Combination of Geodetic Data over the Antarctic Ice Sheet for Monthly Mass Variation Solutions

by

Ryan A. Hardy

B.S., University of Central Florida, 2013

M.S., University of Colorado Boulder, 2016

A thesis submitted to the

Faculty of the Graduate School of the

University of Colorado in partial fulfillment

of the requirements for the degree of

Doctor of Philosophy

Ann and H.J. Smead Department of Aerospace Engineering Sciences

2019

This thesis entitled:
Combination of Geodetic Data over the Antarctic Ice Sheet for Monthly Mass Variation Solutions
written by Ryan A. Hardy
has been approved for the Ann and H.J. Smead Department of Aerospace Engineering Sciences

Prof. R. Steven Nerem

Prof. Delores Knipp

Prof. Tomoko Matsuo

Prof. Michael Willis

Dr. David N. Wiese

Date

The final copy of this thesis has been examined by the signatories, and we find that both the content and the form meet acceptable presentation standards of scholarly work in the above mentioned discipline.

Hardy, Ryan A. (Ph.D., Aerospace Engineering Sciences)

Combination of Geodetic Data over the Antarctic Ice Sheet for Monthly Mass Variation Solutions

Dissertation directed by Prof. R. Steven Nerem

This work presents methods for combining time-variable gravimetry, altimetry, and GNSS bedrock motion data to distinguish sources of mass change in Antarctica with enhanced spatial resolution. GRACE gravimetry provided direct measurements of mass variation of the Antarctic Ice Sheet at monthly timescales between 2002 and 2017, but was limited to a spatial resolution of 300 km. Laser altimetry from ICESat (2003-2009) provided elevation change measurements at fine spatial resolution, better resolving the spatially concentrated sources of Antarctic mass loss, but with sparse temporal sampling. The processes of glacial isostatic adjustment (GIA), ice dynamics, surface mass balance, and firn compaction affect geodetic measurements with distinct magnitudes, timescales, and spatial scales, which means they may be separated through combination of different data sources. This work explores separation of GIA and ice sheet processes by combining data from ICESat and GRACE. This is accompanied by separation of GIA and ice sheet processes using GNSS vertical crustal motion estimates and GRACE. Monthly solutions for combined ice sheet mass variation are developed using monthly GRACE solutions combined with high-resolution ICESat elevation rates. High-resolution monthly solutions for Antarctic mass variation are developed by combining ICESat elevation rates statistical information from models of the processes of interest with monthly GRACE data. This work also examines of the impact of atmospheric modeling errors on estimates of Antarctic mass loss, finding that errors in models used to remove atmospheric signals from GRACE solutions obscure additional acceleration in total Antarctic mass loss. Finally, time-variable GRACE and ICESat data are combined directly to produce 17 time-variable mass solutions at high spatial resolution between 2003 and 2009 with an updated GIA model. The solutions indicate 2003–2009 average mass loss of 116^{+10}_{-51} Gt yr^{-1} and a total GIA mass rate of 110^{+60}_{-24} Gt yr^{-1}. With GRACE Follow-On and ICESat-2 now concurrently in orbit, the methods

developed in this work pave the way toward simultaneous assimilation of their respective gravity and elevation data into a monthly, high-resolution solution for Antarctic mass change.

Dedication

For Harry Moore.

Acknowledgements

I would like to acknowledge the mentorship of R.S. Nerem, Joseph Harrington, David N. Wiese, Kristine Larson, Brent Barbee, and Harry Moore, who provided critical guidance and opportunities throughout the my career. I want to highlight Dr. Nerem's guidance as my advisor throughout this project. I would also like to acknowledge members of my committee, friends, and colleagues who reviewed this work and also provided additional insight. In particular, the useful discussions with Erik R. Ivins, Alex S. Gardner, Mark Seefeldt, and Melissa Nigro were invaluable to this work. Finally, I would like to thank my parents, Annette and Martin Hardy, and my grandmother Cynthia Popplewell for their support and encouragement of my interests and career goals. Thank you.

This work was partly supported by NASA Headquarters under the NASA Earth and Space Science Fellowship Program (grant NNX15AP06H). A portion of this research was carried out at the Jet Propulsion Laboratory, California Institute of Technology, under a contract with the National Aeronautics and Space Administration. This material is based on data services provided by the UNAVCO Facility with support from the National Science Foundation (NSF) and National Aeronautics and Space Administration (NASA) under NSF Cooperative Agreement EAR-0735156.

Contents

Chapter

Tables

Table

Figures

Figure

Chapter 1

Introduction

Observing the changing distribution of mass within Earth's atmosphere, oceans, ice sheets, and ground water is a top priority in modern Earth science (National Academies of Sciences, Engineering, and Medicine, 2018).This task is particularly important and challenging in the largest contiguous mass of land ice on Earth, the Antarctic Ice Sheet (AIS). With its grounded portion spanning over 12 million square kilometers and possessing an average thickness of nearly 2 kilometers, the AIS has the potential to raise sea level by over 58 meters if melted completely (Fretwell et al., 2013). Through gravity-driven ice dynamics, this ice mass continuously flows into the ocean, approximately balanced by incoming precipitation. However, since the early 2000s, various satellite-geodetic estimation techniques have revealed that Antarctica makes net contributions of tens to hundreds of gigatons (1 Gt = 10^{12} kg) per year of ice mass to the oceans, resulting in several tenths of a millimeter per year of sea level rise.

A number of methods exist to characterize the mass balance of the AIS and pinpoint where ice mass is currently being lost. These methods and the processes they detect are illustrated in Figure 1.1. Precise mapping of sources of mass loss in the AIS aids predictions of how these locations will contribute to future sea level rise. Understanding the overall net balance of surface mass balance and ice dynamics will illuminate Antarctica's sensitivity to a changing climate.

Since 2002, the Gravity Recovery and Climate Experiment (GRACE) mission has produced a monthly record of Earth's gravity field, enabling direct estimation of changes in the distribution of water, ice, and solid-Earth mass across its surface. Over Antarctica, GRACE is limited by uncer-

Figure 1.1: Explanation of major ice sheet processes and observable effects

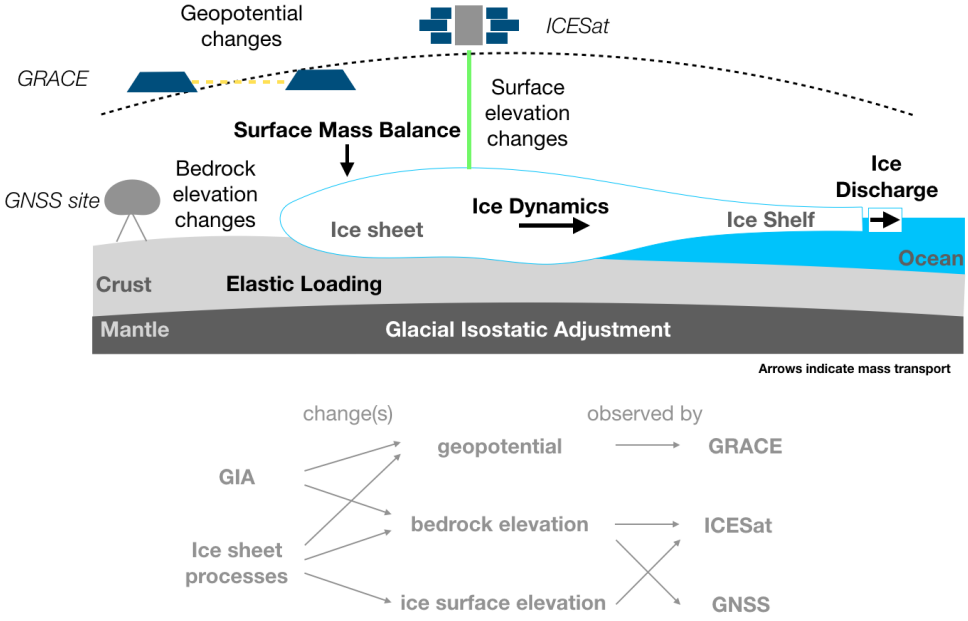

Figure 1.2: Trend signals captured by GRACE (2002–2017), ICESat (2003–2009), and GNSS (2002–2017) vertical position estimates, reflecting geodetic change due to mass variation.

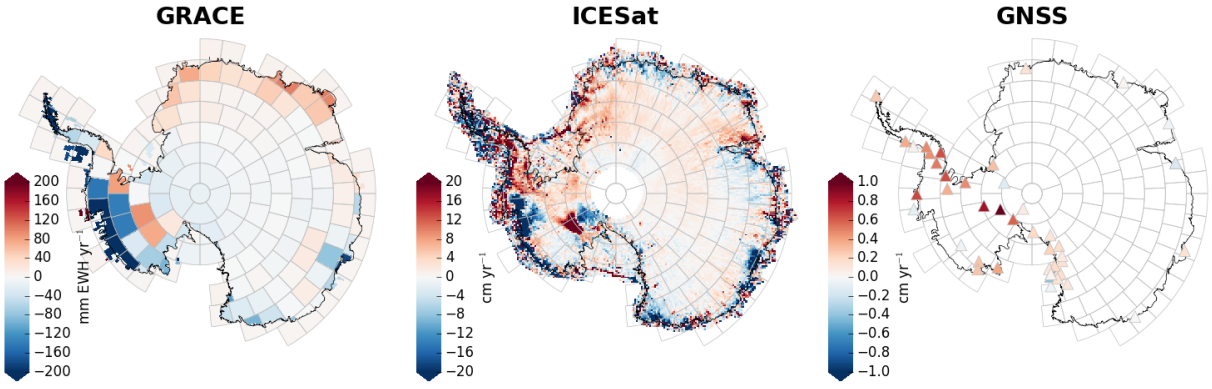

tainty in glacial isostatic adjustment (GIA), the viscoelastic rebound of the solid Earth reflecting loading from ice present during the last glacial maximum, 20,000 years ago. Uncertainty in GIA models results in a wide range of estimates of Antarctic mass loss from anywhere between 50 and 150 Gt yr^{-1} (Martín-Español et al., 2016a).

Changes in the mass of the Antarctic Ice Sheet manifest themselves most directly with elevation change. These may be measured with satellite altimetry. Altimetry missions, such as the Ice, Cloud, and land Elevation Satellite (ICESat), CryoSat-2, and Envisat have recorded surface elevation change measurements at the centimeter level. However, these elevation change estimates are difficult to convert to mass change estimates due to uncertainty in local surface density. Firn compaction, the slow densification of snow as it becomes ice, is a limiting source of uncertainty in the relationship between measured surface elevation change and mass change. Uncertainty in firn compaction models widens the range of possible interpretations such that some authors report mass gains that exceed losses across the continent (Zwally et al., 2015).

Variations in the mass of the AIS are also reflected in elastic deformations of bedrock directly detectable in position time series collected by permanent global navigation satellite system (GNSS) antenna sites mounted in Antarctic bedrock. GNSS vertical motion estimates are extremely sensitive to vertical motion induced by GIA. Elastic loading signals detected in dense GNSS networks have been used to spatially resolve mass variations elsewhere (Argus et al., 2014).

The trend signals captured by these three techniques are illustrated in Figure 1.2. The primary features of these trends are strong, GIA-induced uplift signals in West Antarctica and moderate, long-wavelength GIA signals lining the Antarctic coast; concentrated mass loss signals near the Amundsen, Thwaites, and Totten glaciers; and ice-dynamics-driven mass buildup in the Kamb ice stream.

Geodetic methods used to estimate Antarctic mass change have differing sensitivity to ice sheet processes and background models that limit any single technique. These techniques also differ by orders of magnitude in effective spatial resolution. Combining data from multiple methods could overcome the limitations of any single technique to produce a narrower and less uncertain credible

range of estimates for Antarctic mass loss.

As of December 2018, both the GRACE and ICESat missions are completely inoperative. Their successors GRACE Follow-On and ICESat-2 were both launched in 2018 and are expected to return new science data over the next five years. Additionally, ANET GNSS sites are expected to continue operation in this time period. The concurrent operation of these missions presents an opportunity to develop a system for integrating these data together into a single operational model. As Antarctica's role in future sea level rise remains uncertain (Church et al., 2013), continuous monitoring the mass of this ice sheet through geodetic means will become indispensable.

The objective of this project is to implement combinations of geodetic observations of Antarctica to resolve variations in mass on monthly timescales. The solution should disaggregate GIA, surface mass balance, and ice dynamics. Such a combination also should improve spatial resolution relative to GRACE. Potential spatial resolution improvement could be on the order of 20–100 km. Such a solution should also provide useful predictions of mass variation during periods in which GRACE and ICESat do not observe the Antarctic Ice Sheet concurrently. The combination is informed by the statistics of relevant models, but do not explicitly depend on the internal dynamics of these models or involve direct evaluation of these models.

The scope of this project is limited by one major self-imposed ground rule: there is to be no direct evaluation of dynamics. Dynamical models of the processes that govern observable geodetic changes in Antarctica may not be run on their own. Only model outputs may be used in the development of methods for data combination. Models of GIA, meteorology, ice dynamics, and firn compaction require considerable computational resources and time to develop and properly run. Avoiding the limitations of explicit model dynamics grants flexibility in evaluating filtering approaches. The filter should also not depend on meteorologically driven model outputs for firn compaction, surface mass balance, and ice dynamics as their latency may become a limiting factor in the practical implementation of the data combination.

Where models are used, their spatial statistics should constrain solutions. Published GIA models and covariances should inform the spatial characteristics of the GIA solution. Surface mass

balance and firn compaction predictions from RACMO 2.3 (Wessem et al., 2014; Lenaerts et al., 2013; Ligtenberg et al., 2011) should likewise inform the firn and surface mass balance components of the ice sheet mass variation solution. The ice dynamics should be informed by horizontal interferometric synthetic aperture radar (InSAR) velocities (Rignot et al., 2011) and trend constraints developed by Zammit-Mangion et al. (2013). The project should also leverage previous work in examining atmospheric errors over the Antarctic ice sheet, using reanalyses examined by Hardy et al. (2017) to correct these errors.

The final product should match or exceed the capabilities of filtering schemes developed by Zammit-Mangion et al. (2013, 2015); Schoen et al. (2015); Martín-Español et al. (2016b), particularly in terms of spatial and temporal resolution.

The project should narrow the wide range of solutions for Antarctic mass loss recovered through various methods. These refinements will constrain Antarctica's contribution to current sea level rise. Improved spatial resolution of Antarctic mass loss may also inform projections of future contributions to sea level change as new data are collected. Apparent contradictions between measurements may uncover interesting scientific problems, such as basal melting or post-seismic effects.

The investigation explores a number of semi-independent approaches to the problem of combining Antarctic geodetic data for better mass change estimates. First, errors introduced by uncorrected atmospheric signals to satellite gravimetry are characterized and corrected using a combination of *in situ* pressure measurements and robust atmospheric reanalyses. Techniques to retrieve atmospheric errors from quiescent parts of the Antarctic Ice Sheet are demonstrated, paving the way for satellite gravimetry to become a tool of meteorology. Next, techniques to separate GIA and ice sheet mass variation signals in GRACE, GNSS, and ICESat are explored independently. Monthly and cycle-by-cycle solutions for elevation change in Antarctica are generated and compared with GRACE via linear regression to estimate the distribution of effective surface snow density. Spatial statistics of ice dynamics and surface mass balance (SMB) are used to disaggregate these processes in GRACE data.

High-resolution monthly solutions for Antarctic mass variation are pursued by feeding GRACE data to Kalman filters informed by priors and spatial statistics obtained from ICESat elevation rate fields and surface mass balance models. Basin-level ice mass discharge measurements are also used to constrain these measurements. These filters effectively enhance GRACE solutions. The filter outputs are validated by predicting their elastic loading signals in three-dimensional GNSS time series and verifying that these results either improve or do not unacceptably degrade the residuals of these time series.

History of data combination in Antarctica

Farrell (1972) first examined the relationship between elastic loading and mass change on Earth's surface, formulating Green's functions for elastic effects on Earth's crustal deformation and geopotential, which may be measured through various geodetic methods. These relationships were essential for relating elastic loading detected by altimetry and GNSS time series to local changes in mass. The Green's functions of Farrell (1972) were further essential for relating geopotential changes measured by GRACE to mass changes near Earth's surface. Wahr et al. (1998) ultimately compiled the essential method for relating spherical-harmonic Stokes coefficients to spatial and temporal in Earth's surface mass. Swenson and Wahr (2002), in turn, codified the kernel-averaging techniques necessary for estimating total mass change within a region using GRACE.

Wahr et al. (1995) examined the relationship between vertical motion from GIA and the corresponding change in local gravity. They found an approximate linear relationship between vertical motion and gravity change that enabled solution for GIA through simultaneous linear combination. This linear relationship was refined by Purcell et al. (2011).

Wahr et al. (2000) used simulated data to demonstrate the plausibility of combining of data from the then soon-to-be-launched ICESat and GRACE missions. They concluded that five years of coincident ICESat and GRACE data were sufficient for slight improvement in solutions for AIS mass loss and refinement of GIA. They found that extending the period of data collection between both missions should continue to reduce these uncertainties.

After five years of data had been collected from both the GRACE and ICESat missions, Riva

et al. (2009) attempted to separate GIA and surface processes in the ice sheet through direct linear combination of the trends of total equivalent water height from GRACE and elevation change from ICESat. The combination resulted in an empirical GIA model. This technique was refined by Gunter et al. (2014), who used more robust surface densities. A number of empirical GIA models have followed these approaches, many of which are shown in Martín-Español et al. (2016a), who find that empirical and semi-empirical models tend to find more conservative estimates for GIA corrections than forward models.

Serious efforts at solving the problem of source separation of the constituent processes of measurable geodetic change in Antarctica continued with Zammit-Mangion et al. (2013). They devised a hierarchical Bayesian framework for examining altimetry and gravimetry simultaneously, while leveraging geostatistical information from GIA, firn-compaction, and surface mass balance models to find solutions for total mass balance in West Antarctica. They characterize the spatial and temporal folding scales of the input models and associated variances. A similar approach was taken by Schoen et al. (2015), who also included GNSS vertical motion data. Zammit-Mangion et al. (2015) later continued this hierarchical approach, but expanded the scope of their combinations to cover the entire continent. Martín-Español et al. (2016b) continue this thread, and obtain an empirical GIA solution. Sasgen et al. (2017), as part of the REGINA project, perform a similar disaggregation of GIA and ice sheet mass processes using GRACE, ICESat, Envisat, and GNSS data, but use a GIA modeling approach that allows for lateral mantle structure variation. These papers represent the state of the art in combination of Antarctic geodetic data.

Chapter 2

Background

2.1 Sources of Mass Change in Antarctica

Mass and elevation change in Antarctica may be modeled as a linear combination of four fundamental processes: glacial isostatic adjustment, ice dynamics, surface mass balance, and firn compaction. Each process has characteristic temporal scale, spatial scale, and effective density relating local elevation change to local mass change. Atmospheric effects, such as pressure loading and gravity signals, must also be considered when trying to identify these processes in geodetic data. These processes are summarized in Figure 2.1.

Glacial isostatic adjustment (GIA) is the viscoelastically moderated return of mantle mass displaced by loading from ice sheets present during the last glacial maximum. GIA is detectable as a gravity signal in GRACE and as an elevation change signal in GPS and satellite altimetry. GIA is a long-period signal, which may be treated as a constant trend over decadal timescales. Its geodetic signatures are traditionally forward-modeled using an ice load history and a model of Earth's viscosity profile.

The relationship between elevation change and geopotential change due to GIA is not straightforward, but approximations exist in the vertical direction. Multiple authors, including Wahr et al. (1995) and Purcell et al. (2011) have derived asymptotic linear relationships between gravity change and elevation change, which allow conversion between these quantities independent of load history and solid-Earth structure. This normally results in modeling GIA as a Bouguer plate with $\frac{2}{3}$ the overall density of Earth, or 3700 kg m^{-3}. Other authors, such as (Riva et al., 2009), have refined

Figure 2.1: Classficiation of Antarctic mass variation processes and error sources

Source	Process	Description	Example Model	Typical length scale*	Temporal behavior
Atmosphere	**Atmosphere**	Surface pressure variations	AOD1B; ERA Interim	2000 km†	Sub-monthly to annual timescales; long-period drifts in model errors
Ice sheet	**Firn compaction**	Surface snow densifying into ice	Ligtenberg et al. (2011)	80 km coastal 200 km interior	Interannual
	Surface mass balance (SMB)	Net precipitation, evaporation, and runoff	RACMO 2.3		
	Ice dynamics	Horizontal transport of ice	INSAR horizontal velocities (Rignot et al, 2011)	50 km	Varying trend
Solid Earth	**Glacial isostatic adjustment (GIA)**	Viscoelastic rebound of solid Earth following last glacial maximum	A et al. (2013); IJ05	3000 km	Constant trend

***Schön et al. (2015)**
† This work

this approximation to include self-attraction and loading effects.

Horizontal motion does not follow these asymptotic relationships and requires full modeling of the load history and viscoelastic response of Earth. While it is possible to use a full model to predict the GIA signal in GNSS observations, these signals are difficult to disentangle from additional horizontal motion signals from plate tectonics.

Ice sheet surface processes may be divided into three components: surface mass balance, firn compaction, and ice dynamics. The relationship between the three components may be illustrated in the differential continuity equation for an ice sheet.

$$\frac{\partial \rho}{\partial t} + \rho \nabla \cdot \mathbf{u} = \sigma \tag{2.1}$$

The first term, describing rate of change in local density ρ, captures firn compaction. The divergence term $\rho \nabla \cdot \mathbf{u}$, where $\mathbf{u}$ is the ice stream velocity vector, describes ice dynamics. When the continuity equation is integrated vertically, it implies that gradients in horizontal ice velocities must be balanced by thickening or thinning of the ice sheet in the vertical direction. Ice dynamics may therefore be measured with elevation rates or with horizontal ice velocities. From the divergence theorem, the total contribution of ice dynamics to the ice sheet mass balance may be obtained by integrating the ice velocity divergence over the volume of the ice sheet, or integrating ice velocities through flux gates at the ice sheet boundaries (the grounding line). Finally, the external inputs from precipitation, runoff, and evaporation above the ice sheet are included in the differential volumetric mass generation term σ, the surface mass balance (SMB).

Surface mass balance generates a net ∼2,500 Gt per year of total accumulation on the continent, an amount approximately balanced by ice dynamics. The state of the art in Antarctic surface mass balance modeling is represented by the Regional Antarctic Climate Model (RACMO) 2.3 (Wessem et al., 2014; Lenaerts et al., 2013). The accumulated mass loading of SMB signature may be detected by GRACE directly, through changes in geopotential; GNSS, through changes in elastic loading of bedrock; and satellite altimetry via the combined effects of elastic loading and volume

change in the ice sheet. The effective density of surface snow is time-dependent, but its steady state may be empirically modeled as a function of annually-averaged temperature, precipitation, and wind speeds (Kaspers et al., 2004).

Firn densification, or firn compaction, is the slow consolidation of accumulated surface snow under its own weight and the weight of additional accumulation. Firn compaction is directly observable with altimetry. According to the model produced by Ligtenberg et al. (2011), firn densification has deflated the volume of the ice sheet by $\sim$90 km^3 yr^{-1} between 2003 and 2016, causing altimetry to systematically overestimate the mass loss of the continent if uncorrected. Fortunately, because it has no associated loading or mass change signal, it is not detectable in geopotential or bedrock motion, raising the possibility that it is separable from other ice sheet processes if other measurements are involved. In some approaches to the problem of data combination over Antarctica, firn compaction is treated as a background signal that must be subtracted from altimetry before combination with other data. In others, firn compaction is treated as a separate process that may be disaggregated through the combination of GRACE and altimetry data. Both approaches depend on information from available models. Additionally, some authors have proposed using differences between radar and laser altimetry penetration depths to reveal changes in firn density.

Ice dynamics, the gravity-driven, viscoelastically moderated flow of ice sheet material into the ocean, is another long-period process. Temporally, this flow is modulated by changes in air and ocean temperature, surface mass balance, and bedrock topography. These processes may drive a physical model of ice dynamics. However, the use of numerical models is explicitly beyond the defined scope of this work, which is limited to combining geodetic data to map mass change directly. Instead, ice dynamics may be regarded as a relatively constant trend in mass and elevation change with allowance for variation according to observational constraints. Constraints on surface elevation change due to ice dynamics may be drawn from horizontal ice surface velocity measurements derived from INSAR (Rignot et al., 2011), following Zammit-Mangion et al. (2013). Ice dynamics is directly observable in the same manner as surface mass balance, as it directly affects geopotential, elastic crustal deformation, and ice sheet surface elevation.

Atmospheric signals also contribute to geodetic measurements in Antarctica. Atmospheric pressure loading causes elastic crustal deformations on the order of several millimeters over most of Earth's surface (Petrov, 2004). Pressure loading deformations affect GNSS and altimetry measurements and must be corrected if sub-centimeter elevation accuracy is required.

Gravity from atmospheric mass variations in space and time can be detected by GRACE. The sub-monthly component of these variations can introduce temporal aliasing errors to GRACE estimates of mass change within a region, while lower-frequency atmospheric signals can introduce considerable bias to these estimates. These atmospheric signals are subtracted during processing of GRACE data using a dealiasing model known as AOD1B (Flechtner, 2007). The atmospheric component of this model currently uses the ECMWF operational analysis model. The operational nature of this model introduces drifts, discontinuities and other biases to GRACE solutions, which may be quantified by comparing the dealiasing model with alternative atmospheric models, such as reanalyses, or in situ surface pressure data. Over Antarctica and Greenland, Hardy et al. (2017) use alternative models to find that long-term drifts in the dealiasing model can introduce substantial errors in mass loss acceleration estimates on the order of 4 Gt yr^{-2}. Hardy et al. (2017) further demonstrated that these errors are large enough to be detectable over quiet, high-elevation parts of the continent.

Atmospheric signals are treated as a background process that must be removed to accurately recover ice-sheet and solid-Earth mass variations. It is not presently practical to recover these processes separately, though the unique sensitivity of Antarctic GRACE results to atmospheric models may one day make Antarctica a testbed for gravity as a meteorological observable.

2.2 Geodetic Methods for Observing Antarctic Mass Change

This work considers three primary data sources: GRACE geopotential fields, GNSS position data, and satellite altimetry. GRACE senses the sum of geopotential contributions of GIA and surface mass change, including ice dynamics and surface mass balance. GPS receivers that are mounted in bedrock can measure elevation changes due to GIA and elastic loading from surface

mass change. Finally, satellite altimetry can sense the sum of elevation changes due to all four processes. The spatial and temporal distribution of data used for this project is summarized in Figure 2.2.

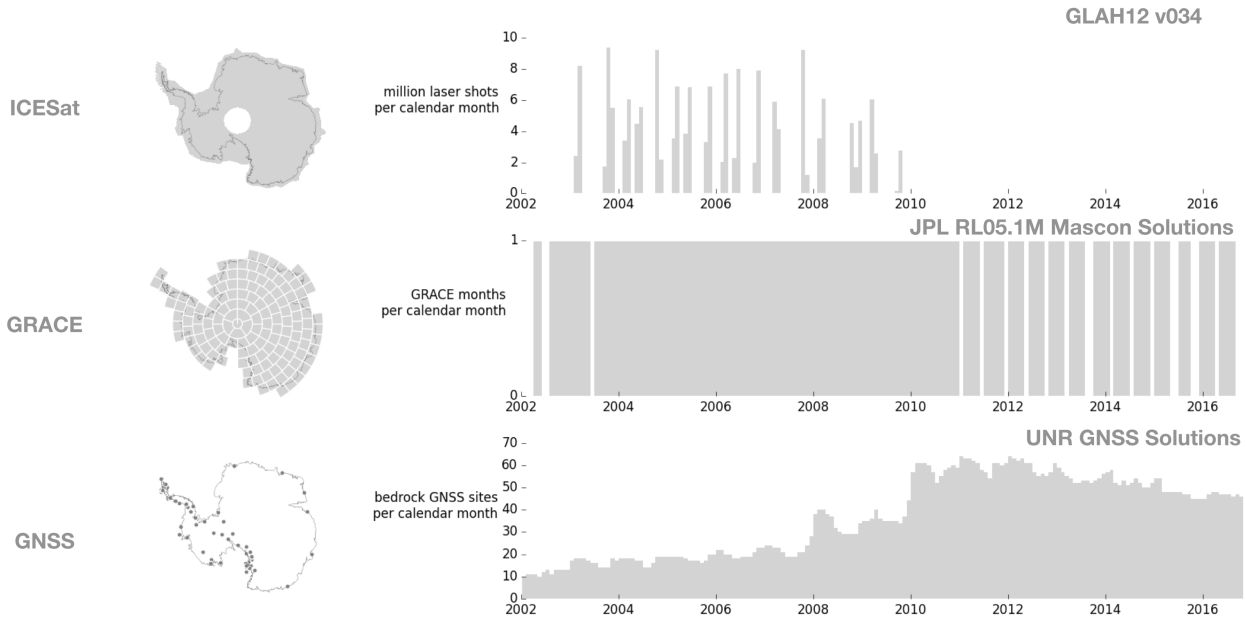

Figure 2.2: Spatial (left) and temporal (right) distribution of ICESat, GRACE, and bedrock-mounted GNSS data.

2.2.1 Gravity

The GRACE mission, launched in March 2002 and terminated in October 2017, consisted of twin satellites orbiting approximately 400 km above Earth's surface separated along track by approximately 200 km. The satellites were linked by a K-band microwave signal, variations in the phase of which can be used to determine changes in intersatellite range on the order of 10 μm. These variations reflect changes in Earth's gravity field and may be inverted to produce monthly global gravity solutions. These geopotential fields, in turn, may be inverted to reveal variations in mass near Earth's surface. GRACE was sensitive to variations in hydrology, land ice, displacements of the solid Earth, ocean bottom pressure, tides, and atmospheric pressure. As these signals are all linearly combined within a GRACE solution, isolating any single mass transport process requires

models of the gravity signals of all other major processes. The uncertainty of these background models can become a limiting factor in measuring any of these processes. Over Antarctica, the primary source of uncertainty is GIA, which is about ± 70 Gt yr^{-1} (Caron et al., 2018).

Multiple GRACE-based solutions for time variations in Earth's gravity exist, using differing filters and basis functions. In the initial exploration of this problem, both mascon and spherical-harmonic solutions were used. The spherical-harmonic solutions used here are the RL05 Stokes coefficients produced at maximum degree and order 60 by the University of Texas at Austin Center for Space Research.

The JPL RL05.1M mascon (mass concentration) solutions (Watkins et al., 2015; Wiese, 2015) were also used. These use a more natural set of basis functions, representing Earth's gravity field as a set of 4,551 spherical caps. The mass distribution within these caps is processed using *a priori* constraints and spread over the bounding quadrilateral of each cap. The mascons are further partitioned to disaggregate land and ocean signals by their distinct geostatistical properties through the coastline resolution improvement (CRI) filter.

A special subset of land-components of the 148 CRI-filtered mascons on the grounded portion of the Antarctic ice sheet and surrounding islands was used for input data in Chapters 4, 5, and 6. This mascon subset is illustrated in Figure 2.3.

The GRACE Follow-On mission, launched in May 2018, will continue to provide Antarctic gravity observations.

2.2.2 Laser Altimetry

Laser altimetry is the measurement of surface elevation by timing the emission of radiation from a platform and the return of this radiation after it is reflected from this surface. Knowing the round-trip transit time of this radiation, its speed of propagation, factors that change its velocity along its path, and the precise position and orientation of the platform enables measurement of the elevation of a point on Earth's surface at a particular time. Laser altimetry directly measures the elevation of the uppermost layer of the ice surface at a given elevation, enabling measurement of

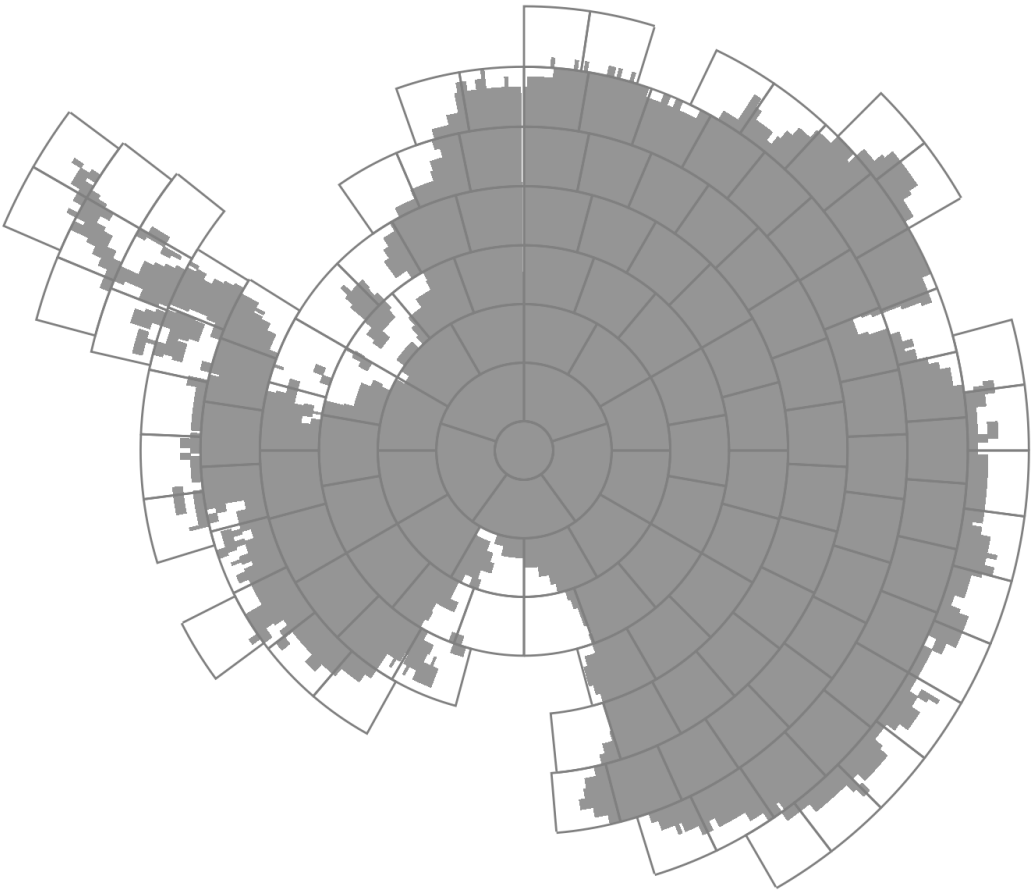

Figure 2.3: Quarter-degree Antarctic land mask for use with JPL RL05.1M mascon products. Mascon bounds are overlaid to illustrate how the "land mascon" data subset used in this work is developed.

volume change of the ice sheet. Altimetry is also sensitive to bedrock elevation change due to GIA and elastic loading. While many altimetry products exist for Antarctica, the focus of this project has been limited to processing ICESat laser altimetry data. Other radar-based measurements exist, but harbor their own set of challenges in processing and interpretation.

ICESat was launched in 2003 and ceased operation in 2009. In this time, it recovered over 1 billion laser shots, approximately 130 million of which fell over the Antarctic ice sheet. ICESat was placed in a 91-day repeat orbit with an inclination of 94.0°, enabling observations as far south as 86° S. ICESat's groundtrack permitted observation of 95% of the grounded portion of the AIS. Its primary science instrument was the Geoscience Laser Altimeter System (GLAS), which emitted laser pulses at 1064 and 532 nm. The laser was normally operational for 25–45 days in ICESat's repeat cycle, and was typically used every other cycle, for an effective biannual temporal resolution. At Earth's surface, each GLAS beam footprint spanned approximately 70 meters and was separated by 170 meters along track.

The altimetry data used here are GLAS/ICESat L1 and L2 Global Altimetry Data, Version 34 GLAH12 (ice sheets) subset, which consist of geolocated altitude measurements. These data are available at the National Snow and Ice Data Center (NSIDC) archive[1] . The millions of data points available in this dataset require additional processing on the user end to establish temporal variation, which is discussed later in this document.

ICESat was succeeded by ICESat-2, which launched in 2018. While ICESat-2 follows a 91-day repeat ground track, like its predecessor, it uses six lasers instead of ICESat's single beam to locally increase spatial resolution and better establish topographic slopes. It also has a more polar inclination than its predecessor, covering latitudes as far north and south as 88°. ICESat-2 is expected to have highly accessible time-variable elevation products for the Antarctic ice sheet [2] .The ATL06 product will consist of geolocated surface heights with along-track and cross-track slopes. The ATL11 product will be a time series of heights at selected points on the ice sheets. The ATL14

[1] http://nsidc.org/data/docs/daac/glas_icesat_l1_l2_global_altimetry.gd.html
[2] https://icesat-2.gsfc.nasa.gov/science/data-products

product will provide monthly maps of land ice elevation for each year in the campaign. Monthly sub-cycle products are also anticipated. The design of these products permits straightforward temporal coregistration of altimetry products with GRACE-FO for future data combination.

2.2.3 GNSS-Measured Crustal Motion

GNSS refers to any set of satellites in high- or medium-Earth orbit used to produce geospatial position solutions, including the US Global Positioning System (GPS), the European Union's Galileo, and Russia's GLONASS. The term GPS is sometimes used interchangeably with GNSS to metonymically to refer to all GNSS-based measurements. In all GNSS setups, satellites broadcast signals according to precise atomic clocks to passive receivers. These receivers compare the timing of these messages with their own internal clocks, to obtain pseudorange measurements. Four or more pseudorange measurements are necessary for establishing a receiver's clock bias and three-dimensional position.

Pseudorange measurements are limited by how well receiver electronics can align the digital signals in GNSS satellite messages with internal reference messages; this translates to meter-to-decimeter-level solution precision. However, more sophisticated GNSS users are able to enhance the precision of their position solutions using carrier-phase tracking. As typical GPS signals have a bit length of hundreds of meters, but carrier-signal wavelengths on the order of 20 cm, tracking the phase of the carrier wave affords much more precision in range measurement. This increased precision enables sensitivity to millimeter-level deformation induced by elastic loading and GIA.

The GNSS data used for this project come from the University of Nevada, Reno Plug and Play daily position solutions (Blewitt et al., 2018). Position time series were downloaded from over 150 stations installed in Antarctica between 2002 and 2017. Only stations determined to be mounted in bedrock were eligible for inclusion in this work because of the need to accurately measure bedrock deformation due to GIA and elastic loading. Most of the 150 stations are not mounted in bedrock or have too short of a record to be useful for measuring bedrock velocities.

Whether stations were mounted in bedrock was determined by comparing their horizontal

velocities with a plate motion model. Observation sites with records shorter than 36 months were also removed from the analysis. There are 68 remaining bedrock-mounted stations in total. Of the remaining stations, 10 stations in the Antarctic Peninsula (within 330 km of 66° S, 65 ° W) were excluded to GIA misfitting due to the unique structure of the mantle in that part of Antarctica. The stations BERP and BACK were also excluded due to known problems with rime formation and other major error sources[3] . The daily position time series were then binned to the intervals defining GRACE months, leaving a total of 56 stations used for verification.

Although the GNSS position solutions are available in three dimensions, this study is often limited to using only the vertical component of these data. While horizontal motion induced by elastic loading is easily predicted using techniques established by Farrell (1972), other effects that induce horizontal motion in Antarctica are more difficult to model. This is due to high uncertainty in the horizontal observation operators for GIA. In contrast with the simple analytic rules relating GIA to both its geopotential and vertical motion effects are found by Wahr et al. (1995), Wahr et al. (2000), and Purcell et al. (2011), GIA observation operators for horizontal motion are highly model-dependent. Furthermore, plate tectonics can be difficult to separate from GIA-induced motion. Horizontal motion does represent an additional source of elastic loading signals, however. Where possible, *detrended* horizontal position time series are used for validation.

[3] Erik Ivins, personal correspondence

Chapter 3

Investigation of Atmospheric Errors over Antarctica

The role of systematic atmospheric errors in GRACE estimates of mass variation over the Antarctic ice sheet was examined exhaustively as part of this work. Methods for correcting these errors in GRACE data were developed using reanalyses and alternative data. Monthly averages of the atmospheric component of AOD1B RL05, referred to as GAA, may be added back to GRACE mass flux estimates to restore monthly averages of the total gravity field of Earth. Similar averages of atmospheric surface pressure from alternative models may then be subtracted to correct these atmospheric errors.

Investigating errors in AOD1B with alternative models and comparison with in-situ pressure data reveals significant drifts in GAA on annual and interannual timescales. These errors hide approximately 4 Gt yr^{-2} of additional acceleration in mass loss, roughly 40% of the 11 ± 4 Gt yr^{-2} total acceleration found by Velicogna et al. (2014). These errors are large enough to recover from quiet parts of Antarctica. Characterizing and these errors will be essential to accurate estimation of mass variation in Antarctica.

Further details on this investigation are given by Hardy et al. (2017) and are reproduced in abridged form in the following sections.

3.1 Data and Methods

In situ surface pressure measurements are the primary record of ground truth for Antarctic surface pressure. They are used to assess the accuracy of AOD1B and all alternative models. Data

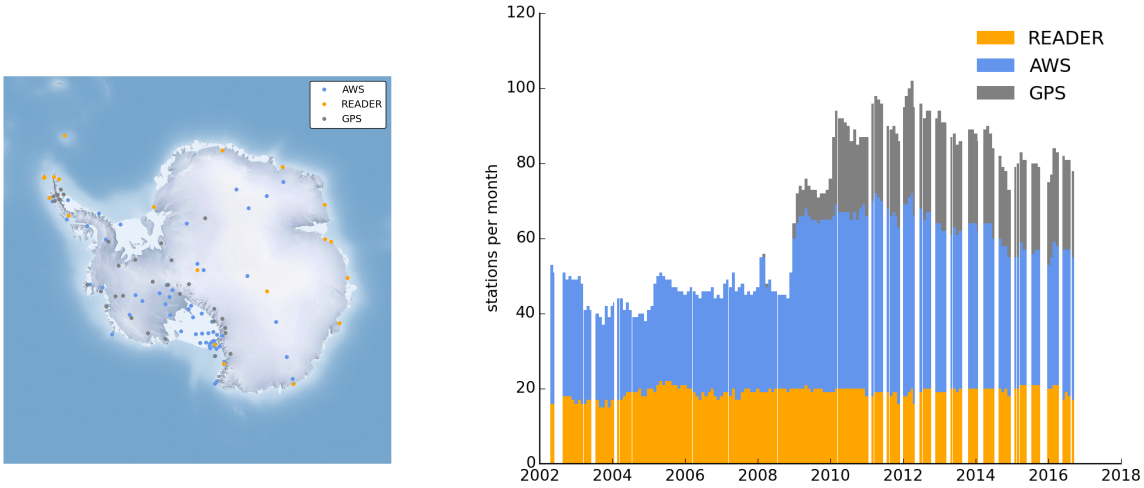

Figure 3.1: Spatial (left) and temporal (right) distribution of available surface pressure observations from AWS, READER, and Antarctic GPS networks available within GRACE months.

collected between 2002 and 2016 from 114 observation sites were obtained from three different data archives were used for this comparison. US Antarctic Program automatic weather stations (AWS) have their data archived at the University of Wisconsin Madison's Antarctic Meteorological Research Center (Lazzara et al., 2012) and comprise over half the data used for this analysis. Observations from 22 sites in READER (REference Antarctica Data for Environmental Research, Turner et al. (2004)), an archive of monthly averages from meteorological instruments maintained by the British Antarctic Survey's scientific committee on Antarctic Research were also used. Ancillary pressure measurements from 31 GNSS sites were used in the comparison as well. These observations were recorded to correct atmospheric propagation delays in GNSS processing, but are nonetheless a valuable record of surface pressure over Antarctica. The value of the GNSS surface pressure data is enhanced by the fact that they are not assimilated into reanalyses or forecast models considered in this analysis. The locations of all stations used in the analysis and the numbers of stations used for each GRACE month are shown in Figure 3.1.

Relative to instrumental data, GAA has an RMS surface pressure error of 14.1 mm water equivalent.

GAA from AOD1B RL05 is compared with five different reanalysis products: NCEP-DOE (Kanamitsu et al., 2002), MERRA, MERRA-2 (Rienecker et al., 2011), ERA-Interim (Dee et al., 2011), and JRA-55 (Kobayashi et al., 2015). Of these models, only ERA-Interim, MERRA-2, and JRA-55 are of the most recent generation of reanalysis models. MERRA has been deprecated as of February 2016. MERRA and NCEP-DOE are only included for completeness as these reanalyses have been commonly used for comparison in the past (e.g, Kim et al. (2016)).

As a new version of AOD1B (AOD1B RL06) is now available, it was also included in the comparison. This new product will be used to dealias future GRACE and GRACE Follow-On solutions (Dobslaw et al., 2017). This new product differs from RL05 in several ways. The atmospheric component is a composite of the ERA-Interim reanalysis prior to 2007 and the ECMWF Operational Analysis thereafter. It is provided at a higher spatial resolution (degree and order 180) than RL05 (degree and order 100). The atmospheric component also includes upper-atmospheric density anomalies, although their effects are shown to only have an effect of a few mm EWH.

The definition of the atmospheric component of AOD1B RL06 has changed such that direct comparison with RL05 is not straightforward. To minimize correlation between the atmospheric and oceanic component due to the inverse barometer effect, GFZ removed the atmospheric pressure signals in RL06 over the oceans almost entirely. Instead, the sum of local atmospheric and oceanic contributions to ocean bottom pressure are included in the oceanic product (`ocn`/GAB), while the atmospheric component replaces oceanic surface pressure signals with the average surface pressure of the entire ocean. This makes direct comparison of the AOD1B RL06 `atm`/GAA products with surface pressure observations and model outputs impossible over oceans, islands, ice shelves, and inland locations within a wavelength ($\sim$220 km) of the coast.

Instead, the `glo`/GAC (atmosphere plus ocean) products of both AOD1B RL05 and RL06 products are compared. As these fields are the most direct reflection of the gravity signals sensed by GRACE, comparing them directly provides a more accurate indication of the errors introduced by the model changes. In situ validation of AOD1B RL06 was performed with comparisons with inland observation sites more than 220 km from the grounding line of each ice sheet. These comparisons

are performed with the GAA product. Because AOD1B RL06 was not used in any official GRACE products at the time this analysis was performed and subsequently published, no *official* GAA or GAC product was available for AOD1B RL06. Custom versions of these products were created by averaging 3-hour AOD1B RL06 fields within the time periods used to define GRACE months for the JPL RL05 solution.

All weather models are resampled onto a common 200x200 stereographic grid centered on the south pole. Model resolution differences are controlled by converting these models to spherical harmonics and evaluating them at a maximum degree and order of 100. AOD1B RL06 was the only exception to this, and was evaluated at degree and order 180. The grid is inscribed by the 60 °S parallel and has a maximum latitude of approximately 48.5 °S. The effective resolution of this grid is 34 km.

Each of the reanalyses uses different physics, resolutions, data assimilation schemes, and initial conditions to propagate their pressure fields over time. These differences between their implementations separate the models from the ground truth in independent ways. It is, therefore, reasonable to assume that a combination of models will better reflect the ground truth better than any single model. The success of ensemble approaches has been demonstrated for decades in meteorological literature (e.g., Weigel et al. (2008)). Model combination driven by the modern reanalyses, ERA-Interim, JRA-55, and MERRA-2 was implemented.

The most basic combination method was an unweighted average of all three models. However, with 114 Antarctic observation locations available over the entire observation span, it is also possible to generate synthetic pressure fields that are semi-independent of the models. These surface pressure fields are interpolated from instrumental surface pressure measurements or their residuals relative to GAA. They have a distinct advantage over simple averaging of instrument data because interpolation addresses the problems inherent in the spatial heterogeneity of the instruments.

These solutions take the form,

$$\hat{x} = PH^T(HPH^T + R)^{-1}\mathbf{y}, \tag{3.1}$$

where P is the covariance of the model grid, H is a linear operator relating the model grid to observations, R is the residual observation covariance (a diagonal matrix with elements estimated as 150 mm^2 from semivariogram), $\hat{x}$ is the estimated correction to the grid and $\mathbf{y}$ is a vector of pressure observations relative to an *a priori* background model. We present two interpolation approaches, optimal interpolation and the ensemble Kalman filter, which are distinguished by how we estimate the model covariance P. Both formulations are similar to least-squares collocation (Moritz, 1978) or the Kalman filter in the spatial domain.

With optimal interpolation, the covariance is estimated from the sample covariance of ERA-Interim surface pressure evaluated over the entire grid and time span and the grid points corresponding to the instrument locations. This scheme better captures fine-scale variability than kriging as the model dynamics are captured by its covariance.

The ensemble Kalman filter estimates the covariance term state at any given month using the mutual sample covariance of selected reanalyses, with the *a priori* state estimate generated from the mean of these models. The ensemble members are ERA-Interim, JRA-55, and MERRA-2. Unlike with the optimal method, the covariance is not stationary and changes from month to month, meaning model dynamics can be better represented for each month. This method follows the observation-matrix-free formulation of Mandel (2009). This implementation of the Kalman filter has no memory of previous grid states and imposes no correlation of states across time. The evolution of the *a priori* state deviation and covariance are implicitly contained in the ensemble covariance and mean. Because the ensemble only contains three members, all resulting solutions are constrained to two effective degrees of freedom per month.

3.2 Results

Over the entire continent, the RMS of the residuals of GAA against the instruments chosen for this analysis is 14.1 mm water equivalent over the entire timeframe. GAA performs poorly over topographically variable regions, like the Transantarctic Mountains near the coasts, where fast-moving polar lows are difficult to model or occur at too fine a scale.

Comparing instrument time series to GAA, clear, temporally correlated biases become apparent. Most importantly, where instruments have been present before 2008, the bias time series in Antarctica show a distinct U-shape across many instrument locations. This suggests that there is a long-wavelength acceleration bias in GAA with respect to the instruments.

Taking an unweighted average of instrument anomalies over each month yields the time series shown in Figure 3.2. Fitting an annual sinusoid, trend, and acceleration yields a high-signal-to-noise acceleration of 0.39 ± 0.05 mm yr^{-2}. This is somewhat smaller than the 0.58 ± 0.07 mm yr^{-2} found by Kim et al. (2016), who restrict their data to inland stations over a shorter time period. The acceleration is less prominent in coastal stations. READER stations, which are almost entirely sited with a few hundred kilometers of the grounding line, do not see this acceleration in aggregate. AWS and GPS observation sites, which are more likely to be inland show similar patterns in model drift, however.

Simple scaling by the grounded area of Antarctica suggests this is consistent with an acceleration of 4.7 ± 0.6 Gt yr^{-2}, which may be subtracted to correct a GRACE mass loss time series. This represents a statistically significant bias ($\sim 8\sigma$) in previous acceleration estimates of Antarctic mass loss.

This averaging approach is the simplest possible as it queries instruments directly with few additional steps. However, as the differences between observation networks illustrate, the heterogeneous spatial distribution of instruments across Antarctica limits the utility of this simple unweighted averaging. The density of observation sites in West Antarctica is far greater than that of East Antarctica, for instance. GPS stations with colocated pressure sensors also tend to be mounted in exposed bedrock, limiting coverage in East Antarctica. Comparison of GAA with reanalyses and spatial interpolation of instrument data yield more realistic estimates of mass bias due to atmospheric errors.

Comparison of the aforementioned models with GAA consistently shows significant spurious accelerations in GAA. These accelerations, along with linear trend, annual sine and cosine, and RMS difference are shown in Table 3.1. Maps of linear trend, annual sine and cosine, and RMS are

given in Figure 3.3. The time series of total mass bias given for each model is shown in Figure 3.4. All models, except MERRA show improved RMS errors with respect to the instruments. Typical RMS values are approximately 12 mm EWH. Unsurprisingly, combinations of reanalyses show additional improvement with respect to surface observations, with typical RMS errors between 10 and 12 mm EWH. The "Optimal" interpolation scheme returns the best performance with respect to observations with an RMS of 10.8 mm EWH. With the exception of NCEP-DOE and MERRA, these results all show a consistent acceleration bias of $\sim$4 Gt yr^{-2}. This acceleration bias is uniformly distributed about the continent.

Comparison of GAA with the AOD1B RL06 version reveals marginal improvement in accuracy relative to instruments over Antarctica. Because of changes in the product definition, the RL06 version of GAA is not comparable with the RL05 GAA or other surface pressure data over oceans. Furthermore, because of spectral leakage, the comparison of RL06 GAA with other pressure data can only be made more than a full wavelength inland, or 220 km. Comparison with instruments is therefore restricted to 35 inland stations, which the RL06 version of GAA matches within 9.0 mm EWH RMS compared with RL05's 9.5 mm EWH. The GAC products of each model are compared to highlight the effects of model versions on total mass change in Antarctica. It is found that RL06's GAC captures the drift of RL05 relative to ERA-Interim between 2002 and 2007. After 2007, the outputs are nearly identical across versions with small differences attributable to differences in resolution and discontinuities due to model-change corrections. The overall acceleration error between 2002 and 2016 is diminished relative to other models, only 1.7 $\pm$ 0.3 Gt yr^{-2}. This means that AOD1B RL06 may still introduce significant acceleration errors on the order of 1–3 Gt yr^{-2} relative to modern reanalyses, owing to the continued use of the ECMWF Operational Analysis model.

Figure 3.2: Time series of mean difference between instrumental surface pressure data and surface pressure predictions from GAA. The solid black line represents the unweighted monthly mean of all AWS, READER, and GPS instruments available at a particular time while the gray fill shows the 1σ variability of instrument residuals about this mean. The time series of average pressure error of GAA relative to each pressure network are shown alongside the average of all stations, highlighting the importance of instrument spatial distribution in detecting this signal. The smooth black curve is the polynomial component of a polynomial-plus-annual-sinusoid fit to these data.

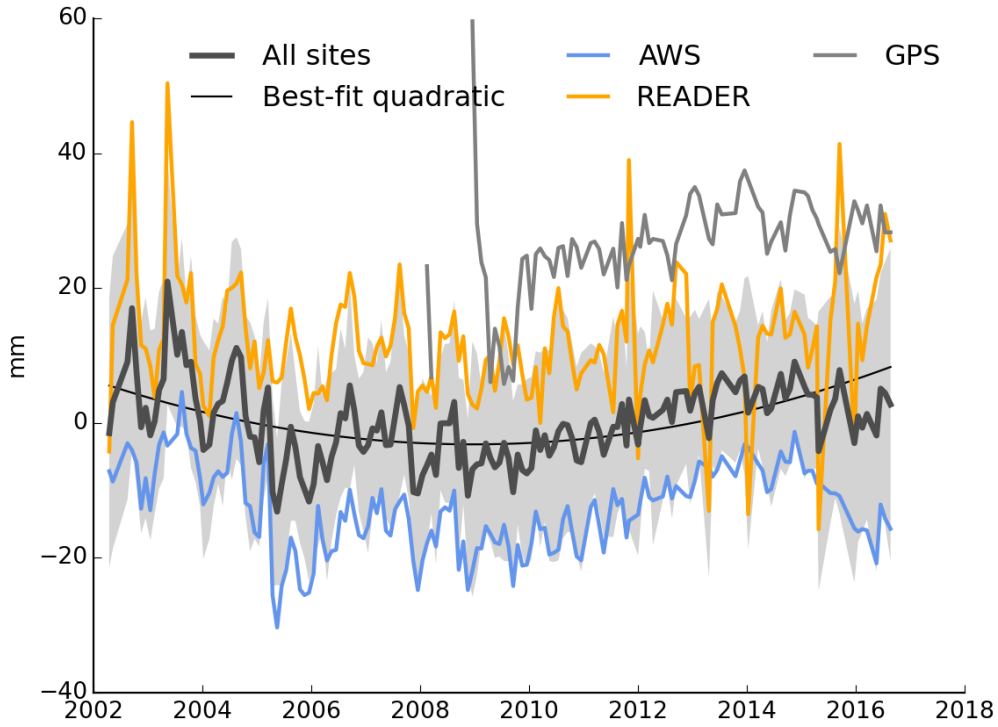

Figure 3.3: Spatial distribution of trend, annual, and acceleration signals for selected models with respect to GAA (model minus GAA). The GAC component (atmosphere plus ocean) of AOD1B RL06 is compared with the GAC component of RL05 instead of comparing GAA between versions because of incompatible product definitions.

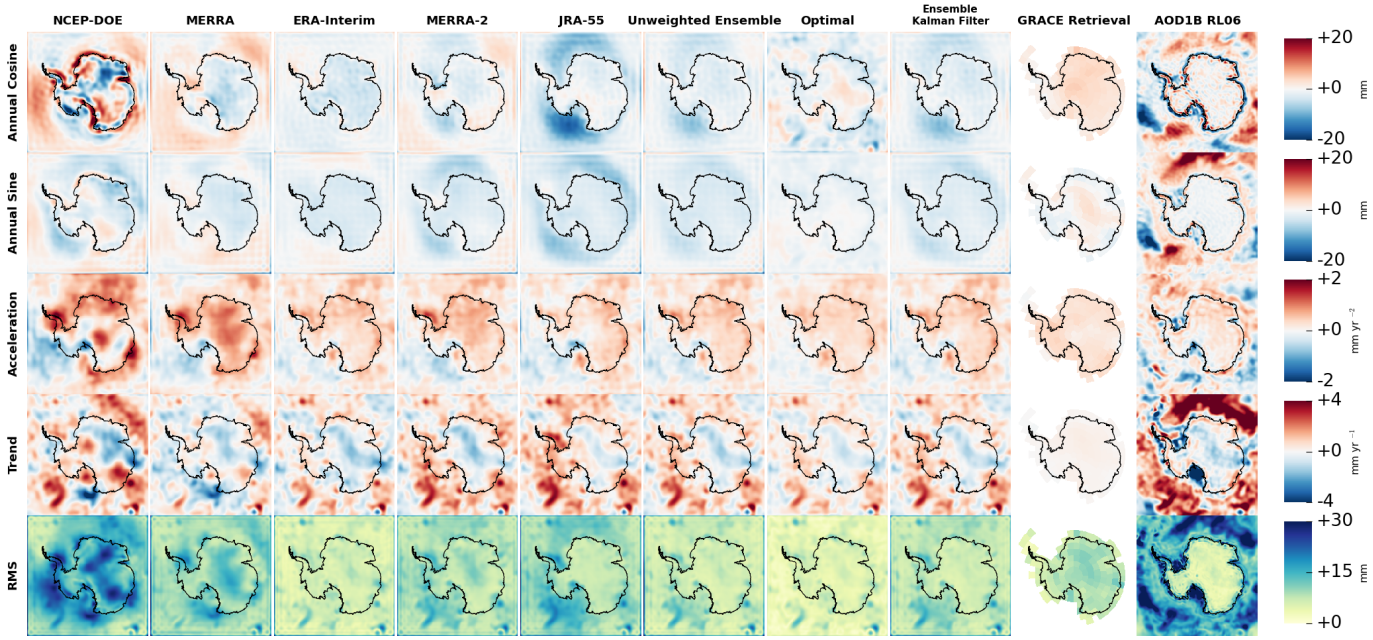

Figure 3.4: Time series of total mass bias over the Antarctic ice sheet for selected models with respect to GAA (model minus GAA, blue). AOD1B RL06 is distinguished by a comparison of GAC (atmosphere plus ocean) with RL05's GAC due to incompatibility of GAA definitions between versions, but accurately reflects the difference in Antarctic mass between versions. All models show a characteristic U-shape consistent with errors in GAA introducing a spurious acceleration signal in the time series of Antarctic mass loss. This is highlighted by the polynomial component of a simultaneous annual sinusoid plus polynomial fit (black). These curves may be subtracted from a GRACE mass time series to yield a corrected time series.

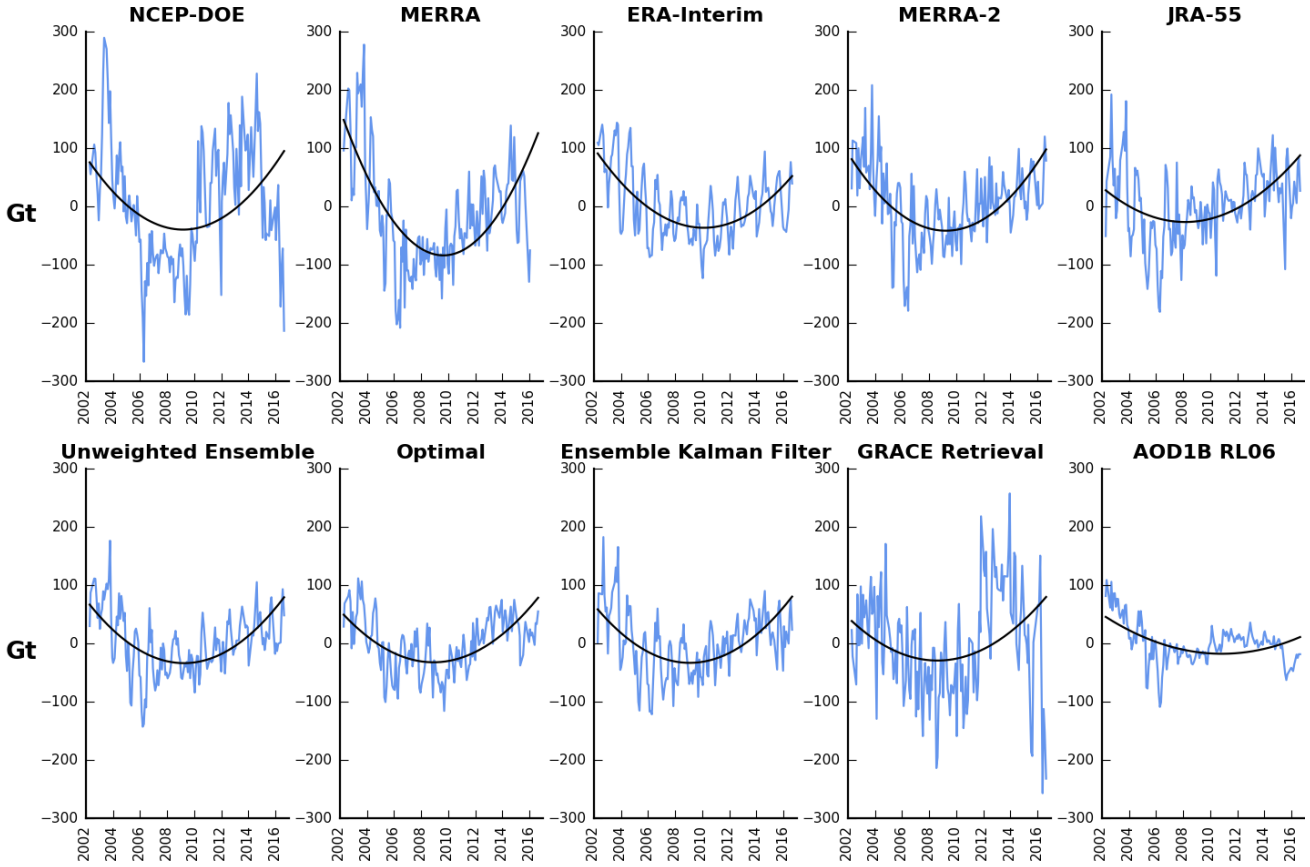

The presence of significant surface pressure errors in GRACE data highlights the possibility of assimilating GRACE data into numerical weather models. This cannot be accomplished without first demonstrating that known pressure errors are present in GRACE data over Antarctica.

The models and surface pressure field generation techniques explored in the last sections all generate consistent monthly bias time series, any of which may be used as a "truth" dataset. This motivates the search for the signatures of these models in the JPL RL05.1M mascon solution. Mascons are preferred because their processing results in reduced noise relative to spherical-harmonic solutions from the same data, which fall victim to striping and other noise sources.

The focus of this search is on part of the High Antarctic Plateau (HAP), which is defined here as a contiguous region of East Antarctica with an elevation greater than 2500 m. Annual surface mass balance accumulations are typically less than 50 mm per year above this elevation. Additionally, surface pressure errors above this elevation exceed the variability of surface mass balance by up to 2 orders of magnitude, meaning that non-trend signals in this region should be attributable to surface pressure errors. Within this region, calibrated errors in equivalent water height variation are 9–16 mm, comparable with the 14.1 mm EWH RMS difference between GAA and instruments. This is partly because GRACE's polar orbit crosses this region 15 times daily, yielding a higher number of gravity observations within an observation span than can be gained at lower latitudes.

The predicted integrated pressure error signal from optimal interpolation over the High Antarctic Plateau is compared with the corresponding mascon time series in Figure 3.5. The mascon time series, while considerably noisier than the predicted surface pressure error time series, has very similar low-frequency characteristics as the pressure error time series. Most notably, a best-fit quadratic function fit to the mascon time series (weighted by observational errors) shows good agreement with the predicted errors; their computed accelerations agree within errors.

The presence of atmospheric mass error is verified by comparing the recovered HAP mass time series with the optimal-interpolation surface pressure error model, which fits ground data best. The goodness of fit of this model is measured relative to the GRACE data by computing χ^2,

defined by

$$\chi^2 = \sum_{i=1}^{n} \frac{(\delta m_{\mathrm{HAP,i}} - \delta m_{\mathrm{model,i}})^2}{\sigma^2_{\delta m_{\mathrm{HAP,i}}}},$$

where n is the number of GRACE months, $\delta m_{\mathrm{HAP,i}}$ is the total mass variation of the HAP detected by GRACE for an individual month, $\sigma^2_{\delta m_{\mathrm{HAP,i}}}$ is the error in total mass obtained from the calibrated errors in the GRACE solutions, and $\delta m_{\mathrm{model,i}}$ is the predicted mass variation from a candidate model.

The χ^2 value for a model of zero pressure error is 269.7. When the optimal interpolation model is used as a candidate model to explain the observed pressure variations, χ^2 is 216.7. Furthermore, an error-weighted fit of observed surface mass and predicted pressure error from the optimal interpolation model reveals a regression coefficient of 0.95 $\pm$ 0.17 and a correlation coefficient of 0.45, strongly hinting at the correspondence of these datasets. Similar results may be yielded with comparison with the ensemble Kalman filter and the unweighted ensemble. It should be noted that individual reanalyses do not improve the χ^2 or show a regression coefficient statistically identical to 1. Nonetheless, the GRACE data agree with the more accurate instrument-driven pressure fields.

With a strong hint of the presence of recoverable pressure error signals in the data, attempts to retrieve these signals are conducted more systematically. GRACE is sensitive to changes in total mass. To simplify this process, the long-period influences of ice dynamics and GIA were removed by detrending the mascon time series.

A Kalman filter was applied to the detrended GRACE data to simultaneously disaggregate surface mass balance and surface pressure signals. The a priori covariance was estimated from the month-to-month difference in surface pressure bias estimated from ERA-Interim and the monthly average sum of precipitation and evaporative losses modeled by ERA-Interim. The filter estimates the mascon-averaged values of surface mass balance x_{SMB} and surface pressure bias $x_{\delta p}$ simultaneously with the constraint that these vectors must sum to their corresponding mascon values within a range defined by the diagonal mascon observation covariance R provided in the solution. This

approach may be compared with that of Seo et al. (2015), who use empirical orthogonal functions.

The following equations are solved, in which the observation operator H represents the point-wise addition of surface pressure and surface mass balance mascons. The covariance estimate P for x_{SMB} and $x_{\delta p}$ come from RACMO2.3 (Wessem et al., 2014) and ERA-Interim, respectively.

$$
\begin{aligned}
\mathbf{y}_i &= (\mathbf{x}_{SMB} + \mathbf{x}_{x_{\delta p}})_i \\
\mathbf{y}_i &= H\mathbf{x}_i \\
\mathbf{x} &= \begin{bmatrix} x_{SMB,i} \\ \\ x_{\delta p,i} \end{bmatrix} \\
H &= \begin{bmatrix} \mathbb{I} & \mathbb{I} \end{bmatrix} \\
P &= \begin{bmatrix} P_{SMB,SMB} & P_{\delta p,SMB} \\ \\ P_{SMB,\delta p} & P_{\delta p,\delta p} \end{bmatrix} \\
K &= PH^T(HPH^T + R)^{-1} \\
\hat{x}_i &= \mathbf{x}_{i-1} + K\left(\mathbf{y}_i - H\mathbf{x}_{i-1}\right)
\end{aligned}
$$

For improved solution stability, only mascons on the High Antarctic Plateau, where pressure error signals dominate, were assimilated. The broad-scale spatial correlations of these error signals were exploited to impute pressure estimates outside of the HAP. As the signal-to-noise ratio of SMB signals to pressure errors is low outside this region, this does not affect the overall solution. Correlations across time were not exploited, except by using the solution from the previous month as a prior.

The pressure retrieval over Antarctica is successful. The acceleration, trend, and annual cycle are shown in Figure 3.3 alongside forward predictions. Over the entire ice sheet, this total acceleration is 3.4 $\pm$ 1.0 Gt yr^{-2}, in line with the accelerations returned by other models (except the older reanalyses, Figure 3.3). This result is based on a fit weighted according to the solution uncertainties.

The RMS of pressure residuals relative to instruments is 14.4 mm, comparable to the 14.1

mm RMSE of GAA. Because each mascon represents the integrated pressure over a 100,000 km^2 quadrilateral, this RMS error includes the error of omission due to reduced spatial resolution. While GRACE itself may not offer improvement over GAA on monthly timescales, it may prove valuable in filling continent-scale gaps in pressure measurements over East Antarctica. Additionally, GRACE can capture drifts and biases in numerical weather models on longer timescales, as was demonstrated above.

Figure 3.5: Ratio of Antarctic surface pressure error standard deviation to surface mass balance standard deviation (upper left), which exceeds unity above elevations of 2500 meters; mascons corresponding to the region above 2500 meters (lower left); and predicted pressure error signal from optimal interpolation compared with time series of JPL mascons integrated over this region (right). While the mascon time series is considerably noisier than the predicted surface pressure errors, a quadratic fit to this time series agrees with the surface pressure error predictions, indicating the presence of this signal in the time series.

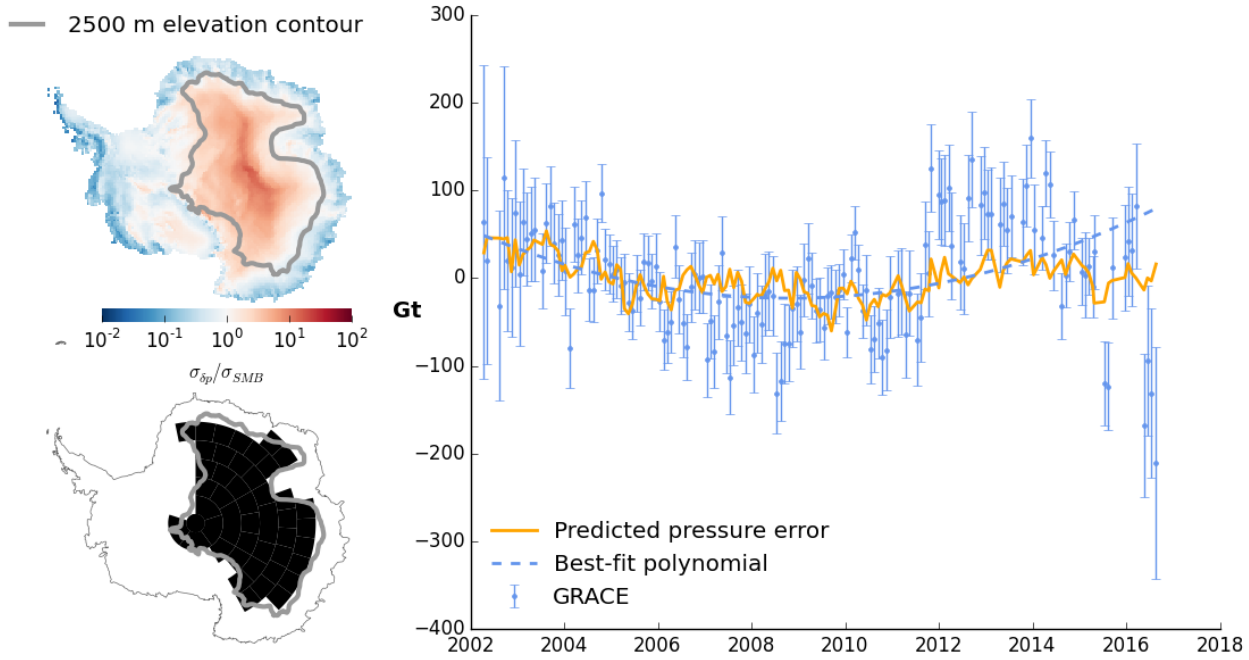

	Annual Cosine	Annual Sine	Acceleration	Trend	RMSE
	Gt	Gt	Gt yr^{-2}	Gt yr^{-1}	mm EWH
NCEP-DOE	-11.5 ± 11.0	-20.2 ± 10.7	4.9 ± 1.0	-0.0 ± 1.9	20.0
MERRA	-26.7 ± 7.5	-28.1 ± 7.3	8.6 ± 0.8	-4.0 ± 1.4	15.0
ERA-Interim	-34.6 ± 3.3	-32.9 ± 3.2	4.2 ± 0.3	-3.9 ± 0.6	12.8
MERRA-2	-7.4 ± 5.6	-28.5 ± 5.5	5.1 ± 0.5	-0.3 ± 1.0	13.5
JRA-55	-13.1 ± 5.9	-32.7 ± 5.7	3.2 ± 0.5	3.3 ± 1.0	13.3
Unweighted Ensemble	-18.4 ± 4.0	-31.4 ± 3.9	4.1 ± 0.4	-0.3 ± 0.7	12.7
Optimal	-5.7 ± 4.3	-9.8 ± 4.2	3.7 ± 0.4	1.0 ± 0.7	11.0
Ensemble Kalman Filter	-19.5 ± 4.4	-27.5 ± 4.4	4.0 ± 0.4	0.4 ± 0.8	12.2
GRACE Retrieval	35.3 ± 10.0	3.9 ± 9.7	3.4 ± 1.0	1.9 ± 1.8	14.4
AOD1B RL06	8.6 ± 3.4	-3.5 ± 3.3	1.7 ± 0.3	-2.9 ± 0.6	18.3

Table 3.1: Results of a simultaneous fit of trend, annual, and acceleration signals for selected models with respect to GAA integrated over the Antarctic ice sheet. AOD1B RL06 is evaluated by comparing GAC between RL05 and RL06 instead of GAA due to incompatible product definitions.

Chapter 4

Adjustment of Trends

This chapter focuses on separating signals from GIA and ice sheet processes in average trends observed by GRACE, ICESat, and GNSS data. The primary goal is separation of GIA and ice mass signals. GIA is the largest error source for the AIS.

4.1 Formulation of Data Combination over Antarctica

The basic estimation problem may be first stated as $\mathbf{y} = \mathbf{H}\mathbf{x}$, where $\mathbf{y}$ contains the observed ICESat, GRACE, and GNSS data; $\mathbf{x}$ contains a parameterization of a GIA model over the entire time period of interest and vectors of surface ice mass estimates for every time period in the estimation (e.g., every month); and H is a matrix of observation operators reflecting the effects of GIA, elastic loading, and total mass change at each of the observation locations. These functions contain the Green's functions of Farrell (1972) and are inherently linear.

In one formulation of this problem, the basic observation equation for observed GIA and elastic loading effects at time t_i with respect to reference time t_0 and ice mass state $\mathbf{x}_{\mathrm{ICE},0}$ is as follows:

$$\begin{bmatrix} \mathbf{y}_{\mathrm{GRACE,i}} - \mathbf{y}_{\mathrm{GRACE},0} \\ \mathbf{y}_{\mathrm{GPS,i}} - \mathbf{y}_{\mathrm{GPS},0} \\ \mathbf{y}_{\mathrm{ALT,i}} - \mathbf{y}_{\mathrm{ALT},0} \end{bmatrix} = \begin{bmatrix} (t_i - t_0)I & I \\ H^{\mathrm{GPS}}_{\mathrm{GIA}} & H^{\mathrm{GPS}}_{\mathrm{ICE}} \\ H^{\mathrm{ALT}}_{\mathrm{GIA}} & H^{\mathrm{ALT}}_{\mathrm{ICE}} \end{bmatrix}_i \begin{bmatrix} \mathbf{x}_{\mathrm{GIA}} \\ \mathbf{x}_{\mathrm{ICE,i}} - \mathbf{x}_{\mathrm{ICE},0} \end{bmatrix}, \tag{4.1}$$

This equation captures the entire problem of data combination on monthly timescales. It assumes that the parameterization of GIA and surface mass share the same physical dimensions (e.g., mm equivalent water height and mm equivalent water height per year) as the GRACE data to which they are compared. Note that the equation requires subtraction of data from an epoch common to all datasets. This registration against a common epoch bypasses the problem of estimating constant biases between datasets, but is difficult to implement when there is poor overlap between datasets. It also renders the data vulnerable to outliers present in the data at the reference epoch.

This observation equation may also be differentiated with respect to time to examine the entire problem in terms of linear rates of variation. This is an intuitive point of departure for exploring corrections to GIA models.

$$\begin{bmatrix} \dot{\mathbf{y}}_{\mathrm{GRACE}} \\ \dot{\mathbf{y}}_{\mathrm{GPS}} \\ \dot{\mathbf{y}}_{\mathrm{ALT}} \end{bmatrix} = \begin{bmatrix} I & I \\ H^{\mathrm{GPS}}_{\mathrm{GIA}} & H^{\mathrm{GPS}}_{\mathrm{ICE}} \\ H^{\mathrm{ALT}}_{\mathrm{GIA}} & H^{\mathrm{ALT}}_{\mathrm{ICE}} \end{bmatrix} \begin{bmatrix} \mathbf{x}_{\mathrm{GIA}} \\ \dot{\mathbf{x}}_{\mathrm{ICE}} \end{bmatrix}, \tag{4.2}$$

Differentiation also eliminates the need for a common epoch against which to reference the data, further simplifying the problem and maximizing the total amount of information included in the inversion. For this reason, two of the following sections in this chapter explore the data purely in terms of estimated rates.

There is wide flexibility for the choice of basis functions for the $\mathbf{x_{GIA}}$ and $\mathbf{x_{ICE}}$, format of the observation data, and the formulation of the observation functions. The models may be represented as radial basis function, spherical harmonics, or mascons. GRACE data may be represented in a similar basis. Altimetry data generally come in high volume and require a number of reduction steps to be computationally tractable. Multiple approaches exist for reducing altimetry data. The choice of basis functions, data formats, and observation functions carry distinct tradeoffs in computational efficiency, accuracy, and feasibility, which are explored in this chapter.

It is important to consider that this formulation treats firn compaction as a background process and assumes that its elevation change effects have been subtracted from y_{ALT}. Future work

on this problem will necessarily involve treating firn compaction as an unknown process to be solved for.

4.2 Modeling Considerations

There are a number of options for how the observation and mass state vectors are represented.

Spherical harmonics are orthogonal special functions defined over the entire surface of a sphere. As spherical harmonics are valid solutions of Laplace's equation in spherical coordinates, they are a natural basis for representing various aspects of geopotential fields. As such, they are the default representation scheme for GRACE gravity solutions and AOD1B geophysical fluid gravity models. As a spectral representation of the gravity field, spherical harmonics are easily convolved with Green's functions to examine other geodetic effects.

However, spherical harmonics are cumbersome if used within a limited spatial domain. Modeling Earth's full gravity field at maximum degree and order 60, for example, requires 3,721 independent coefficients, including degree 0. While these functions are necessarily orthogonal over a sphere, evaluating these functions over a limited spatial domain to generate a local solution imposes linear dependence between coefficients in the solution, introducing a computational inefficiency and an obstacle to direct interpretation. Antarctica accounts for less than 3% of Earth's surface, meaning that these 3,721 coefficients have only 100 or so degrees of freedom within its coastline.

The problem of linear dependence between spherical-harmonic coefficients is solved through the generation of Slepian functions within a domain. Slepian functions may be obtained through eigenvalue decomposition of a matrix of spherical-harmonic functions evaluated within a confined domain. Slepian decomposition of the gravity field within a limited domain can be useful for filtering noise sources, as has been demonstrated by Harig and Simons (2012). As Slepian functions may be represented both spatially and as spherical harmonics, it is straightforward to convolve these with Green's functions or perform spectral filtering operations.

Spherical-cap mascons are radially-symmetric representations of mass and surface elevation change. Their effects on geopoential and vertical crustal deformation are paraxial and vary only as

a function of distance from the cap. Mascons may be arbitrarily sized and distributed according to the availability of data or the spatial characteristics of the model.

Grids and other mesh configurations are also a viable way to represent mass variation, especially at high-resolution spatial scales of 20 km. Zammit-Mangion et al. (2013, 2015); Martín-Español et al. (2016b) explore different optimized mesh spacings for best capturing mass variation in Antarctica. One avenue for optimizing the distribution of solutions points involves taking advantage of lower characteristic length scales near the coasts of Antarctica for surface mass balance and firn compaction. These grids may also be parameterized by empirical orthogonal functions, which exploit linear dependence across space and time within a model to reduce its complex dynamics of to linear combinations of static spatial patterns.

4.3 Adjustment of GIA models with GNSS vertical motion rates

The first successful approach to this problem involved combining GNSS vertical motion with GRACE data to generate corrections to the IJ05 GIA model (Ivins et al., 2013). This was accomplished with a simplification of Equation 4.2 for observations $\mathbf{y}$ given model parameters $\mathbf{x}_{\mathrm{GRACE}}$ (total estimated mass) and $\mathbf{x}_{\mathrm{GIA}}$ (GIA correction) is

$$\mathbf{y} = H_{\mathrm{GIA}}\mathbf{x}_{\mathrm{GIA}} + H_{\mathrm{EWH}}(\mathbf{x}_{\mathrm{GRACE}} - \mathbf{x}_{\mathrm{GIA}}) \tag{4.3}$$

The operators H_{GIA} and H_{EWH} give the respective partial derivatives of elastic loading and GIA uplift at each observation site with respect to the parameters of each model. The individual parameter vectors may be isolated by rearrangement of the equations. This effectively combines the elastic loading and GIA observation operators into a single operator with respect to GIA.

$$\mathbf{y} = (H_{\mathrm{GIA}} - H_{\mathrm{EWH}})\mathbf{x}_{\mathrm{GIA}} + H_{\mathrm{EWH}}\mathbf{x}_{\mathrm{GRACE}} \tag{4.4}$$

For our purposes, the term $\mathbf{x}_{\mathrm{GRACE}}$ may be removed from the estimation and constrained to the GRACE covariance. This is the equivalent of adding the uncertainty of the potential to the

GIA covariance. This reduces the problem to estimation of corrections to the GIA model instead of both the GIA model and GRACE data. The observation equations may therefore be simplified and *a priori* estimates may be removed.

$$H = H_{\mathrm{GIA}} - H_{\mathrm{EWH}} \tag{4.5}$$

$$\delta\mathbf{y} = H\delta\hat{\mathbf{x}}_{\mathrm{GIA}} \tag{4.6}$$

$$\delta\mathbf{y} = \mathbf{y} - (H_{\mathrm{GIA}} - H_{\mathrm{EWH}})\bar{\mathbf{x}}_{\mathrm{GIA}} - H_{\mathrm{EWH}}\bar{\mathbf{x}}_{\mathrm{GRACE}} \tag{4.7}$$

The corrections are then obtained using least-squares adjustment.

$$\delta\hat{\mathbf{x}}_{\mathrm{GIA}} = PH^T(HPH^T + R)^{-1}\delta\mathbf{y} \tag{4.8}$$

This technique requires an estimate of the spatial statistics of both GIA models and total geopotential, represented by the covariance $P = P_{\mathrm{GRACE}} + P_{\mathrm{GIA}}$. The covariance of the geopotential P_{GRACE} comes from an estimate of the trend term in a simultaneous fit of a trend and annual signal to the original GRACE Stokes coefficients. These uncertainties may then be projected onto the basis functions used to represent mass variations.

The covariance of GIA, P_{GIA}, is more difficult to estimate, but is critical to generating corrections to GIA models statistically consistent with commonly-used forward models. To this end, a small ensemble of six publicly available forward GIA models was used, including the W12a L/B/U models (Whitehouse et al., 2012), IJ05.R2 (Ivins et al., 2013), and two versions of the ICE-6G model by (Peltier et al., 2015) and Purcell et al. (2016) as shown in Figure 4.1. The mean and standard deviation of this ensemble are shown in Figure 4.2.

For the purpose of this inversion, GNSS sites on the Antarctic Peninsula were excluded from the analysis. The Antarctic Peninsula is known to have a distinct mantle viscosity profile not captured by any of the ensemble members (Barletta et al., 2018).

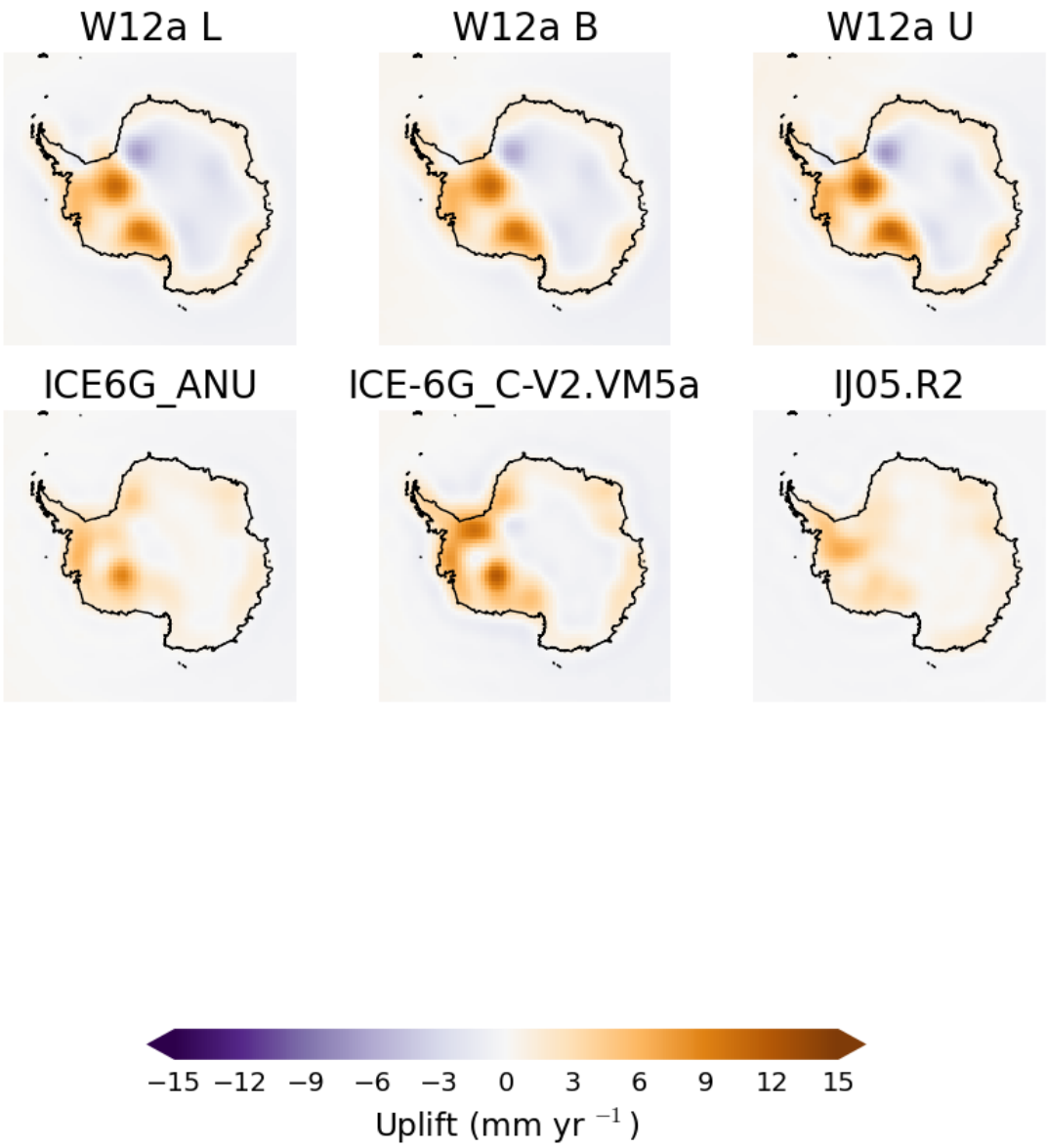

Figure 4.1: GIA ensemble members

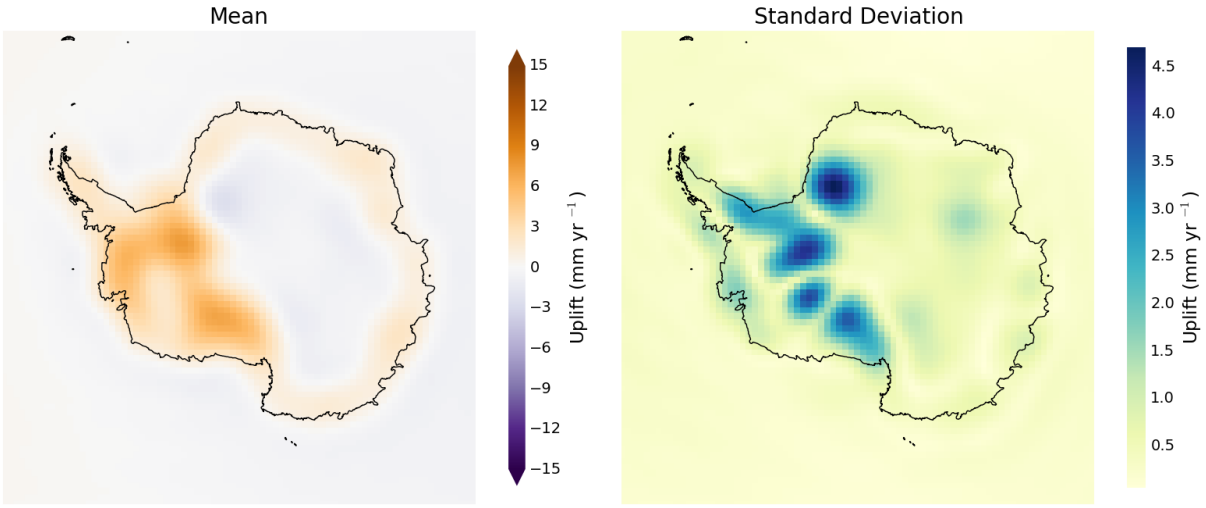

Figure 4.2: Mean and standard deviation of the GIA ensemble

4.3.1 Parameterization

While GRACE geopotential models are distributed in terms of spherical harmonics, it is preferable to work in the spatial domain. In this analysis, GIA and mass loss are therefore parameterized in terms of mass concentrations (mascons), similar to the approach of JPL (Watkins et al., 2015). Each mascon is a spherical cap of uniform mass loading with a diameter of 3 degrees. The mascons are confined to land and the area under ice shelves to capture GIA. GIA and ice mass change are modeled as separate layers of spherical caps. The sum of each set of caps is equal to total surface mass as yielded by retrieval from GRACE geopotential fields with the methods of Wahr et al. (1998). The spatial configuration of these caps is given in Figure 4.4. The variable captured by each mascon is the rate of equivalent water height change within its boundaries. The uplift due to this mass change is computed from the spherical-harmonic decomposition of each mascon, using functions and coefficients given by Purcell et al. (2011) for GIA and Farrell (1972) for elastic loading.

Each spherical cap may be decomposed into a set of dimensionless spherical-harmonic coefficients $\bar{\Gamma}_{i,lm}$, where i is the index of the cap, l is the spherical-harmonic degree and m is the spherical-harmonic order. In this implementation, the spherical caps are decomposed to degree and order 60. While higher-degree implementation using radial Legendre polynomials is possible, spherical harmonics are more straightforward to work with in this setup. The surface density σ_i of each cap may be computed from GRACE spherical harmonics C_{lm} and S_{lm} as,

$$\sigma_i = \frac{R\rho_E}{3} \sum_{l=2}^{\infty} \frac{2l+1}{1+k_l^E} \sum_{m=0}^{l} \bar{\Gamma}_{i,lm} \begin{bmatrix} C_{lm} \\ S_{lm} \end{bmatrix} \tag{4.9}$$

.

Here, k_l^E is a set of elastic loading Love numbers describing the deformation of the crust in response to surface loads, R is the equatorial radius of Earth, and ρ_E is the average density of Earth.

The effect of GIA from one spherical cap measured at an angular distance α from its center

is,

$$\delta r(\alpha, \delta\sigma_i)_{\text{GIA}} \approx \frac{3}{\rho_E} \sum_{l=2}^{\infty} \frac{h_l^{VE}}{k_l^{VE}} \frac{1+k_l^E}{2l+1} \Gamma_l P_l(\cos\alpha) \delta\sigma_i \tag{4.10}$$

.

In the above equation, the fictitious elastic loading term contained in the GIA mass estimate (for dimensional compatibility with land ice mass) is removed and replaced with more appropriate viscoelastic Love numbers h_l^{VE}, k_l^{VE}, the ratio of which approaches $\frac{2l+1}{2}$ over sufficiently long timescales. Because of this approximation, the effect of 1 mm EWH of GIA detected by GRACE results in approximately 0.3 mm of vertical uplift. However, truncation errors reduce the actual scale of this effect and introduce substantial Gibbs phenomena.

The effect of ice mass change of a single spherical cap on elastic loading is given by

$$\delta r(\alpha, \delta\sigma_i)_{\text{elastic}} = \frac{3}{\rho_E} \sum_{l=2}^{\infty} \frac{h_l^E}{2l+1} \Gamma_l P_l(\cos\alpha) \delta\sigma_i. \tag{4.11}$$

From this parameterization, it is straightforward to compute the observation operators H_{GIA} and H_{EWH} as matrices of the partial derivatives of these expressions with respect to the surface densities of each spherical cap.

The Green's functions for elastic loading converge quickly at when truncated at degree 60, but do not converge as quickly for GIA. This is illustrated in Figure 4.3. Consequently, the uplift pattern from a uniform disk of GIA loading is subject to ringing artifacts. In terms of magnitude, a unit variation in mass observed by GRACE has a much larger effect in terms of uplift when interpreted as GIA than when interpreted as elastic loading. GNSS position measurements are therefore much more sensitive to GIA than changes in ice mass.

Because the vertical motion load Love number h_l^E converges quickly to a finite value of -5.2 as l approaches ∞, this function converges much more quickly than the expression for GIA effects. From the sign of this value, it is readily apparent that a unit change in GIA as measured by GRACE has the *opposite* effect on vertical bedrock motion as an equivalent change in ice mass.

The above parameterization is set up for use with the CSR RL05 spherical-harmonic GRACE products. The rest of this work uses JPL RL05.1M mascon solution, requiring an alternative basis to be set up for this data. For the same reasons the full set of spherical harmonics are eschewed, using the full mascon dataset would be too cumbersome. Instead, only the 148 mascons covering the grounded portion of the Antarctic ice sheet are sampled. The mascons may be further subdivided into land and ocean components according to the quarter-degree cylindrical land mask accompanying the solution. The mascon solutions are processed so mascons straddling both ocean and land may disaggregated into land and ocean components, leveraging constraints from surrounding mascons of each category. The algorithm for this, the "coastline resolution improvement" (CRI) filter is detailed in Wiese et al. (2016). The locations and spans of these subsampled mascons over Antarctica are detailed in Figure 2.3.

For each of the 156 GRACE months contributing to the solution, the value of land components of the 148 AIS mascons are assigned to a vector representing the available data for that month. Uplift Green's functions for these mascons are available and computed to degree and order 100. The boundaries of these mascons are retained for "mascon averaging" operations to construct observation operators relating solution mass distributions to observed GRACE data. These land mascons provide both convenient basis functions for GRACE data and low-resolution mass solutions.

4.3.2 Results

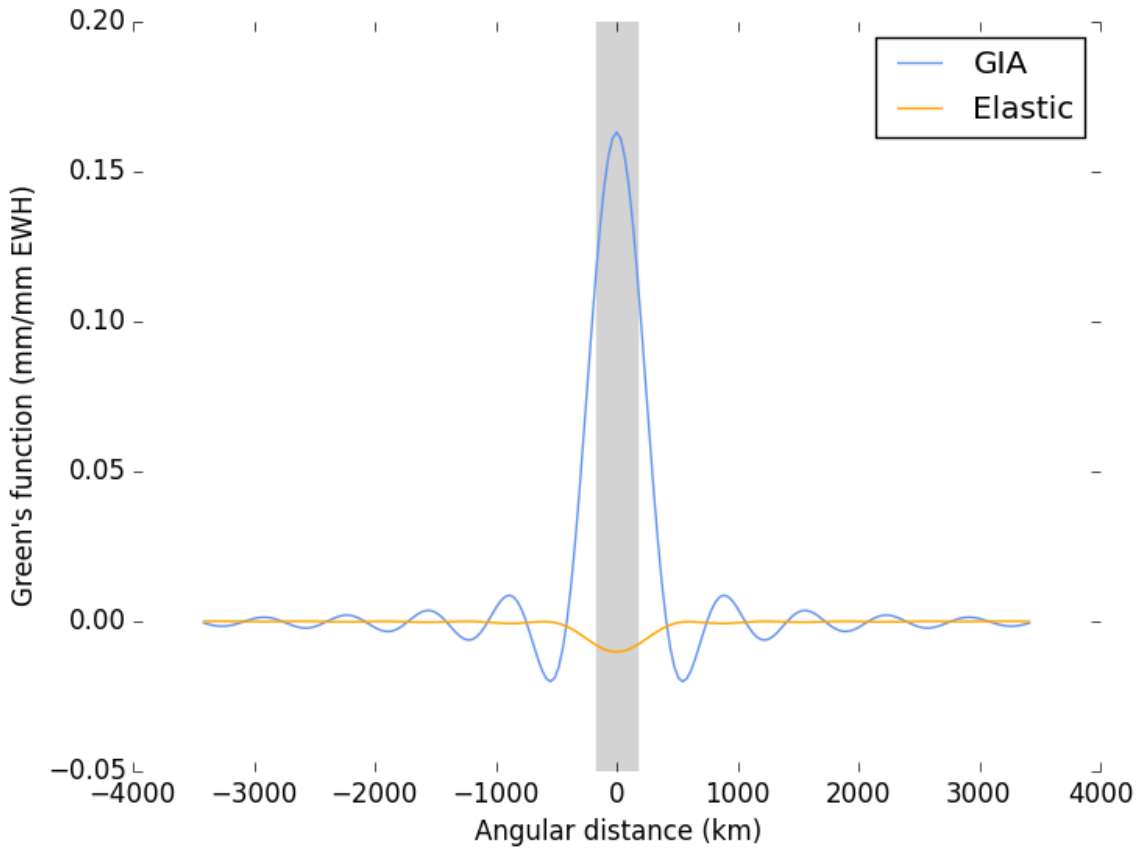

Figure 4.3: Partial derivatives of vertical motion (attributed to either GIA or elastic loading) with respect to a change in equivalent water thickness of a spherical cap with a 300 km diameter as a function of great-circle distance from the center of the cap. This illustrates the high sensitivity of GPS to GIA signals.

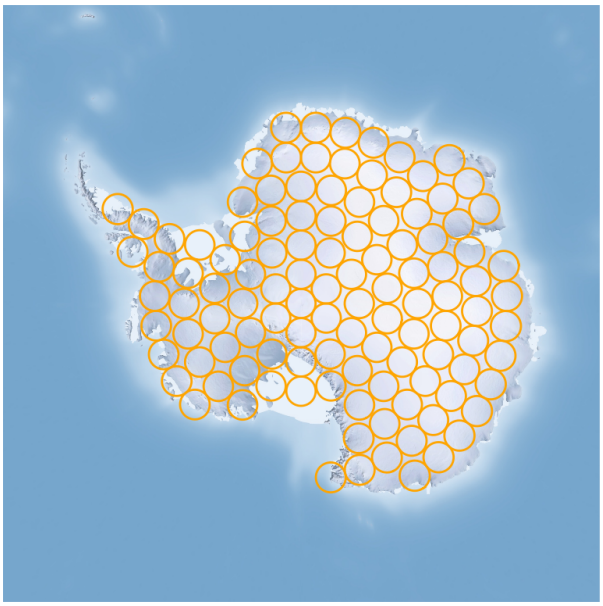

Figure 4.4: Locations and spatial extents of spherical caps used for the initial analysis of GNSS and GRACE data

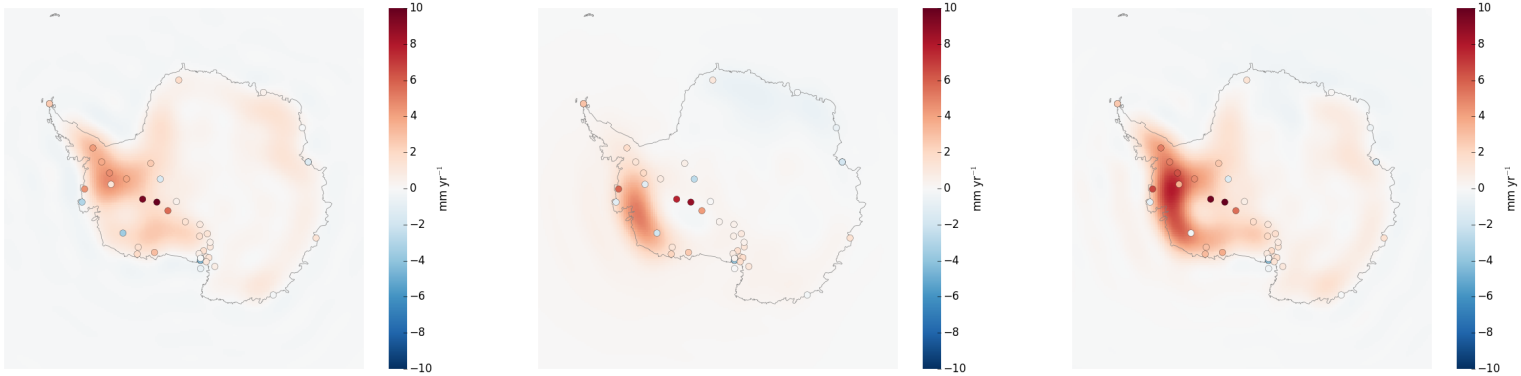

(a) GIA (IJ05.R2). Elastic loading removed from GPS vertical velocities.

(b) Surface water loading (GRACE minus IJ05.R2). GIA uplift removed from GPS vertical velocities.

(c) GIA plus loading compared with raw GPS velocities

Figure 4.5: Vertical velocity predictions from a priori models plotted against GPS vertical velocity measurements corrected for models not included in each plot.

Model	GIA Gt yr^{-1}	Ice (2002–2017) Gt yr^{-1}
A et al. (2013) + JPL RL05.1M	112	-201
GRACE + GNSS	85	-173

Table 4.1: GIA and ice sheet mass trends for 2002–2017 obtained using a combination of GNSS and GRACE data

Pre-fit models and data for the spherical-cap solution are shown in Figure 4.5. Corrections to the reference GIA model and postfit residuals are given in Figure 4.6 and the total corrected GIA model is shown in Figure 4.7.

The spherical-cap method yields a correction of the GIA model of -8.5 $\pm$ 3.6 Gt yr^{-1}, taking the current estimate of Antarctic mass change using CSR RL05 and IJ05 from -100 Gt yr^{-1} to -91 Gt yr^{-1} between 2002 and 2016. The corrections to the model explain 47% of the variance in the prefit residuals and leave postfit residuals with a weighted RMS scatter of 1.0 mm yr^{-1}. While the total change in mass loss rate is not significant, the new spatial patterns introduced by the new data are noteworthy and do not contradict expectations.

One of the key limitations of this method is the manner in which the covariance of GIA was estimated. Using only six GIA models from four authors affords only five effective degrees of freedom in the covariance matrix. Given the high number of GNSS stations used in the solution, this leaves the solution spatially overconstrained.

The Caron et al. (2018) GIA covariance estimate provides an alternative to the ensemble-based approach to estimate the GIA covariance used in this modeling procedure. The covariance matrix of the Caron et al. (2018) solution is dominated by a single spatial pattern. The first eigenvalue of its Antarctic components accounts for more than 90% of the overall variance. This product is available, but not used in this analysis for now.

This method was repeated with a land-mascon basis functions with JPL RL05.1M mascons as inputs. Aside from the input data and choice of basis functions, this solution differs from the previous solution in the way that GIA uplift is handled. Results are shown in Figure 4.8 and tabulated in Table 4.1.

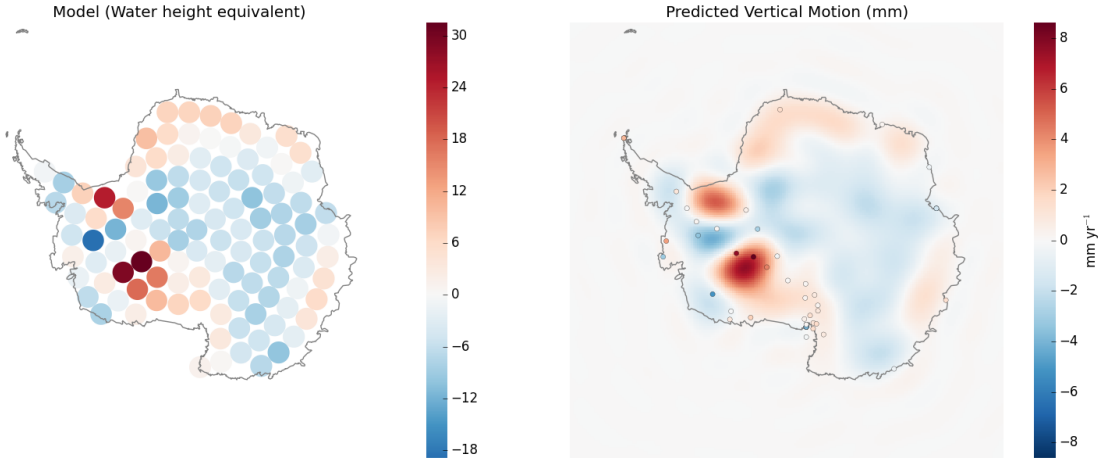

Figure 4.6: Postfit corrections to the IJ05.R2 GIA model parameters (left, units: mm EWH) and predicted uplift deviations plotted alongside GPS vertical velocity prefit residuals.

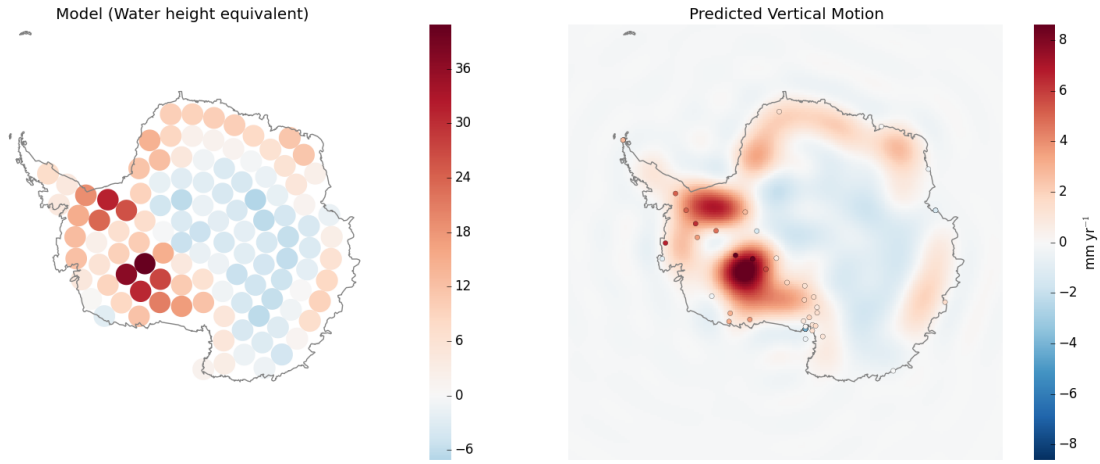

Figure 4.7: Postfit corrections to the IJ05.R2 GIA model parameters with IJ05.R2 added back (left, units: mm EWH) and predicted uplift rates plotted alongside GPS vertical velocities.

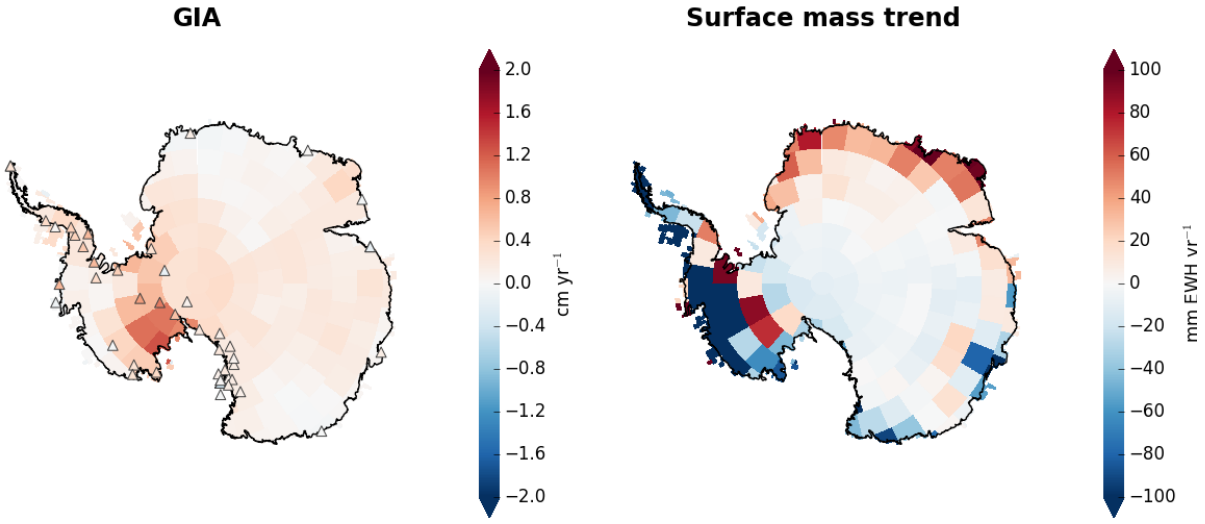

Figure 4.8: Left: Mascon-averaged GIA solutions obtained from combination of GRACE, GIA, and GPS ensembles and predicted uplift rates plotted alongside GPS vertical velocities. Right: Land surface ice mass balance for solution.

Instead of using asymptotic approximations for GIA uplift Green's functions, this solution method attempts to account for lateral variation in mantle properties with spatially-dependent estimates for effective bedrock density. For each mascon, the uplift and equivalent-water-height components of the A et al. (2013) GIA model (so chosen for its 3D Earth structure) are isolated and linearly regressed against each other to obtain an effective density for each mascon. The densities span 3000–4000 kg m^{-3}, consistent with the range of densities imposed by Riva et al. (2009). The densities are presented in Figure 4.10e. The GIA component of uplift for a GPS site on each mascon may be computed by dividing the equivalent water height rate for the GIA signal predicted for the geographically closest mascon by that effective density. The problem setup remains identical to the previous method, except for the aforementioned change in basis functions and GIA Green's functions.

This solution method outperforms the other method and the solution fields explain 73% of the variance in the GNSS trends, reducing the standard deviation from 2.7 mm yr^{-1} to 1.4 mm yr^{-1}. Formal uncertainty estimates for total mass loss from both methods are unexpectedly small and are roughly ± 2 Gt yr^{-1}. The solution estimates are presented without uncertainties to avoid a false impression of precision.

The methods presented in this section demonstrate the feasibility of adjusting GIA models with bedrock-mounted GPS position time series and constraints on GIA models.

4.4 Combination of ICESat surface elevation rates with GRACE mass change rates

This section describes attempts to duplicate combination of GRACE and ICESat by Riva et al. (2009) and Gunter et al. (2014) to generate an empirical GIA model and a corresponding estimate of ice sheet mass loss. This combination uses gridded ICESat elevation rate data between 2003 and 2009 and equivalent water height change rates estimates from GRACE data available in the same time period.

GRACE and ICESat sense combined effects of changes in local surface density with differing

spatial resolutions and sensitivities. For any given point in Antarctica, the observation equation for rate of surface density change detected by GRACE is

$$\dot{\sigma} = \dot{\sigma}_{\mathrm{GIA}} + \dot{\sigma}_{\mathrm{Ice}} \tag{4.12}$$

.

If $\dot{\sigma}$ is the product of an elevation change rate and an effective density of a medium, then this equation may be rephrased as

$$\dot{\sigma} = \rho_{\mathrm{GIA}}\dot{h}_{\mathrm{GIA}} + \rho_{\mathrm{Surface}}\dot{h}_{\mathrm{Ice}} \tag{4.13}$$

,

and the observation equation for observed altimetry elevation rates is,

$$\dot{h} = \dot{h}_{\mathrm{GIA}} + \dot{h}_{\mathrm{Ice}} \tag{4.14}$$

The effective densities ρ_{GIA} and ρ_{Surface} differ by nearly an order of magnitude. ρ_{GIA} is approximately $\frac{2}{3}$ the average density of Earth (Wahr et al., 1995), or 3700 kg m^{-3}, while the effective density of snow or ice at the ice sheet surface ranges between 300 and 917 kg m^{-3}, depending on the state of firn compaction at the ice surface. This density contrast renders ICESat much more sensitive to changes in ice sheet elevation than GRACE for an equivalent change in mass. More importantly, the density contrast makes the above set of equations invertible everywhere over the Antarctic ice sheet. The rate of GIA elevation change may be solved at any location as,

$$\dot{h}_{GIA} = \frac{\dot{\sigma} - \dot{h}\rho_{\mathrm{Surface}}}{\rho_{\mathrm{GIA}} - \rho_{\mathrm{Surface}}} \tag{4.15}$$

,

and the rate of ice sheet mass loss may be rendered as,

$$\dot{\sigma}_{\mathrm{Ice}} = \dot{\sigma} - \dot{h}_{\mathrm{GIA}}\rho_{\mathrm{GIA}} \tag{4.16}$$

.

Given a measurement of surface elevation rate and a corresponding equivalent water height change rate, it is possible to separate GIA and ice sheet processes in both signals. The primary difficulty in this approach lies in the estimation of the effective densities associated with both GIA and ice sheet processes. Due to firn compaction, the effective ice surface density varies in both space and time.

Effective solid-Earth density is also uncertain. While the partial derivative relating GIA-induced bedrock elevation change is unique to all GIA models, an acceptable rule of thumb is that this value asymptotically converges to $\frac{2}{3}$ the average density of Earth as the GIA model run time approaches infinity. Riva et al. (2009) find that this effective density varies between 3400 kg m^{-3} over oceans and 4000 kg m^{-3} over land due to self-attraction and loading effects. They approximate the transition between land and ocean density using Gaussian smoothing.

The time-dependence of surface density due to firn compaction can be mitigated using a firn-compaction model and a corresponding model of surface mass balance (SMB). Gunter et al. (2014) modify the formulation of an empirical GIA solution to include these models:

$$\dot{h}_{\mathrm{GIA}} = \frac{\dot{\sigma} - \dot{\sigma}_{\mathrm{SMB}} - (\dot{h} - \dot{h}_{\mathrm{Firn}})\rho_{\mathrm{Surface}}}{\rho_{\mathrm{GIA}} - \rho_{\mathrm{Surface}}} \tag{4.17}$$

.

In this formulation, $\dot{\sigma}_{\mathrm{SMB}}$ is the average anomaly of surface mass balance rate within the 2003–2009 time period of interest relative to the average rate of surface mass accumulation and $\dot{h}_{\mathrm{Firn}}$ is the average rate of firn elevation change within the corresponding period. The RACMO2.3 SMB outputs produced by Lenaerts et al. (2013) and Wessem et al. (2014) were used, which include outputs of a firn compaction model initially devised by Ligtenberg et al. (2011).

4.4.1 Reduction of ICESat Data

In duplicating the Gunter/Riva method, it was necessary to reproduce their reduction and gridding of ICESat data. Gridded ICESat data are necessary for direct comparison with GRACE

data.

Three primary methods exist for reducing altimetry data: the crossover method, the repeat-track method, and the overlapping-footprint method. Felikson et al. (2017) give a substantial overview of these methods applied to Greenland.

The crossover method involves identifying laser shots that fall within a defined radius of a known point corresponding to the intersection of two reference ground tracks. A plane is fit to the elevations of points identified within this distance to approximate the topographic slope and the residuals to this spatial fit may be interpreted as variations in surface elevation across time. The crossover method has the advantage of computational and conceptual simplicity. It is straightforward to implement and may be computed with limited resources. However, the spacing between crossovers increases at low latitudes, resulting in reduced spatial resolution near coastlines, where ice mass loss is most likely to occur. The crossover method also discards laser shots far from the crossover locations, potentially wasting useful data. Furthermore, any linear dependence between the time variation of elevation and the locations of individual footprints about a crossover point may confound the estimate of the topographic slope.

The repeat-track method locates laser shots within a specified cross-track distance of segments of the reference ground track. The assembled points are partitioned into along-track bins and the topographic slope within each bin is estimated such that the residuals may be interpreted as time variations in surface elevation. This technique uses more data than the crossover method and consequently has the advantage of higher resolution at low latitudes. It is therefore more capable of detecting coastal surface elevation change than the crossover method.

The overlapping-footprint (OFP) method searches the entire elevation measurement dataset for laser shot footprints that are co-located such that the sum of their campaign footprint radii (50–70 meters) is less than the distance between their centroids. If this condition is met, the shot footprints are determined to be overlapping. Overlap between laser shots means that they are sensing elevations from the same points in space and the difference between their respective elevation measurements may be interpreted as direct elevation change. While topographic slope correction

is possible, this method may be practically implemented without such corrections. This method contains fewer assumptions about topography than the repeat-track and crossover methods. Furthermore, it does not depend on prior knowledge of the groundtrack, enabling the use of data from the Laser 1a/b campaign in which ICESat was in an 8-day repeat orbit. Its primary disadvantage is the brute-force nature of the computation required to find all overlapping footprints.

Because of the higher resolution afforded by the OFP method, it was decided that this method would be used to extract elevation change signals from the ICESat data, as was done by Riva et al. (2009) and Gunter et al. (2014).

The reduction process was initiated with the GLAH12 geolocated elevation dataset. Before searching for overlapping footprints, several data editing tasks were performed, following Gunter et al. (2014). The saturation corrections present in the elevation datasets were subtracted from the elevation data. Data with co-elevations of more than 0.45° and data points flagged for multiple peaks were excluded.

The search for overlapping footprints was performed by comparing data from different days of observations. Neighboring footprints within pairs of observation days were located using k-d trees. To eliminate redundancy and save computing time, data from the same day were not compared. For each shot pair, the search records the mean position of the footprint pair, the distance between the footprints, the timestamp of each shot, and the difference in elevation between the shots.

The search found over 350 million valid OFP pairs. These OFP pairs contain redundant spatial and temporal information and are best gridded for comparison with GRACE data. A pole-centered stereographic grid with a spacing of 27 km, consistent with crossover spacing, was chosen to bin the data. This grid was used through this work to be consistent with the input ICESat data. After Gunter et al. (2014), shot pairs with an apparent elevation rate of more than 12 meters per year were excluded from the binning process, as this rate exceeds any known ice sheet process. The degree of overlap between neighboring ICESat footprints, a function of their radii and the distance between them, was computed according to the formulation for exoplanet transit depth given by Mandel and Agol (2002) and used as a weight in the computation of the binned average. The use

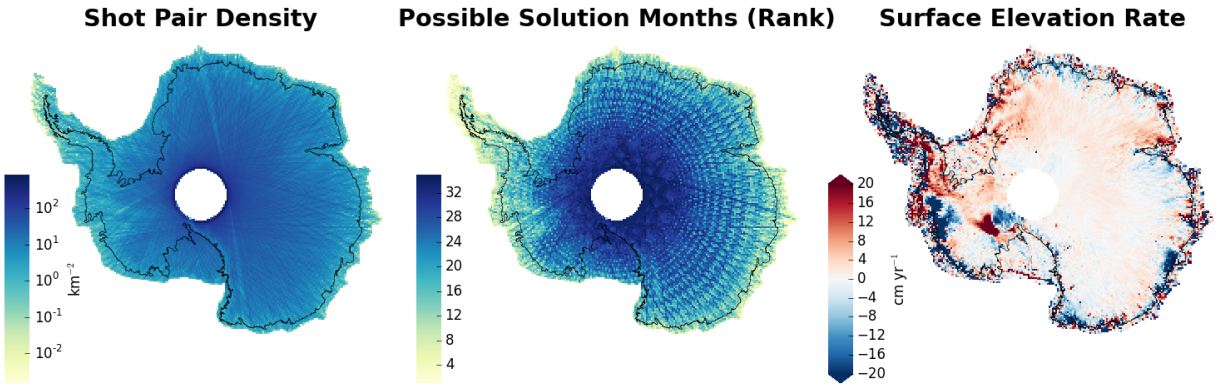

Figure 4.9: Left: Overall density of overlapping footprints used to generate monthly ICESat solution between 2003 and 2009. Center: Number of GRACE months in which ICESat elevation changes are able to be computed. Right: Best-fit surface elevation rate from overlapping footprints.

of overlap weighting is essential for valid elevation change solutions.

These elevation difference grids were then processed via least squares fit with the time difference between campaign pairs as the independent variable to obtain a map of surface elevation trends. The 2003–2009 trend, overall pair density, number of solutions months per grid cell are illustrated in Figure 4.9.

Following Gunter et al. (2014), the solutions are corrected for campaign bias using the low-precipitation zone on the High Antarctic Plateau as a calibration target. The corrected trend map is shown in Figure 4.10.

4.4.2 Solution for GIA with GRACE and ICESat

Having secured a valid ICESat trend for 2003–2009 and GRACE rates for the corresponding period, it is possible to disaggregate GIA and land-ice mass variation according to the method of Gunter et al. (2014). All ingredients used for this combination are shown in Figure 4.10.

Starting with GRACE mass trends from the CRI-filtered JPL RL05.1M mascon solutions (Watkins et al., 2015), the 2003–2009 trend is computed and mascon-averaged GIA signals are restored to yield the total mass flux trend signal over Antarctica, shown in Figure 4.10a. The difference between the 2003–2009 average of RACMO SMB and the average of RACMO over its

entire time period of 1979–2015 is computed and mascon averaged to obtain the grid of SMB anomaly rates shown in Figure 4.10b. These fields are differenced to obtain Figure 4.10g.

Trends from 2003–2009 ICESat data processed in the previous section are shown in Figure 4.10c. A campaign bias correction of 10.5 mm yr^{-1} has been subtracted from these trends, following the low-precipitation zone calibration method of Gunter et al. (2014). The Ligtenberg et al. (2011) firn densification trend shown in Figure 4.10d is subtracted from the ICESat trend map to obtain the data shown in Figure 4.10h. Gunter et al. (2014) use difference between the ICESat elevation rate and the firn surface elevation rate used to determine whether to use the density model of Kaspers et al. (2004), a solid ice density of 917 kg m^{-3}, or zero density. The approach presented here differs in that regions lying within the exposed bedrock mask (Fretwell et al., 2013) are given zero density. In further contrast with Gunter et al. (2014), the rule for assigning zero density to a grid cell based on agreement between the firn model and ICESat is ignored to illustrate an extreme solution. The snow density model is shown in Figure 4.10f.

The mascon-averaged effective mantle density is shown in Figure 4.10e. These densities come from a local regression of predicted uplift and predicted equivalent water height variation of the A et al. (2013) GIA model within each mascon. Because the A et al. (2013) model has lateral variations in mantle structure, the modeled density may accurately reflect effective mantle density.

The altimetry data in Figure 4.10h are multiplied by the density distribution in Figure 4.10f and then mascon-averaged so it may be compared with Figure 4.10g. The data in these two subfigures are then differenced, divided by the difference between the effective mantle density and effective surface density, and elastically corrected to obtain the uplift rate from GIA shown in Figure 4.10i. This GIA model is compared with elastically corrected GNSS vertical motion data as a validation step. To obtain surface mass change, this GIA model is multiplied by the effective mantle density and subtracted from the total mass signal in Figure 4.10a.

The final results are shown in Figures 4.10i and 4.10j. The resultant GIA model shows an unexpected negative trend in West Antarctica and positive trends in East Antarctica. Surface mass changes line up with expectations, particularly near the Amundsen coast and Totten glacier, where

Model	GIA Gt yr^{-1}	Ice (2003–2009) Gt yr^{-1}
A et al. (2013) + JPL RL05.1M	112	-153
GRACE + ICESat	108	-148

Table 4.2: GIA and ice sheet mass trends for 2003–2009 obtained using a combination of ICESat and GRACE data

strong mass loss signals are present.

Results also diverge from both expectations and those of Gunter et al. (2014). Total ice mass loss is 148 Gt yr^{-1} compared with 153 Gt yr^{-1} from the original mascon solution. The total mass signal from the solution GIA is 108 Gt yr^{-1}, comparable with the original A et al. (2013) model, but more than twice the value found by Gunter et al. (2014). The standard deviation of the prefit residuals of elastically-corrected GNSS vertical velocities is 2.6 mm yr^{-1}, but this error increases to 10.2 mm yr^{-1}. after the solution. These results indicate unsuccessful replication of the results of Gunter et al. (2014) and Riva et al. (2009). The reasons for this disagreement have not yet been established. Reliable uncertainty estimates are also not available at present. Like with the GNSS combination, the formal uncertainties not realistic enough to present alongside the data.

The approach of Gunter et al. (2014) and Riva et al. (2009) is replicated in this chapter, but the final results differ somewhat from theirs.

With refinement, the methods used to combine data over Antarctica may be applied to other regions where ice mass change signals are recorded by gravity, altimetry, and dense GNSS observation sites, such as the Greenland Ice Sheet, southern Alaska, and Iceland. Monitoring mass change enables prediction of crustal deformation and geoid height change, a problem of interest to authorities charged with maintaining vertical datums with accuracy requirements of 1 cm within a timespan of a decade. In Antarctica, both geoid heights and bedrock elevations change by more than a centimeter per decade, due to a combination of elastic loading and GIA. This mirrors the magnitude of geoid and elevation change in North America (Jacob et al., 2011).

Figure 4.10: Input data, models, and results for combination of GRACE and ICESat trends to obtain an empirical GIA model and surface mass trend between 2003 and 2009.
a GRACE total mass trend from CRI-filtered JPL mascons with mascon-averaged A et al. (2013) GIA model restored
b Mascon-averaged average of RACMO SMB anomaly over 2003–2009 interval
c Gridded ICESat surface elevation change rate over 2003–2009 interval with campaign bias correction
d RACMO firn densification rate over 2003–2009 interval
e Mascon-averaged bedrock density estimate for relating rate of surface uplift to rate of apparent equivalent water height change from GIA
f Inferred density of surface snow and ice based on comparing ICESat elevation rates with the firn model. Effective density is set to zero over regions known to consist primarily of exposed bedrock.
g Difference between **a** and **b**
h Difference between **c** and **d**
i Solution for GIA uplift rates from combination of above data. Elastically corrected GNSS data shown for comparison.
j Solution for ice mass change rates from combination of above data

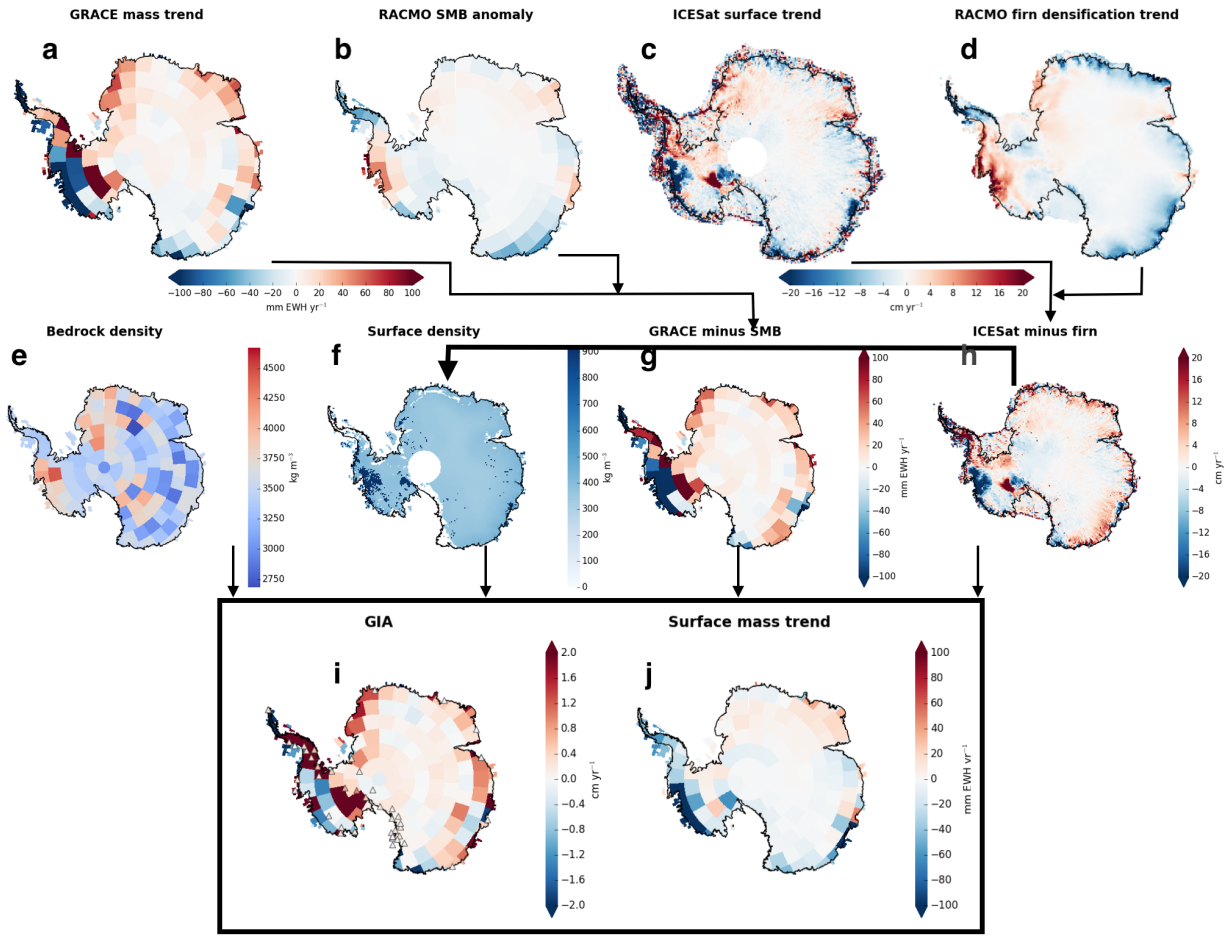

4.4.3 Separation of ice dynamics and SMB signals in GRACE data

Thus far, we have explored methods for separating ice mass change signals from glacial isostatic adjustment in GRACE data. Ice mass change signals have two components: ice dynamics and surface mass balance. These processes may be distinguished by where they tend to dominate signals. Because gravity and elevation signals caused by ice dynamics are primarily due to horizontal transport, InSAR-derived horizontal ice velocity maps may be used to create ice dynamics constraints.

If the ice sheet is decomposed into layers of ice dynamics and surface mass balance, the observation equation is

$$\dot{\mathbf{y}}_{\mathrm{GRACE}} = H \begin{bmatrix} \dot{\mathbf{x}}_{\mathrm{SMB}} \\ \dot{\mathbf{x}}_{\mathrm{ice}} \end{bmatrix}, \tag{4.18}$$

where

$$H = \begin{bmatrix} \delta_{ij} & \delta_{ij} \end{bmatrix}, \tag{4.19}$$

δ_{ij} is the Kronecker delta function, $\dot{\mathbf{y}}_{\mathrm{GRACE}}$ is the 2002–2017 trend for the 148 land mascons, and the vectors $\dot{\mathbf{x}}_{\mathrm{SMB}}$, $\dot{\mathbf{x}}_{\mathrm{ice}}$ represent the average equivalent water height variations in ice dynamics and SMB. With no additional information, it is impossible to disaggregate $\dot{\mathbf{x}}_{\mathrm{SMB}}$ and $\dot{\mathbf{x}}_{\mathrm{ice}}$ from their sum. However, spatial statistics from models of SMB and ice dynamics can make the problem tractable. Following Zammit-Mangion et al. (2013), InSAR horizontal velocity data from Rignot et al. (2011) are used to identify the parts of the mascons with significant ice dynamics contributions. Where horizontal velocity is found to be greater than 10 m yr $^{-1}$ the variance of the ice dynamics at that spot is assigned a value of (15,000 mm EWH)^2, after Zammit-Mangion et al. (2013). The area of each mascon with horizontal ice velocity above this threshold his tabulated. It is tempting to quantify ice dynamics variability using the divergence of the Rignot et al. (2011) horizontal velocities, but the noise in the resulting product is too excessive to be useful. The horizontal ice velocities and resultant ice mask used in this work are shown in Figure 4.11.

The observation operator is rewritten such that H considers the fraction of a mascon's area occupied by a the ice dynamics mask.

$$H = h_{ij} = \begin{bmatrix} \delta_{ij} & \frac{A_{\text{ice,i}}}{A_{\text{mascon,i}}}\delta_{ij} \end{bmatrix} \tag{4.20}$$

Note that the observation equation does not consider surface mass balance and SMB mutually exclusive. The area in which ice dynamics are applicable within a mascon may be limited to less than the area of the mascon, but SMB may affect the entire mascon.

The *a priori* covariance is then computed:

$$P = \begin{bmatrix} P_{\text{SMB}} & 0 \\ 0 & P_{\text{ice}} \end{bmatrix} \tag{4.21}$$

While P_{SMB} may be estimated directly from RACMO, RACMO contains the full SMB signal, which is on the order 2,000 Gt yr^{-1}. To estimate P_{SMB}, the sample covariance in the trend of the Ligtenberg et al. (2011) model firn model is scaled by the average density of Antarctic surface snow (300 kg m^{-3}) and divided by the variance of the timestamps in the GRACE time series to reflect the variability of the rate of surface mass balance in time.

The solution is obtained iteratively using constrained least squares:

$$\begin{bmatrix} \dot{\mathbf{x}}_{\text{SMB,k+1}} \\ \dot{\mathbf{x}}_{\text{ice,k+1}} \end{bmatrix} = (H^T W H + P^{-1})^{-1} \left(\dot{\mathbf{y}}_{\text{GRACE}} - H \begin{bmatrix} \dot{\mathbf{x}}_{\text{SMB,k}} \\ \dot{\mathbf{x}}_{\text{ice,k}} \end{bmatrix} \right) + \begin{bmatrix} \dot{\mathbf{x}}_{\text{SMB,k}} \\ \dot{\mathbf{x}}_{\text{ice,k}} \end{bmatrix} \tag{4.22}$$

A solution based on the IJ05 GIA model is shown in Figure 4.12. As expected, the ice dynamics component has strong negative signals near the Pine Island, Thwaites, and Totten Glaciers and strong positive signals on in the vicinity of the Kamb Ice Stream. The smoother, spatially correlated SMB component is characterized by strong long-wavelength signals lining the coast of East Antarctica.

The solution is dependent on the choice of GIA model. This method was repeated with various GRACE inputs with an ensemble of eight GIA models, including Caron et al. (2018) and A

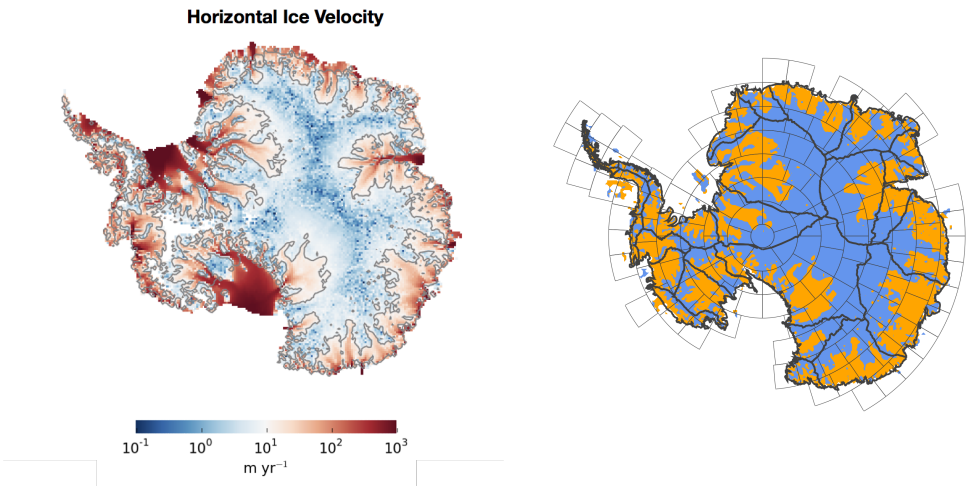

Figure 4.11: Left: Horizontal ice velocities obtained from InSAR measurements (Rignot et al., 2011). Right: Ice dynamics mask (orange) for horizontal velocities greater than 10 m yr^{-1}.

et al. (2013) and the ensemble members used for the GNSS combination. The resultant solutions are consistent with the results of Martín-Español et al. (2016b), who separate GIA, ice dynamics, and SMB over a comparable interval. The effect of the range of GIA models on total mass trends is shown in Figure 4.13.

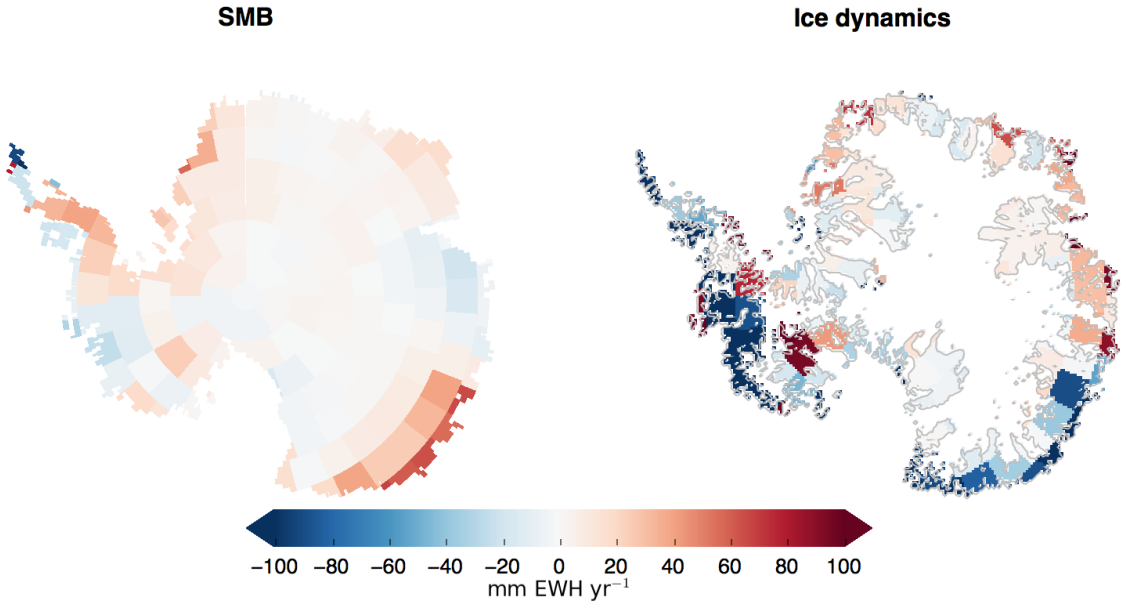

Figure 4.12: Results for source separation of 2002–2017 trends for ice dynamics and surface mass balance using JPL RL05.1 mascons, an ice dynamics mask and covariance, and a surface mass balance mask.

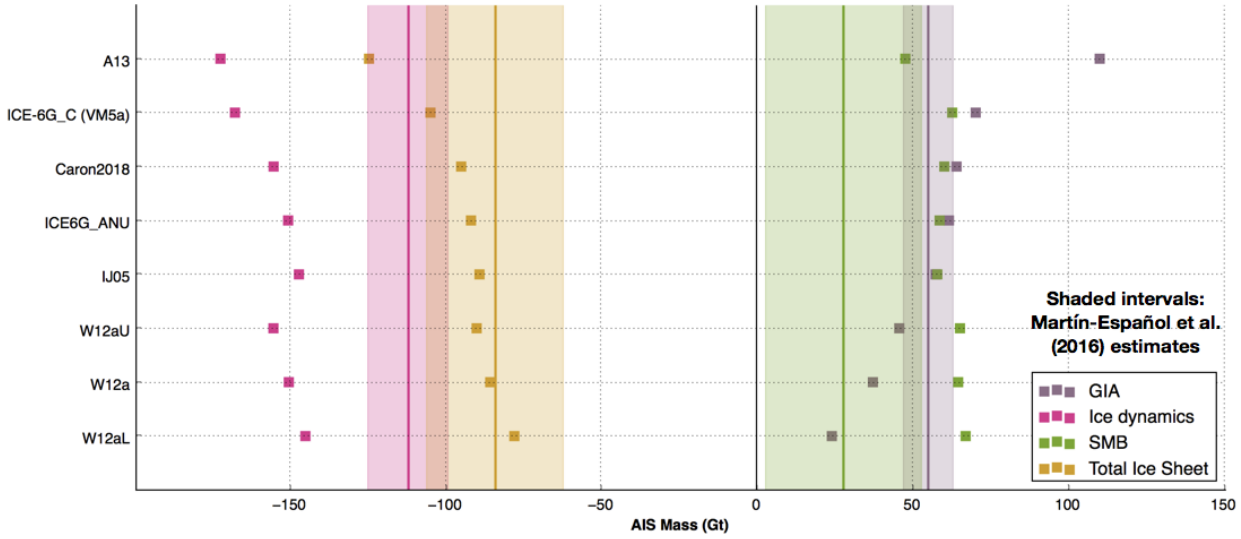

Figure 4.13: Results for source separation of ice dynamics and surface mass balance with an ensemble of GIA background models compared with results for ice dynamics, surface mass balance, and GIA from Martín-Español et al. (2016b).

Chapter 5

Enhancing the Spatial Resolution of Monthly GRACE Solutions with ICESat Trends

The main goal of this endeavor is to combine ICESat, GNSS, and GRACE data to obtain monthly solutions for the distribution of mass in Antarctica. This chapter focuses on combining ICESat trends, monthly GRACE data, and spatial statistics from local models and measurements of local mass change processes to create monthly, high-resolution mass change solutions.

In contrast with the previous chapter, where ICESat elevation rates are computed with an in-house solution, ICESat elevation rates used for the filtering methods in this chapter come from Sasgen et al. (2017). All GRACE data were corrected with the GIA solution of Caron et al. (2018). However, the accompanying covariance of this model was not propagated into the mascon formal errors. The Caron et al. (2018) covariance matrix over Antarctica is dominated by a single spatial pattern that accounts for more than 90% of its variance. The immutable long-wavelength correlations introduced by this covariance destabilized filter solutions, thereby justifying its omission from the solution presented in this chapter.

5.1 Problem Setup

Assuming that the GIA and firn compaction have been corrected, the observation equation to find the variation in average equivalent water height may be written as

$$\begin{bmatrix} \mathbf{y}_{\mathrm{GRACE,i}} - \mathbf{y}_{\mathrm{GRACE,0}} \\ \\ \mathbf{y}_{\mathrm{ICESat,i}} - \mathbf{y}_{\mathrm{ICESat,0}} \end{bmatrix} = \begin{bmatrix} M & M \\ \\ \frac{1}{\rho_{\mathrm{ice}}} L & \frac{1}{\rho_{\mathrm{ice}}} L \end{bmatrix}_i \begin{bmatrix} \mathbf{x}_{\mathrm{SMB,i}} - \mathbf{x}_{\mathrm{SMB,0}} \\ \\ \mathbf{x}_{\mathrm{ice,i}} - \mathbf{x}_{\mathrm{ice,0}} \end{bmatrix}. \tag{5.1}$$

$\mathbf{x}_{\mathrm{ice,i}}$ and $\mathbf{x}_{\mathrm{SMB,i}}$ denote the latent parameter vectors for the cumulative mass contributions from ice dynamics and surface mass balance, respectively. The matrix M performs mascon-averaging of these vectors for direct comparison with GRACE. The matrix L serves to project mass variability fields for comparison with ICESat altimetry.

Monthly solutions for ICESat altimetry are not available at this stage for practical combination with GRACE. Nonetheless, ICESat elevation trend fields still contain spatial information suitable for enhancing low-resolution GRACE data. These trends reflect average mass change within the 2003–2009 span and are still useful as a constraint.

$$\begin{bmatrix} \mathbf{y}_{\mathrm{GRACE,i}} - \mathbf{y}_{\mathrm{GRACE,0}} \\ \\ \dot{\mathbf{y}}_{\mathrm{ICESat,i}} \end{bmatrix} = \begin{bmatrix} M & 0 \\ \\ 0 & \frac{1}{\rho_{\mathrm{ice}}} L \end{bmatrix} \begin{bmatrix} \mathbf{x}_{\mathrm{SMB,i}} - \mathbf{x}_{\mathrm{SMB,0}} + \mathbf{x}_{\mathrm{ice,i}} - \mathbf{x}_{\mathrm{ice,0}} \\ \\ \langle \dot{\mathbf{x}}_{\mathrm{SMB}} \rangle_{2003-2009} + \langle \dot{\mathbf{x}}_{\mathrm{ice}} \rangle_{2003-2009} \end{bmatrix}. \tag{5.2}$$

The above observation equation may be rewritten into two sub-vectors. The lower sub-vector provides an isolated ICESat observation equation, which may be rearranged as

$$\rho_{\mathrm{ice}} \dot{\mathbf{y}}_{\mathrm{ICESat}} = L \left[\langle \dot{\mathbf{x}}_{\mathrm{SMB}} \rangle_{2003-2009} + \langle \dot{\mathbf{x}}_{\mathrm{ice}} \rangle_{2003-2009} \right]. \tag{5.3}$$

The average surface mass balance rate between 2003 and 2009, $\langle \dot{\mathbf{x}}_{\mathrm{SMB}} \rangle$ is provided by RACMO. Since this is an average of six years, or approximately 72 months, of SMB processes, the uncertainty of the estimated field may be estimated by evaluating the sample covariance of RACMO within this time period and dividing this covariance matrix by the number of input months.

The average ice dynamics within this period may therefore be estimated by subtracting the mean SMB field from the ICESat velocity field during this time period.

$$\langle \dot{\mathbf{x}}_{\text{ice}} \rangle_{2003-2009} = \rho_{\text{ice}} L^T \dot{\mathbf{y}}_{\text{ICESat}} - \langle \dot{\mathbf{x}}_{\text{SMB}} \rangle_{2003-2009} \tag{5.4}$$

At each month, ice dynamics may be parameterized as

$$\dot{\mathbf{x}}_{\text{ice,i}} = \langle \dot{\mathbf{x}}_{\text{ice}} \rangle_{2003-2009} + \delta \dot{\mathbf{x}}_{\text{ice,i}} \tag{5.5}$$

The estimation problem is now reduced to simply assimilating GRACE observations with constraints developed from the SMB model and ICESat.

$$\mathbf{y}_{GRACE,i} - \mathbf{y}_{GRACE,i-1} = M(t_i - t_{i-1}) \dot{\mathbf{x}}_i + M(t_i - t_{i-1}) \left[\dot{\mathbf{x}}_{\text{SMB,i}} + \langle \dot{\mathbf{x}}_{\text{ice}} \rangle_{2003-2009} \right] \tag{5.6}$$

.

The variable $\dot{\mathbf{x}}_{\mathbf{i}}$ represents the sum of unmodeled ice dynamics and SMB at each month.

The observation equation may be cumulatively summed over the entire observation span to arrive at

$$\mathbf{y}_{\text{GRACE,i}} - \mathbf{y}_{\text{GRACE,0}} = \sum_{j=0}^{i} M(t_j - t_{j-1}) \left[\dot{\mathbf{x}}_j + \dot{\mathbf{x}}_{\text{SMB,j}} + \langle \dot{\mathbf{x}}_{\text{ice}} \rangle_{2003-2009} \right] \tag{5.7}$$

.

Redefining the cumulative mass change $\sum_{j=0}^{i} (t_j - t_{j-1}) \dot{\mathbf{x}}_j = \mathbf{x}_i$ The final observation equation at each iteration may be set up as

$$\begin{bmatrix} \mathbf{y}_{\text{GRACE,i}} - \mathbf{y}_{\text{GRACE,0}} \end{bmatrix} = \begin{bmatrix} M & 0 \\ 0 & 0 \end{bmatrix} \begin{bmatrix} \mathbf{x}_i \\ \dot{\mathbf{x}}_{\text{SMB,i}} + \langle \mathbf{x}_{\text{ice}} \rangle_{2003-2009} \end{bmatrix} \tag{5.8}$$

with transitions between states expressed by

$$\begin{bmatrix} \mathbf{x_{i+1}} \\ \dot{\mathbf{x}}_{\mathbf{i+1}} \end{bmatrix} = \begin{bmatrix} I & t_{i+1} - t_i \\ 0 & 0 \end{bmatrix} \begin{bmatrix} \mathbf{x}_i \\ \dot{\mathbf{x}}_{\text{SMB,i}} + \langle \dot{\mathbf{x}}_{\text{ice}} \rangle_{2003-2009} \end{bmatrix} + \begin{bmatrix} 0 \\ \dot{\mathbf{x}}_{\text{SMB,i+1}} + \langle \dot{\mathbf{x}}_{\text{ice}} \rangle_{2003-2009} \end{bmatrix} \tag{5.9}$$

The state derivative term in the parameter vector is not estimated, but is informed by SMB and ice dynamics priors at all steps.

The covariance of the average ice dynamics within this time period is the sum of the covariance of ICESat errors, SMB, and the scaled firn elevation.

With ICESat and RACMO used in the creation of priors, the filter at every step becomes

$$\begin{bmatrix} \mathbf{x}_{i|i} \\ \dot{\mathbf{x}}_{i|i} \end{bmatrix} = K \left[\mathbf{y}_{\mathrm{GRACE,i}} - \mathbf{y}_{\mathrm{GRACE,0}} - H \begin{bmatrix} \mathbf{x}_{i|i-1} \\ \dot{\mathbf{x}}_{i|i-1} \end{bmatrix} \right] + \begin{bmatrix} \mathbf{x}_{i|i-1} \\ \dot{\mathbf{x}}_{i|i-1} \end{bmatrix} \tag{5.10}$$

The subscript notation $i|j$ may be read as "pertaining to the state i given prior information at state j". The matrix H is the observation operator,

$$H = \begin{bmatrix} M & 0 \\ 0 & 0 \end{bmatrix} \tag{5.11}$$

,

which contains the mascon-averaging operator M.

The matrix K is a minimum mean-squared error estimator, the Kalman gain. This matrix contains the optimal modification vectors of the solution associated with unit errors in the observations. K is conventionally estimated from the covariance of the observation errors and the cross-covariance of the observation errors and state errors.

$$K = C_{XY} C_{YY}^{-1}, \tag{5.12}$$

where X and Y denote latent parameters and observations, respectively. If the covariance provides enough information and C_{YY} is positive definite, then parameters may be adjusted by observations even if the number of unknown parameters exceeds number of observations. If the parameter covariance matrix, $P_{i|i-1}$ is known, the covariance of the observations R_i is also known, and a linear operator H exists to relate observations and parameters, then

$$C_{XY} = P_{i|i-1} H^T \tag{5.13}$$

and

$$C_{YY} = HP_{i|i-1}H^T + R_i \tag{5.14}$$

.

The Kalman gain is therefore

$$K = P_{i|i-1}H^T(HP_{i|i-1}H^T + R_i)^{-1}. \tag{5.15}$$

Solutions generated from the Kalman filter may be propagated forward in time to the next step. Covariances may also be adjusted to include information from the current iteration using the Joseph formulation,

$$P_{i|i} = (I - KH)P_{i|i-1}(I - KH)^T + KRK^T \tag{5.16}$$

which can be simplified to

$$P_{i|i} = (I - KH)P_{i|i-1} \tag{5.17}$$

.

The Kalman filter is simple to describe and conceptually straightforward to implement. Because the observation operations in this work are strictly linear, the assumptions under which the filter is derived are valid. The challenge of constructing the Kalman filter lies in establishing the covariance of the parameters.

Since the subsampled land components of CRI-filtered mascons have highly variable areas and the filtering setup requires predicting mascon equivalent water heights, smaller mascons may have unwarranted leverage on the solution. To remedy this effect, a weighting matrix is applied to the numerator and denominator of the Kalman gain. The weighting matrix W has diagonal elements equal to the square of the areas of the corresponding mascons. This modification implicitly changes the observation equations so the figure of merit is the variance of the residual mass of each mascon rather than its mass flux. The Kalman gain takes the form:

$$K = P_{i|i-1}H^T W(WHP_{i|i-1}H^T + WR_i)^{-1}. \tag{5.18}$$

5.2 Computational Considerations

The Kalman filter is well-suited for monthly solutions. The computation of the Kalman gain is straightforward when the number of observations is small relative to the number of parameters because rank the effective rank of this matrix is limited by the number of data points. The scaling of the Kalman gain computation time is quadratic with the number of parameters, but linear with the number of data points. The solution presented here exists on a 27 km grid with 17,880 elements mapped to the JPL land mask. At every iteration, GRACE provides a vector of 148 mascons that represent averages of these grid cells.

The covariance update step in the Kalman filter is the most computationally intensive part of the filter. This step involves the multiplication of two $n \times n$ matrices, an operation with a computational complexity of $O(n^3)$, where n is the number of data points. One alternative to the conventional Kalman filter keeps the filter entirely in terms of the data-parameter covariance matrix PH^T. This approach keeps the computational complexity of the filter to $O(m^2 n)$, where m is the number of parameters. The covariance update step is approximated with a Taylor expansion. This approach was briefly considered and implemented, but found found to be unnecessary for the work subsequently presented in this chapter.

The need to reduce the size of the parameter vector prompted exploration of various mesh optimization methods to capture small-scale variability in select parts of Antarctica while relegating quiet inland variation to low-resolution. Foremost among these methods was the construction of variance quadtrees (Minasny et al., 2007) based on various geophysical fields that reflect Antarctic mass variation, such as topography. The variance quadtree algorithm divides a field into quadrilateral zones with variances less than or equal to a threshold value. Each quadtree element may be considered to have equal variance and therefore equal weight when being assimilated into a solution. The implementation of this algorithm enables its use for future investigations.

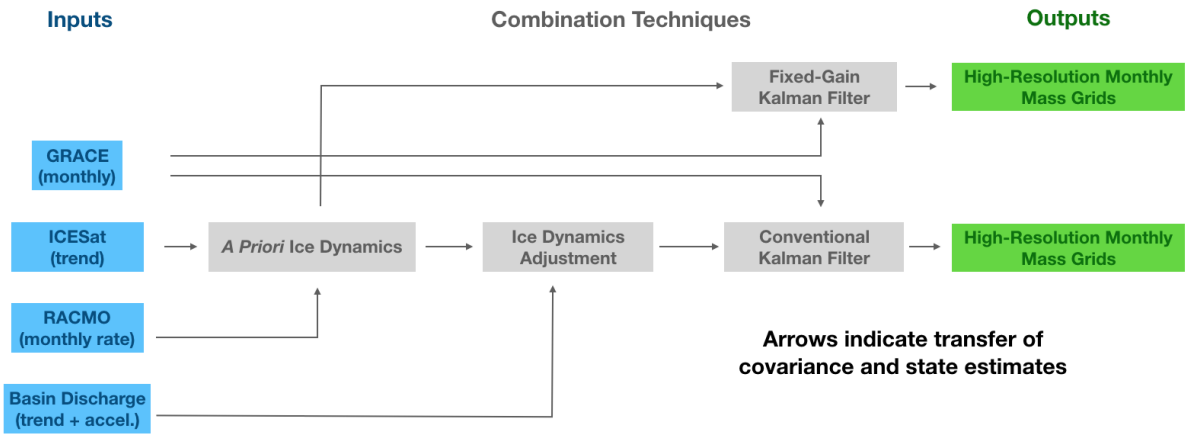

Figure 5.1: Summary of information flow for monthly combination techniques

While mesh optimization provided interesting avenues for parameterization of Antarctic mass, the computational complexity problem was ultimately solved by downsampling the matrix by a factor of four, reducing the number of elements required to describe Antarctic land mass from 17,880 to 1,105. The parameter vector is a lattice of 108 km elements, each representing up to 16 27-km grid elements. This vector is projected onto the solution grid with nearest-neighbor interpolation.

The flow of information in these solution methods is illustrated by Figure 5.1.

5.2.1 Priors and Covariance Matrix Construction

The trick used to obtain monthly solutions involves using ice dynamics to establish a prior. A number of parameterizations of the *a priori* covariance of ice dynamics were explored.

The final covariance model for ice dynamics is generated using the following procedure:

Amid other sources of elevation change, ICESat trends contain a measurement of the average ice dynamics between 2003 and 2009. Using the Ligtenberg et al. (2011) firn model and RACMO2.3, it is possible to remove the effect of firn compaction and the contribution of surface mass balance from this dataset. The uplift signal of GIA is also present in this model and removable. The altimetry field also contains elastic loading signals from Antarctic mass variation.

The initial estimate for the ice mass trend field is convolved with high-resolution Green's functions to compute vertical crustal deformation from elastic loading. This crustal deformation field is subtracted from the altimetry data. The loading-corrected altimetry is then used to recompute the *a priori* ice mass variation signal. This iteration is not repeated.

The ice mass rate is unobserved south of 86° S. Grid cells south of this latitude are imputed with the median ice mass value in an annulus between 85° S and 86° S.

The prior mass rate covariance matrix becomes:

$$P = \rho_{\text{ice}} \left[P_{\dot{h}} + P_{\text{firn}} \right] + P_{\text{SMB}} + P_{\text{ice}} k \tag{5.19}$$

The factor k scales the covariance so it represents the variability of the field at monthly time scales rather than the average over the ICESat observation time period. k is set to 72 in this work.

ICESat trend uncertainties provided by REGINA are clipped between 0 and 1 m yr^{-1}. They are subsequently median-filtered with a to further remove outliers. The median filter has a bidirectional window size of 5 adjacent grid points (135 km full-width). The median filter also introduces spatial correlations. These trend errors are multiplied by the ρ_{ice} (917 kg m^{-3}).

P_{ice} is estimated from the

$$P_{ij,\text{ice}} = \left[\rho_{\text{ice}}^2 |\dot{h}_i||\dot{h}_j| + \sigma_0^2 \right] e^{-\frac{1}{2}\frac{r_{ij}^2}{s^2}} \tag{5.20}$$

The nugget σ_0^2 is set to 10 mm EWH^2, a value consistent with the noise floor of the altimetry. The purpose of this step is to ensure that zero-crossings in the field are allowed to vary. The sill term also enables variation within the unobserved part of Antarctica south of 86° S, which is visible to GRACE. The range scale parameter s was set to 250 km, consistent with semivariograms of the ICESat elevation trend field. The resultant covariance matrix is shown in Figure 5.2.

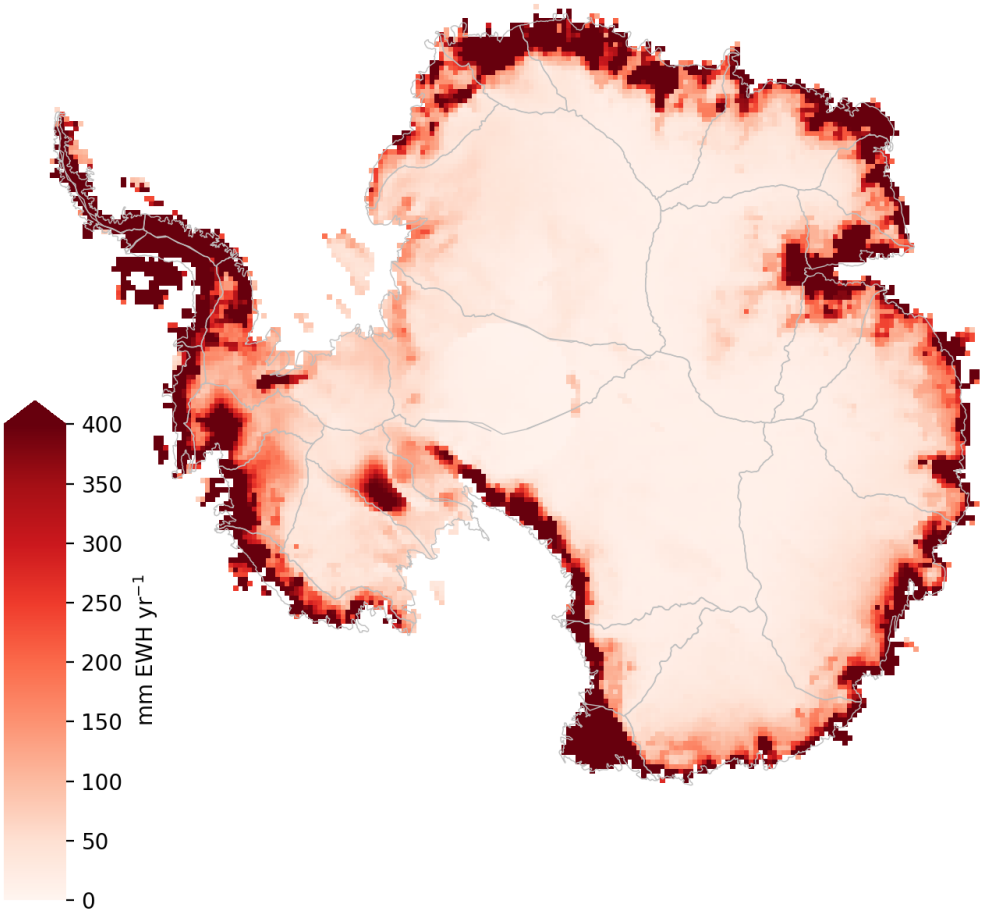

Figure 5.2: Diagonal elements (standard deviations) of *a priori* covariance matrix for ice dynamics derived from ICESat 2003–2009 elevation trends and average surface mass balance. These constraints demonstrate and impose high-magnitude, short-wavelength variability near the Antarctic coasts and low-magnitude, long-wavelength variability inland.

5.2.2 Validation with GNSS

High-resolution solutions for mass variation in Antarctica may be considered valid if they predict signals in independent data that others models do not. Our filter assimilates ICESat trends and GRACE data. The remaining geodetic data in Antarctica are GNSS position time series, which contain elastic-loading displacement signals from Antarctic mass variations. These data were deliberately set aside for validation.

Improvement in spatial resolution has multiple effects on crustal displacement time series. In the vertical direction, increased concentration of mass variation changes the near-field amplitude of elastic displacements. The horizontal components of crustal motion contain directional information and are therefore sensitive to the location of a loading source. While the vertical signal introduced by elastic loading depends only on distance, the horizontal components of a GNSS position time series positioned near a loading source will be markedly different from the time series observed if the loading source's position were changed, but its distance to the observation site remained the same. Because of the geometry of satellite observations, GNSS observations are also more precise in the horizontal plane than the vertical axis. However, while horizontal measurements are less noisy, the effect of elastic loading in the horizontal direction is also approximately half that of the vertical effect. (Wahr et al., 2013)

GNSS motion time series contain linear-trend signals that are not caused by crustal loading, such as plate tectonics and GIA. Horizontal GNSS position time series contain valuable data on crustal deformation due to elastic loading. The geometry of GNSS observations also make these observations less noisy and underconstrained Unfortunately, long-period signals due to plate tectonics and GIA are difficult to model. While robust approximations (Purcell et al., 2011) relating the vertical component of GIA-induced displacement to corresponding change in gravity exist, relations for the horizontal component of GIA are indeterminate and highly model-dependent Sabadini and Vermeersen (2004). Modeling long-period signals, such as GIA, may be avoided by detrending both the set of elastic loading predictions from the output model and the horizontal motion data. As

detrending is a linear operation, a detrending operator may be added to the observation operator during the assimilation process to make the horizontal motion data comparable with only non-trend signals.

While horizontal trend signals are avoided, vertical trends predicted with both the JPL RL05.1M mascons and these solution methods are compared. This comparison is sensitive to the choice of GIA model.

The comparison is performed by computing elastic loading in the east, north, and vertical directions with both the JPL RL05.1M mascons and the mass change solutions from our filters. Elastic-loading displacement from the atmosphere and oceans were removed using the GAC component of AOD1B RL05. Because of the high intrinsic resolution of the Kalman filter results, we computed loading using near-exact radial Green's functions obtained from (Petrov, 2004)[1] . The loading signals from the mascons were computed by projecting the land-components of the Antarctic CRI-filtered mascons to onto the same grid as our candidate solutions and applying the same convolution with high-resolution Green's functions.

5.3 Fixed-gain Kalman Filter

The feasibility of monthly solutions was initially explored with a case testing the following idea: Could mascon trends be processed with a filter with ICESat-based covariance to obtain a high-resolution mass trend field? In the setup discussed at the beginning of the chapter, the Kalman gain is defined in terms of the observation-parameter covariance and data-data covariance. The covariance for ice dynamics obtained earlier in this chapter may be used as an input to compute both covariance matrices.

The observation equation for this setup is

$$\dot{\mathbf{y}}_{\mathrm{GRACE}} = M\dot{\mathbf{m}}. \tag{5.21}$$

$\dot{\mathbf{y}}_{\mathrm{GRACE}}$ is a vector of best-fit rates of change in mascon equivalent water height between 2003

[1] http://vlbi.gsfc.nasa.gov/aplo/

and 2009; $\dot{\mathbf{m}}$ is the corresponding rate of change at higher resolution. The filter takes the form:

$$\dot{\mathbf{m}} = K[\dot{\mathbf{y}}_{\mathrm{GRACE}} - M\dot{\mathbf{m}}_{\dot{h}}] + \dot{\mathbf{m}}_{\dot{h}}. \tag{5.22}$$

$\dot{\mathbf{m}}_{\dot{h}}$ is the sum of the *a priori* ice dynamics estimate and the 2003–2009 average SMB from RACMO. The subscript $\dot{h}$ indicates the origins of this prior in satellite altimetry. The Kalman gain K, as previously established depends on the observation operator M and the covariance of the ice sheet mass trend field within this span.

$$K = PM^T W \left[W(MPM^T + R)\right]^{-1} \tag{5.23}$$

The observations errors R are estimated from the errors in the GRACE trend between 2003 and 2009, or within the ICESat observation span. That is, $R = [r_{jj}^2]$ and

$$r_{jj}^2 = \frac{1}{n-2} \frac{\sum_{k=1}^{n} \sigma_{kj}^2}{\sum_{k=1}^{n} (t_k - \bar{t})^2}. \tag{5.24}$$

.

σ_{kj} is mascon j's formal error at time t_k. The constant $\bar{t}$ is the mean of the n months that comprise the inputs to the GRACE trend calculation. The GIA covariance P_{GIA} from Caron et al. (2018) is not added to the GRACE uncertainty. W is a diagonal matrix with elements equal to the square of the area of the corresponding mascon. The addition of this term serves to weight the observations by the areas of the mascons, ensuring that noise in smaller mascons does not have excess influence over the solution.

The covariance matrix P is set to P_{ice} as established in the previous section. The results of this combination are shown in Figure 5.3.

The success of this filter naturally raises a question of whether it can be applied to individual GRACE months without modifying the Kalman gain. To explore this, the following modifications were made:

The basic observation equation is

$$\mathbf{y}_i = M\mathbf{m}_i, \tag{5.25}$$

where $\mathbf{y}_i$ is the vector of predicted equivalent water heights for the 148 land mascons at the time t_i. The filter seeks to minimize the variance of $\mathbf{y}_{i,\text{obs}} - \mathbf{y}_i$, where $\mathbf{y}_{i,\text{obs}}$ is the vector of mascons in the GRACE dataset at time t_i. The operator M performs mascon averaging of grid cells and serves as the observation operator for this demonstration.

The filter takes the form

$$\mathbf{m}_i = K[\mathbf{y}_{i,\text{obs}} - M\dot{\mathbf{m}}_{\dot{h}}(t_i - t_0)] + \dot{\mathbf{m}}_{\dot{h}}(t_i - t_0). \tag{5.26}$$

$$K = PM^T W\left[W(MPM^T + R)\right]^{-1} \tag{5.27}$$

The matrix P and the *a priori* estimate of the mass loss field are both estimated from the the ICESat trend grid over the 2003–2009 observation span.

The continental mass variation solution time series for the 2002–2017 interval is shown in Figure 5.4. Basin-by-basin mass evolution time series are shown in Figure 5.6. These changes are integrated according to defined regions of the Antarctic Ice Sheet to obtain the time series in Figure 5.5. Finally, the elastic loading effects of this model on Antarctic GNSS sites is shown in Figure 5.7.

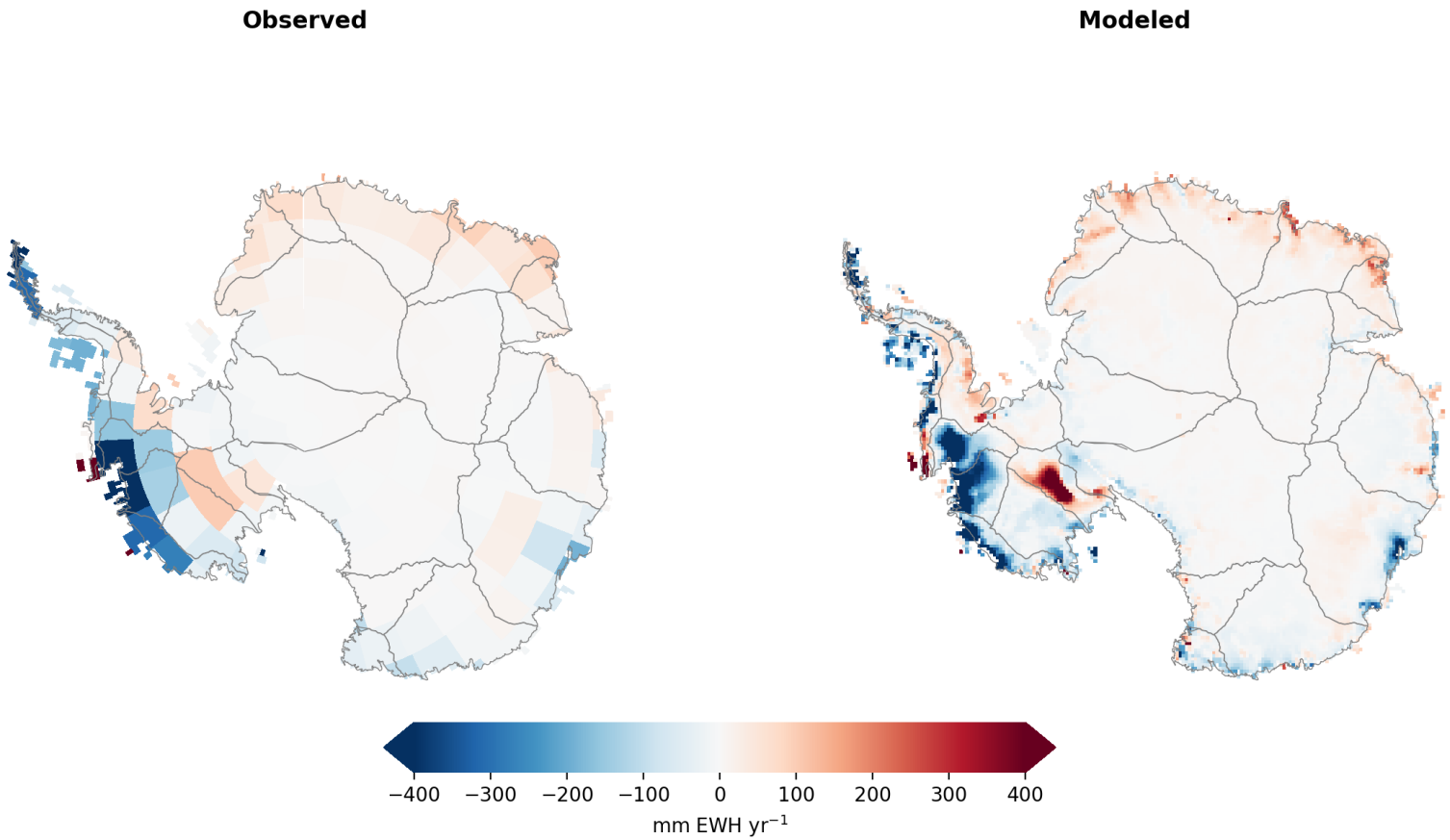

Figure 5.3: Input mascon trends over 2002–2017 interval and enhanced trends for the same time period obtained from the fixed-gain Kalman filter

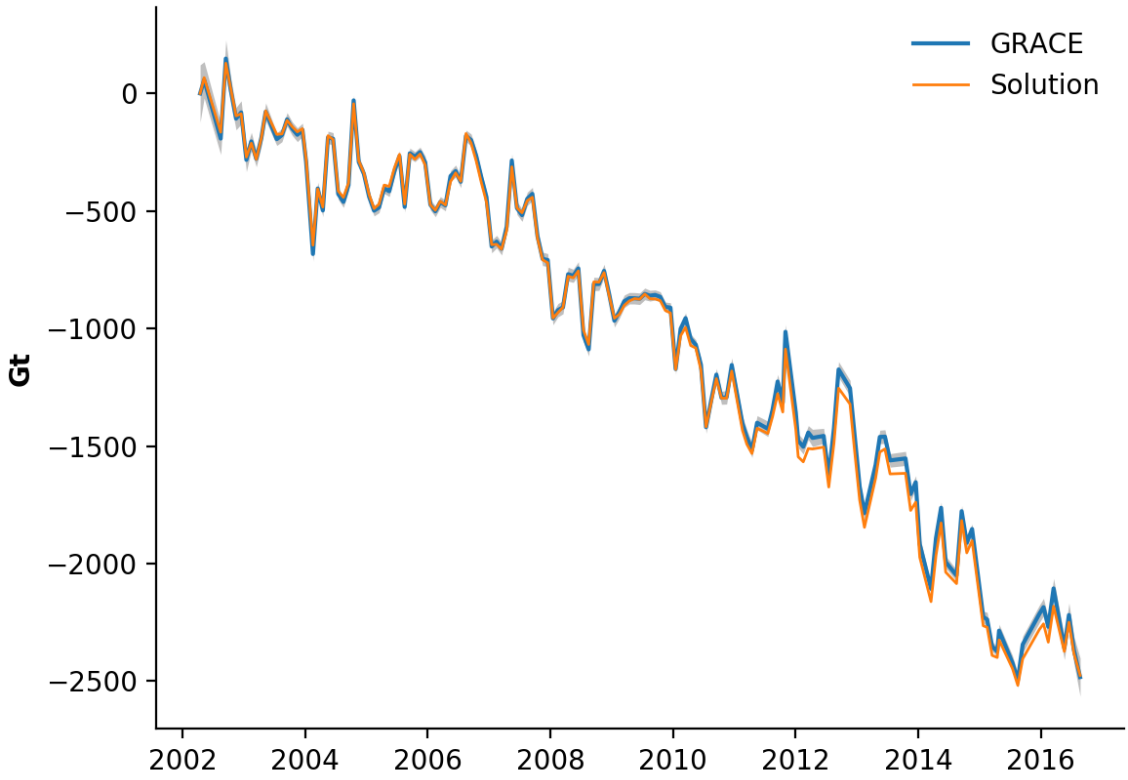

Figure 5.4: Mass change integrated over the entire Antarctic ice sheet from the fixed-gain Kalman filter compared with its input GRACE data and corresponding 1-σ errors

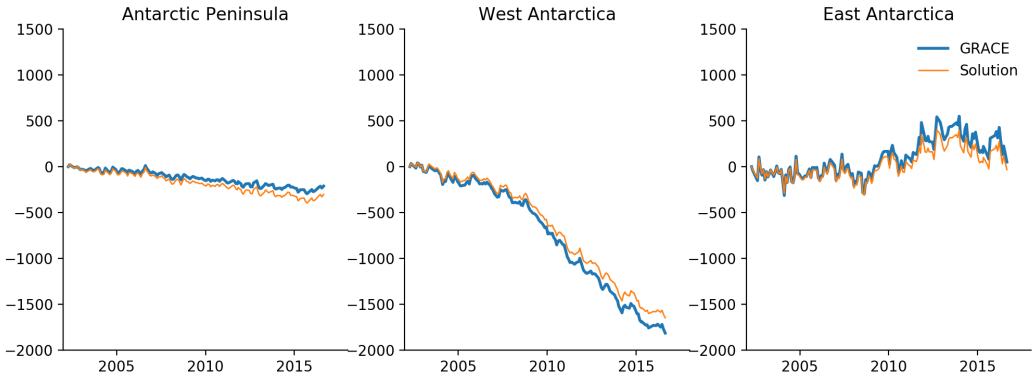

Figure 5.5: Mass change (Gt) from the fixed-gain Kalman filter in Gt integrated over East Antarctica, West Antarctica, the Antarctic Peninsula compared with corresponding GRACE data

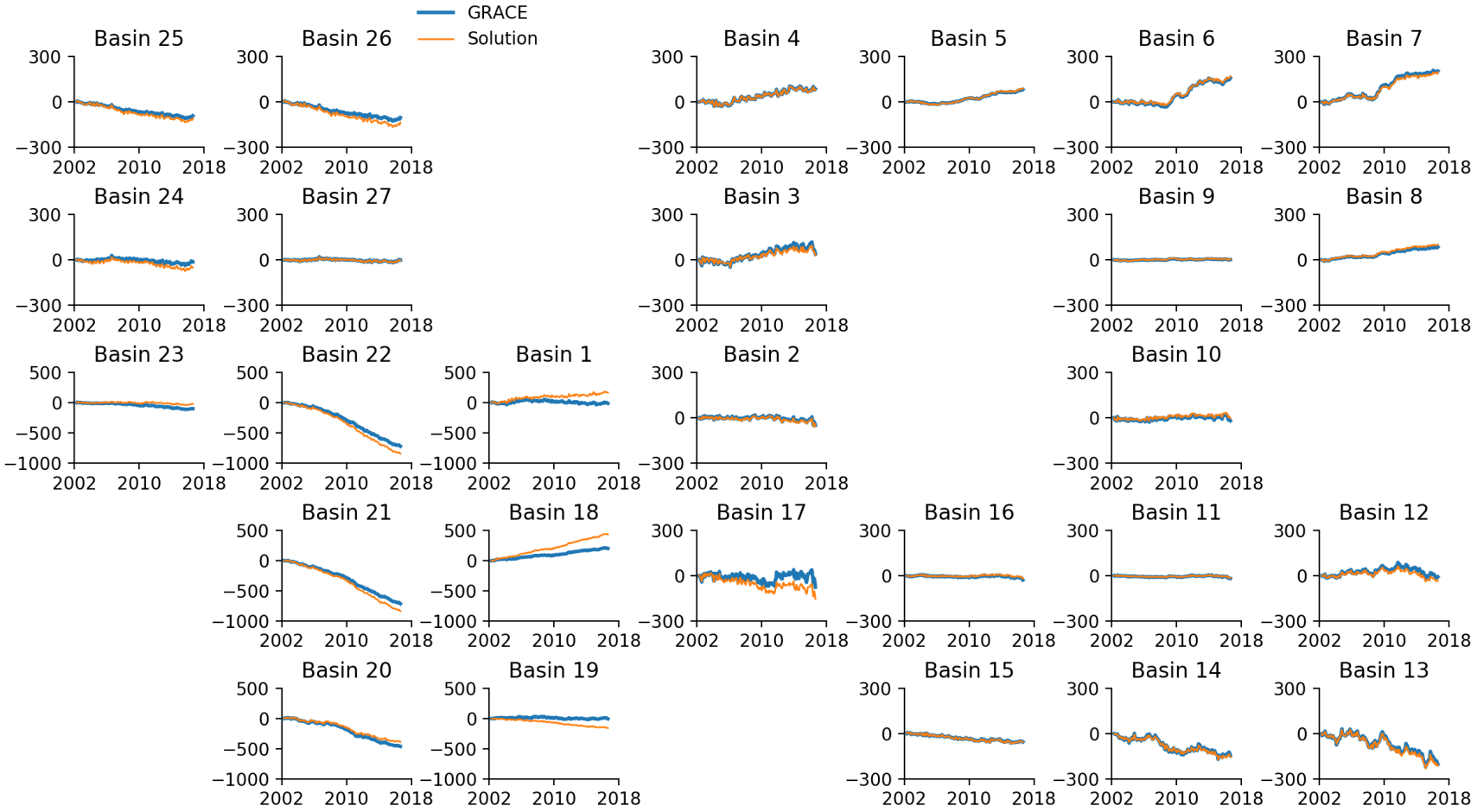

Figure 5.6: Basin-by-basin time series of mass change (Gt) obtained from the fixed-gain Kalman filter and compared with GRACE

5.4 Adjustment of Ice Dynamics

Ice dynamics processes vary slowly over time. For the purposes of this study, ice dynamics may be modeled over the 2002–2017 interval as a static trend with a constant acceleration. Direct measurements of total basin-scale ice dynamics are available from Gardner et al. (2018), who measured the volumetric discharge of ice from outlet glaciers for each of Antarctica's 27 drainage basins, as defined by Zwally et al. (2012). The basin boundaries are illustrated in Figure 5.8. The measurements were performed by measuring horizontal displacements at outlet glaciers (flux gates) for each basin with satellite imagery. Discharge rates are available from 2008 and 2015 and may be differenced to compute discharge acceleration. The time-integrated ice dynamics signal within a basin may be modeled as a quadratic function of time with these basins as inputs.

Assuming the ice dynamics field developed from ICESat and RACMO earlier in this chapter is accurate, then its spatial integrals within each basin should agree with the Gardner et al. (2018) estimates. Using the *a priori* covariance of the ice dynamics, these basin-scale estimates may then be optimally adjusted to fit the measured time-dependent basin discharge. Such a fit has two effects. First, it ensures that the ice dynamics prior matches both the spatial patterns implied by ICESat and RACMO; and the independent magnitudes of basin-level integral measurements. Second, it introduces time-dependence in the form of constant acceleration to the ice dynamics prior.

The fit is performed with a Kalman filter as before. The filter is evaluated sequentially, but error estimates are not propagated in time.

For each month, the observation equation is

$$\dot{\mathbf{y}}_{\mathrm{basin,i}} = B\dot{\mathbf{m}}_{\mathrm{ice,i}}. \tag{5.28}$$

The operator B integrates grid mass fluxes over each drainage basin for comparison with the discharge estimates. The adjustment to the ice dynamics field at each month is

$$\dot{\mathbf{m}}_{\mathrm{i,ice,posterior}} = K(\dot{\mathbf{y}}_{\mathrm{basin,i}} - B\dot{\mathbf{m}}_{\mathrm{i,ice,prior}}) + \dot{\mathbf{m}}_{\mathrm{i,ice,prior}}. \tag{5.29}$$

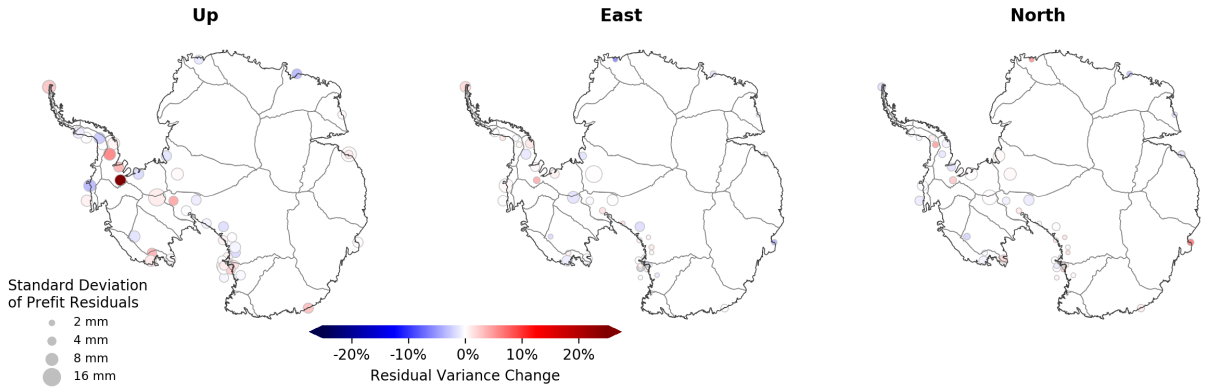

Figure 5.7: Change in variance of the detrended residual GNSS position time series relative to results obtained by computing elastic crustal deformation with the JPL RL05.1M mascon solutions after removing elastic crustal deformation predictions from the fixed-gain Kalman filter.

The Kalman gain K is defined as:

$$K = P_{\text{ice,prior}} B^T (B P_{\text{ice,prior}} B^T + R)^{-1}, \tag{5.30}$$

where $R = r_i^2 j \delta_{jk}$, the measurement errors for the Gardner et al. (2018) basin discharge error estimates. No propagation of the acceleration errors in time is performed to obtain this matrix. This keeps the Kalman gain constant and also saves memory by requiring the computation of a single updated covariance matrix.

$$P_{\text{ice,posterior}} = (I - KB) P_{\text{ice,prior}} \tag{5.31}$$

The parallel nature of this solution makes it functionally equivalent to simply reducing the ice dynamics field to a trend and acceleration, but the actual implementation instead evaluates ice dynamics independently at each month. This adjustment is illustrated in Figure **??**. The output of this procedure may be fed forward to other solutions.

The adjusted solution may also be added to RACMO SMB fields and integrated through time to create a solution independent of GRACE. The 2002–2017 trend is shown in Figure 5.10. The total AIS mass time series is given in Figure 5.11. Basin-by-basin mass evolution time series are shown in Figure 5.13. These changes are integrated according to defined regions of the Antarctic Ice Sheet to obtain the time series in Figure 5.12. Finally, the elastic loading effects of this model on Antarctic GNSS sites is shown in Figure 5.14.

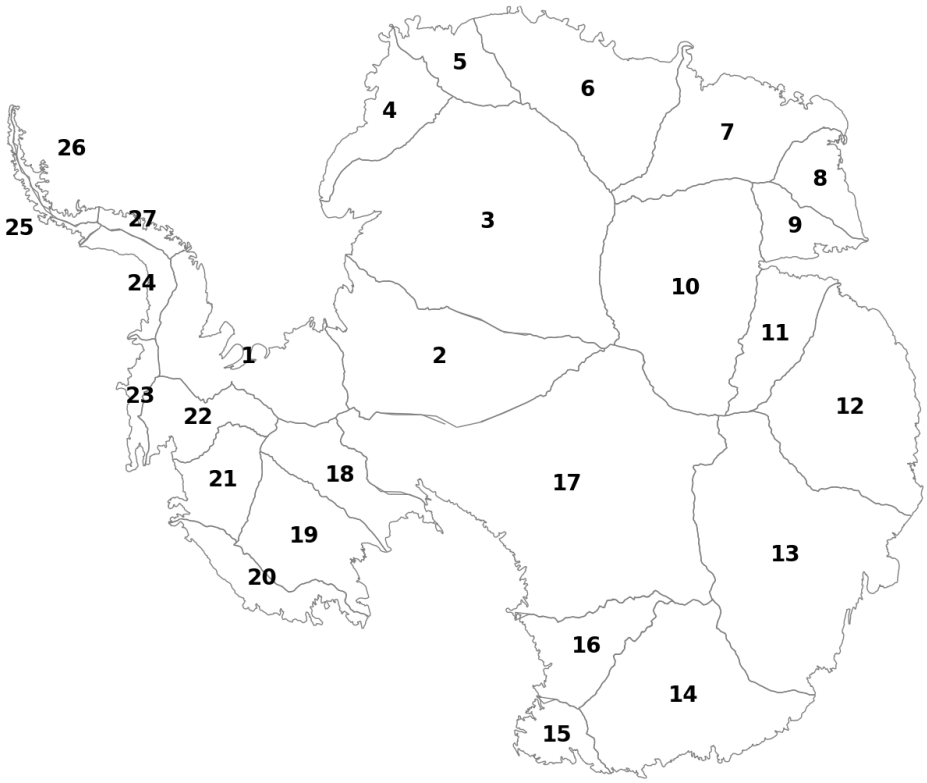

Figure 5.8: Boundaries and indices of Zwally et al. (2012) Antarctic ice sheet drainage basins

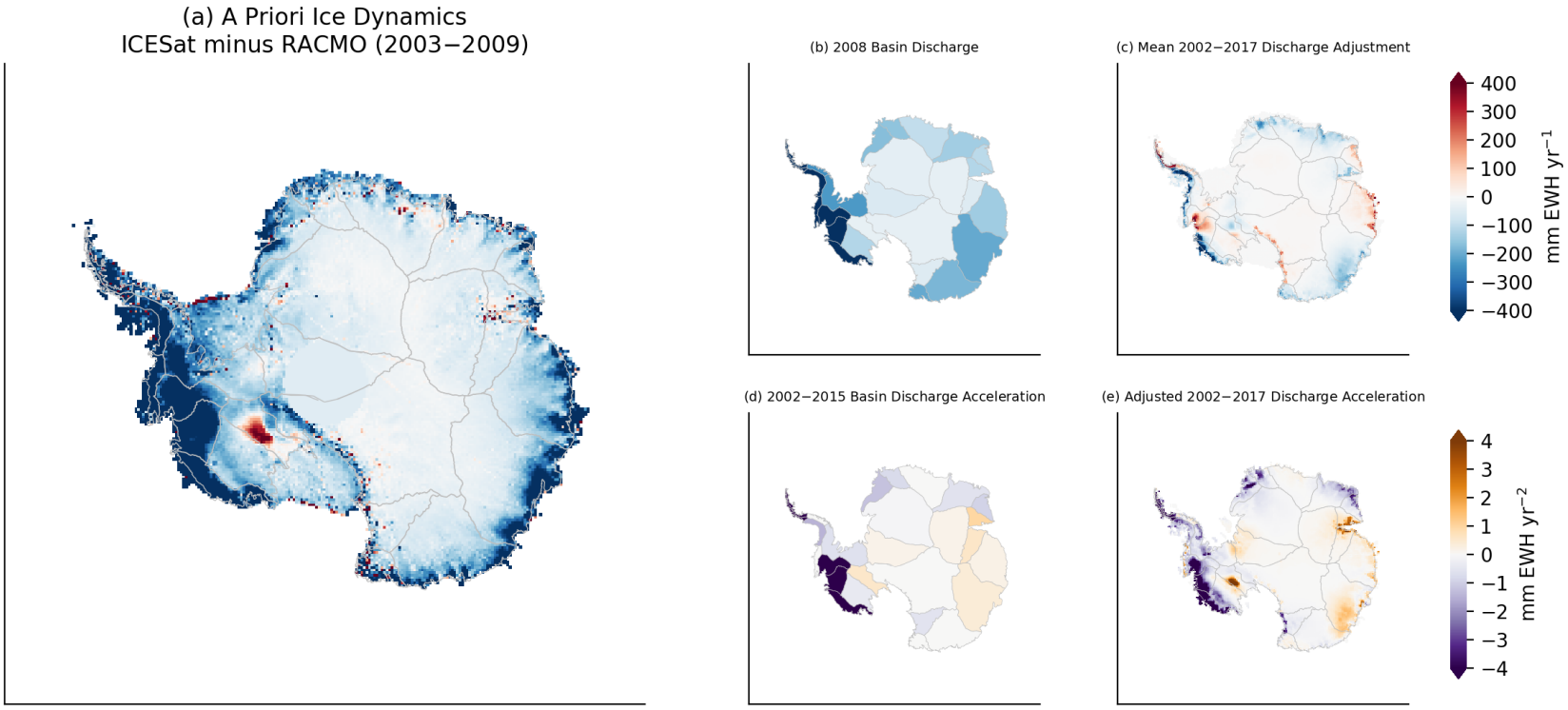

Figure 5.9: Inputs and results for adjustment of ice dynamics fields with basin-level constraints.
a. Prior solution for ice dynamics obtained from 2003–2009 ICESat trends and average surface mass balance from the same period
b. Basin discharge estimates from Gardner et al. (2018)
c. Mean of optimal adjustments to ice dynamics rates between 2002 and 2017 from prior ice dynamics estimates and constraints from Gardner et al. (2018)
d. Basin discharge acceleration estimates from Gardner et al. (2018)
e. Optimal adjustments to ice dynamics accelerations between 2002 and 2017 from prior ice dynamics estimates and constraints from Gardner et al. (2018)

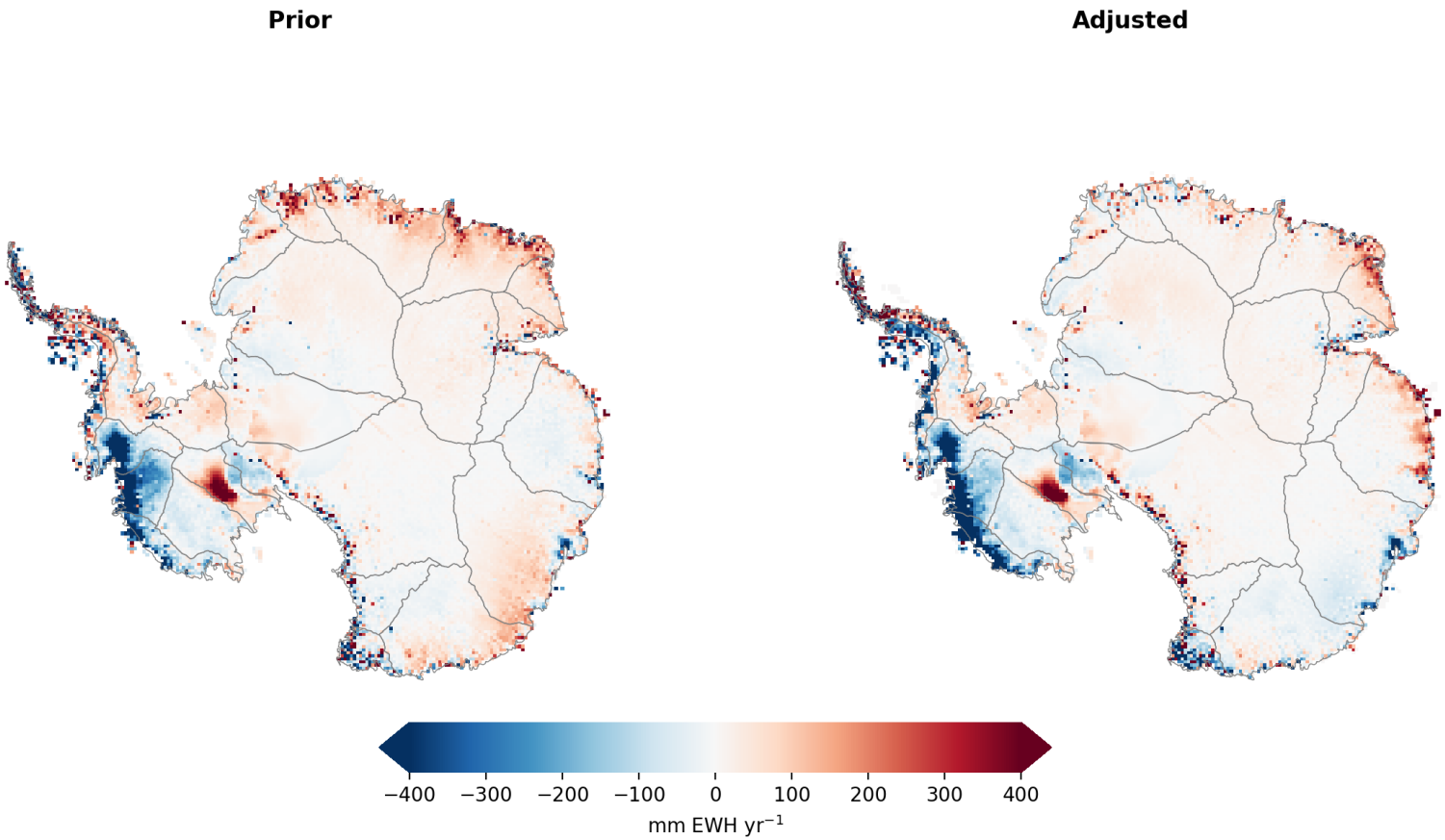

Figure 5.10: Input mascon trends over 2002–2017 interval and enhanced trends for the same time period obtained from the adjusted ice dynamics solution.

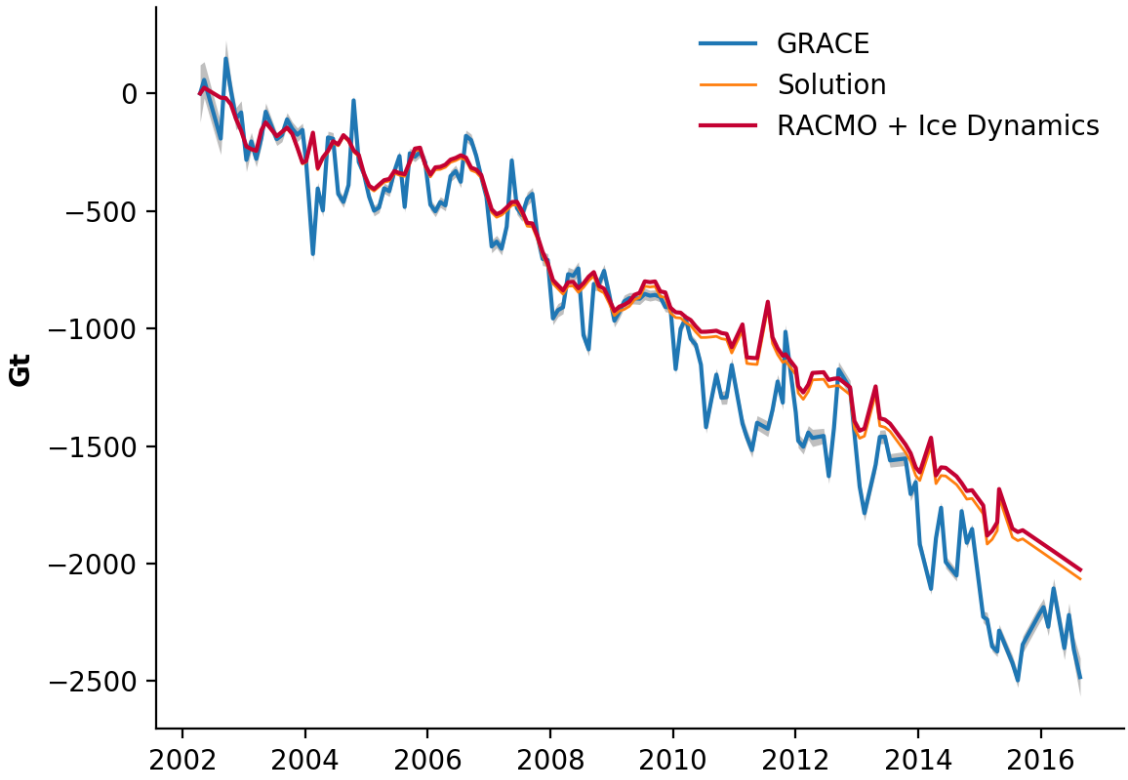

Figure 5.11: Mass change integrated over the entire Antarctic ice sheet from the adjusted ice dynamics solution compared with its input GRACE data and corresponding 1-σ errors

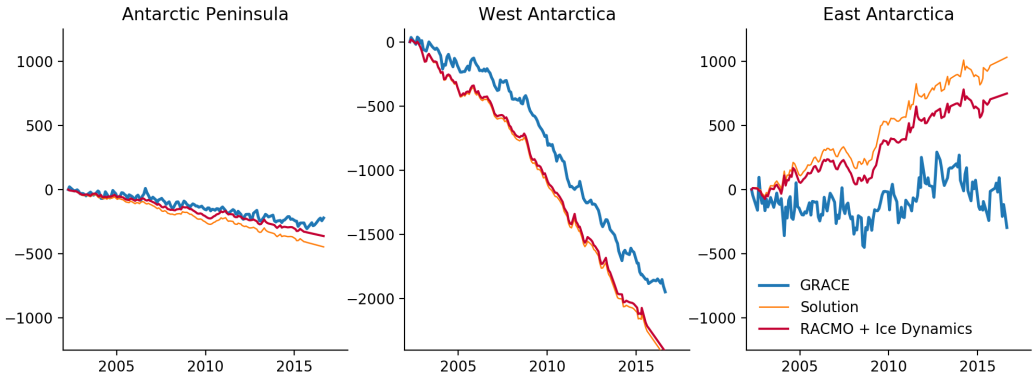

Figure 5.12: Mass change (Gt) from the adjusted ice dynamics solution in Gt integrated over East Antarctica, West Antarctica, the Antarctic Peninsula compared with corresponding GRACE data

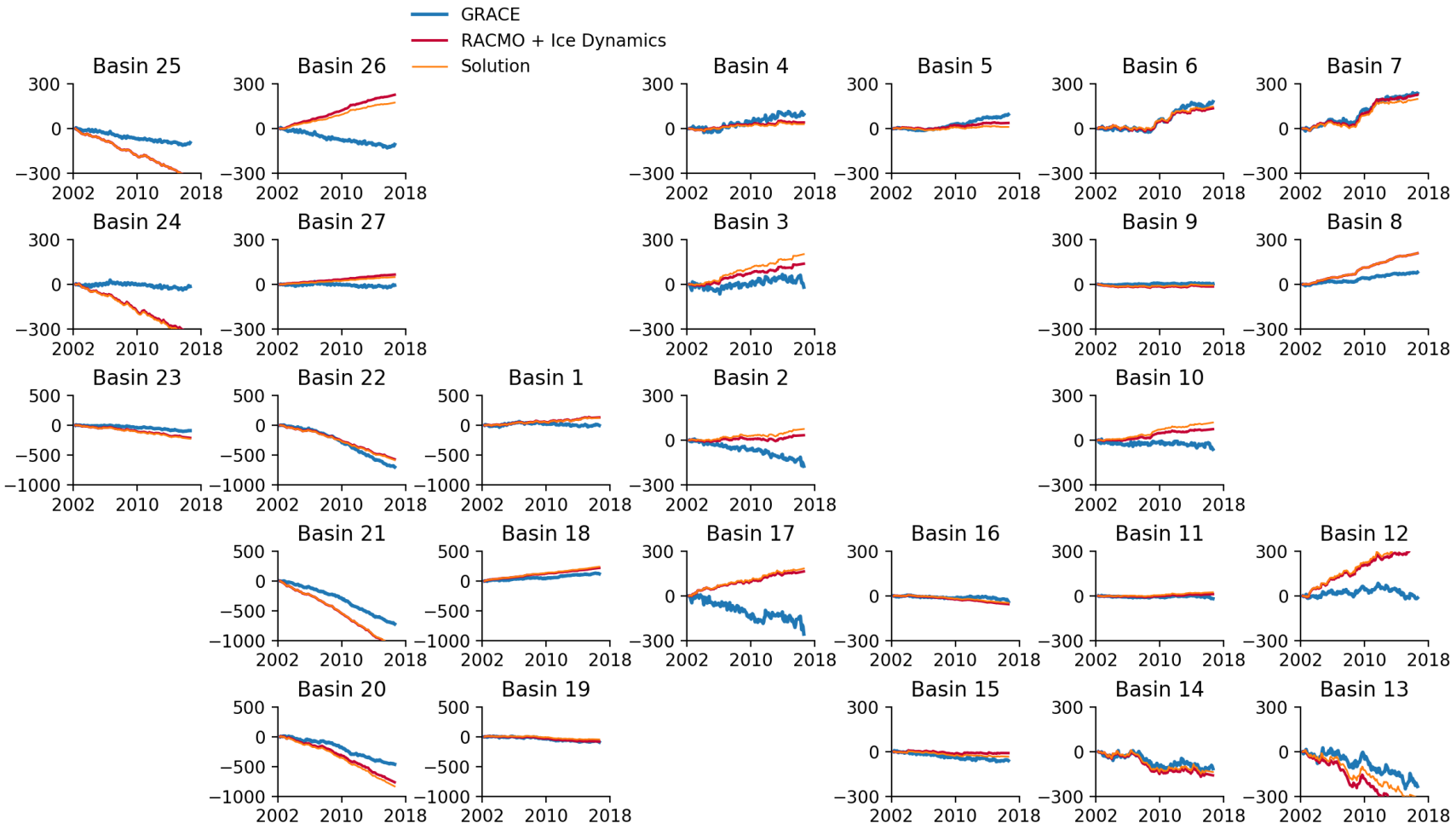

Figure 5.13: Basin-by-basin time series of mass change (Gt) obtained from the adjusted ice dynamics solution and compared with GRACE

5.5 One-Dimensional Kalman Filter

A one-dimensional Kalman filter was devised to verify the conceptual integrity of the Kalman filters in this chapter. This filter adjusts only the cumulative mass change and mass change rate of Antarctica according the the total mass estimated by GRACE.

The total mass change of the Antarctic ice sheet at time t_i relative to t_0 is given by m_i. The rate of mass change, given by the sum of ice dynamics and surface mass balance at time t_i is $\dot{m}_i$. The cumulative mass change and instantaneous rate of mass change may be assembled into a state vector:

$$\mathbf{x}_i = \begin{bmatrix} m_i \\ \dot{m}_i \end{bmatrix}. \tag{5.32}$$

The surface mass balance model used here has output available no later than December 2015, whereas the GRACE data runs to August 2016. SMB for months outside of the boundary are imputed with the average SMB integrated over the entire continent for the 2002–2016 period. For the purposes of this filter, the instantaneous mass change is integrated forward in time linearly as a function of $\Delta t = t_i - t_{i-1}$.

$$\mathbf{x}_{i|i-1} = \begin{bmatrix} m_{i|i-1} \\ \dot{m}_i \end{bmatrix} = F_i \mathbf{x}_{i-1|i-1} + \begin{bmatrix} 0 \\ \dot{m}_i \end{bmatrix}. \tag{5.33}$$

The state transition matrix F_i is designed such that information about the rate of mass change is not preserved between iterations. Instead, the instantaneous rate of mass change is obtained from external models.

$$F_i = \begin{bmatrix} 1 & \Delta t \\ 0 & 0 \end{bmatrix}. \tag{5.34}$$

The state also has an associated covariance. The covariance P_0 is initialized such that all terms in the 2x2 matrix are zero. The covariance for the current iteration is propagated forward in time from the previous iteration to the current iteration as follows.

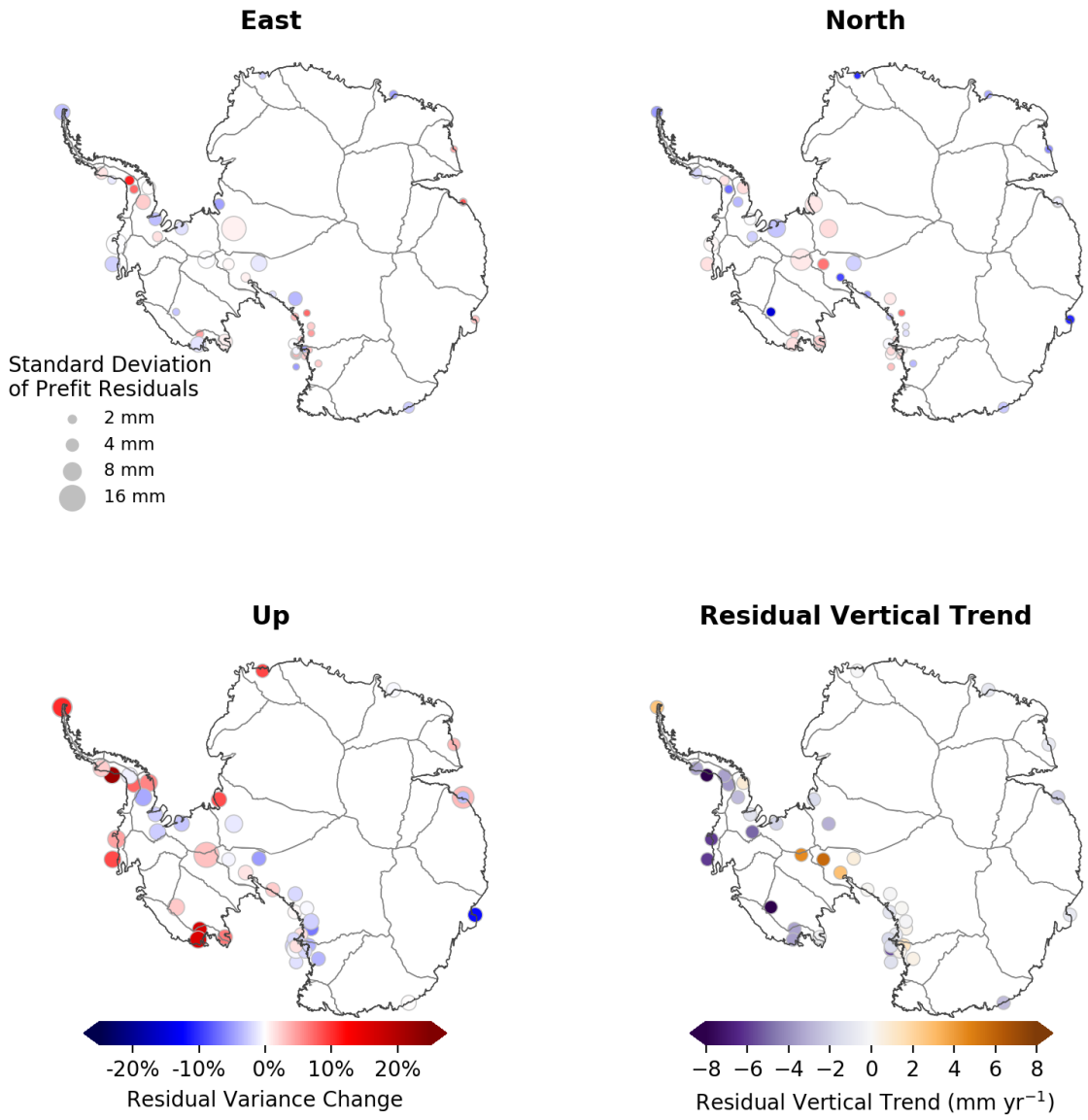

Figure 5.14: Change in variance of the detrended residual GNSS position time series relative to results obtained by computing elastic crustal deformation with the JPL RL05.1M mascon solutions after removing elastic crustal deformation predictions from the adjusted ice dynamics solution. The lower-right subplot compares the trends predicted by the output model to the data after correction with the Caron et al. (2018) GIA model.

$$P_{i|i-1} = FP_{i-1|i-1}F^T + Q \tag{5.35}$$

The covariance from the previous iteration consists of two diagonal scalar elements.

$$P_{i-1} = \begin{bmatrix} \sigma^2_{m,i-1|i-1} & 0 \\ 0 & \sigma^2_{\dot{m},i-1} \end{bmatrix} \tag{5.36}$$

The constant matrix Q contains the process noise associated with the variability of the instantaneous rate of change of the ice sheet.

$$Q = \begin{bmatrix} 0 & 0 \\ 0 & \sigma^2_{\text{ice}} \end{bmatrix} \tag{5.37}$$

The basic observation equation of the filter relates the total mass predicted by the model $m_{i|i-1}$.

$$m_{i|i-1} = H_i \mathbf{x}_{i|i-1}, \tag{5.38}$$

where

$$H_i = \begin{bmatrix} 1 & 0 \end{bmatrix}. \tag{5.39}$$

At each iteration, the filter must minimize the square of the difference between $m_{i|i-1}$ and the observed total mass $m_{i,\text{obs}}$. The solution update, $x_{i|i}$ may be estimated using the minimum mean square estimator:

$$\mathbf{x}_{i|i} = K_i(m_{i,\text{obs}} - m_{i|i-1}) + \mathbf{x}_{i|i-1}. \tag{5.40}$$

The Kalman gain K_i is defined as:

$$K_i = P_{i|i-1}H^T(HP_{i|i-1}H^T + R_i)^{-1}, \tag{5.41}$$

where $R = \left[r_i^2\right]$. The scalar quantity r_i^2 is computed as the sum of the GRACE measurement errors for month i, month 0, and the propagated GIA covariance between t_0 and t_i, or

$$r_i^2 = \sigma_{m,i}^2 + \sigma_{m,0}^2. \tag{5.42}$$

Similarly, the prediction variance is

$$\sigma_{m,i|i-1}^2 = HP_{i|i-1}H^T = \sigma_{\dot{m}_{\text{ice}}}^2 \Delta t^2 + \sigma_{m,i-1|i-1}^2. \tag{5.43}$$

These may be ingested into the definition of the Kalman gain to obtain

$$K_i = \frac{\sigma_{m,i|i-1}^2}{\sigma_{m,i|i-1}^2 + r_i^2} \begin{bmatrix} 1 \\ 0 \end{bmatrix}. \tag{5.44}$$

The updated covariance $P_{i|i}$ may be computed with the new Kalman gain as follows:

$$P_{i|i} = (I - K_i H)P_{i|i-1}. \tag{5.45}$$

The matrix $I - K_i H$ takes the form

$$I - K_i H = \begin{bmatrix} 1 - \frac{\sigma_{m,i|i-1}^2}{\sigma_{m,i|i-1}^2 + r_i^2} & 0 \\ 0 & 1 \end{bmatrix} \tag{5.46}$$

and the adjusted covariance is

$$P_{i|i} = \begin{bmatrix} \left(1 - \frac{\sigma_{m,i|i-1}^2}{\sigma_{m,i|i-1}^2 + r_i^2}\right) \frac{\sigma_{m,i|i-1}^2}{\sigma_{m,i|i-1}^2 + r_i^2} & 0 \\ 0 & \sigma_{\text{ice}}^2 \end{bmatrix}. \tag{5.47}$$

The filter is then incremented to month $i + 1$.

The cumulative mass time series is shown in Figure 5.15.

5.6 Conventional Kalman Filter

At each iteration, the ice dynamics grid obtained from Section 5.4 corresponding to the current month is added to the RACMO SMB field for the same month. The total mass flux

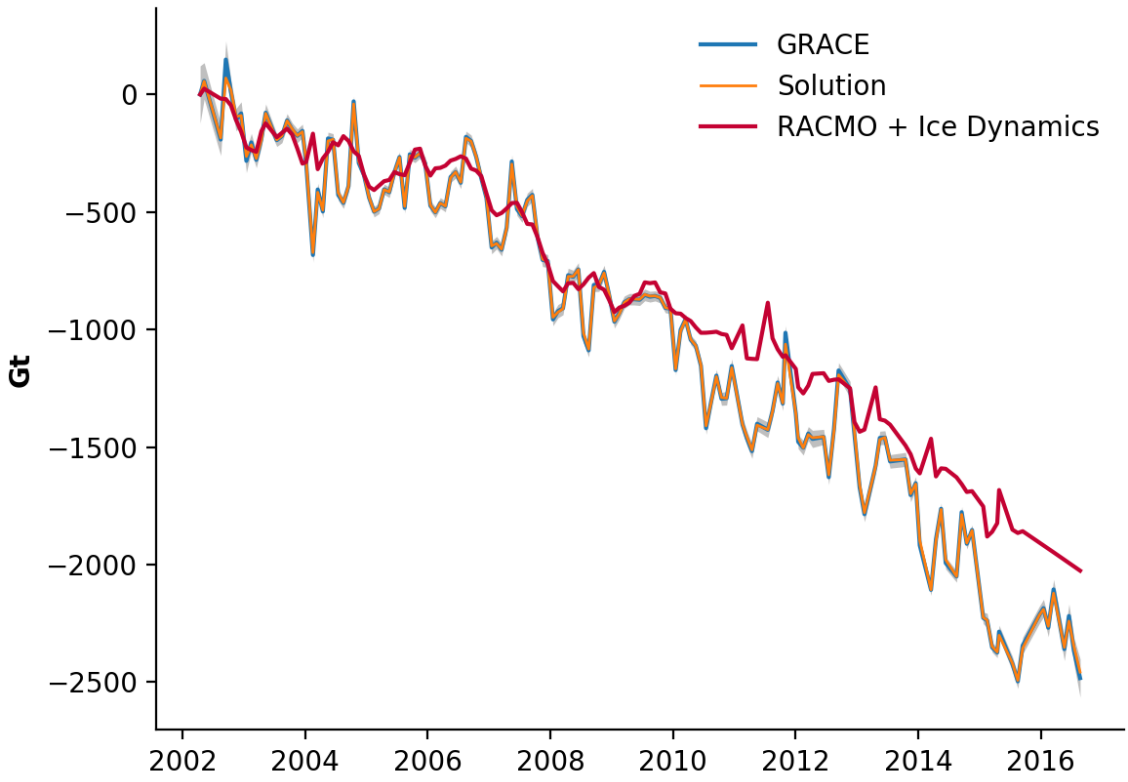

Figure 5.15: Total cumulative mass change of the Antarctic Ice Sheet obtained from the one-dimensional Kalman filter compared with input GRACE data and the sum of a priori ice dynamics and RACMO SMB.

field is integrated over the interval between the previous month and the current month and added to the mass field from the previous month. This mass field, which exists on a 27-km grid, is mascon-averaged and compared with the GRACE mascon estimates for the corresponding month. The observation deviation vector is then pushed through the Kalman gain operator to obtain a state deviation vector for the integrated mass change field. This state deviation is computed at a resolution of 108 km to reduce computation time, but is projected onto the 27-km land grid using nearest-neighbor interpolation.

$$\mathbf{x}_i = \begin{bmatrix} \mathbf{m}_i \\ \dot{\mathbf{m}}_i \end{bmatrix}. \tag{5.48}$$

As with the one-dimensional filter, the surface mass balance model used here has outputs available no later than December 2015, whereas the GRACE data runs to August 2016. SMB for months outside of the boundary are imputed with the average SMB field in the 2002–2016 period. For the purposes of this filter, the instantaneous mass change is integrated forward in time linearly as a function of $\Delta t_i = t_i - t_{i-1}$.

$$\mathbf{x}_{i|i-1} = \begin{bmatrix} \mathbf{m}_{i|i-1} \\ \dot{\mathbf{m}}_i \end{bmatrix} = F_i \mathbf{x}_{i-1|i-1} + \begin{bmatrix} 0 \\ \dot{\mathbf{m}}_i \end{bmatrix}. \tag{5.49}$$

The state transition matrix F_i is designed such that information about the rate of mass change is not preserved between iterations. Instead, the instantaneous rate of mass change is obtained from external models.

$$F_i = \begin{bmatrix} \delta_{jk} & \Delta t_i = t_i - t_{i-1} \\ 0 & 0 \end{bmatrix}. \tag{5.50}$$

The state also has an associated covariance. The covariance P_0 is initialized such that all terms in the 2x2 matrix are zero. The covariance for the current iteration is propagated forward in time from the previous iteration to the current iteration as follows.

$$P_{i|i-1} = F P_{i-1|i-1} F^T + Q \tag{5.51}$$

The covariance from the previous iteration consists of two block diagonal elements. This matrix is initialized at zero.

$$P_{i-1} = \begin{bmatrix} P_{\mathbf{m},i-1} & 0 \\ 0 & P_{\dot{\mathbf{m}},i-1} \end{bmatrix} \tag{5.52}$$

The constant matrix Q contains the process noise associated with the variability of the instantaneous rate of change of the ice sheet.

$$Q = \begin{bmatrix} 0 & 0 \\ 0 & P_{\text{ice}} \end{bmatrix} \tag{5.53}$$

The basic observation equation of the filter relates the total mass predicted by the model $\mathbf{m}_{i|i-1}$.

$$\mathbf{y}_{\text{GRACE,i}_{i|i-1}} = M\mathbf{m}_{i|i-1}, \tag{5.54}$$

where

$$H = \begin{bmatrix} M & 0 \end{bmatrix}. \tag{5.55}$$

At each iteration, the filter must minimize the square of the difference between $m_{i|i-1}$ and the observed total mass $m_{i,\text{obs}}$. The solution update may be estimated using the minimum mean square estimator:

$$\mathbf{m}_{i|i} = K_i(y_{\text{GRACE,i}_{i|i-1}} - M\mathbf{m}_{i|i-1}) + \mathbf{m}_{i|i-1}. \tag{5.56}$$

The Kalman gain K_i is defined as:

$$K_i = P_{i|i-1}H^T W(WHP_{i|i-1}H^T + WR_i)^{-1}. \tag{5.57}$$

The diagonal elements of R are derived from the mascon observation errors. Because of the setup of the filter, the errors associated with the initial month are added to the corresponding elements of this matrix. The diagonal elements of the weight matrix W are the squares of

$$\sigma^2_{m,i|i-1} = HP_{i|i-1}H^T \tag{5.58}$$

The updated covariance $P_{i|i}$ may be computed with the new Kalman gain as follows:

$$P_{i|i} = (I - K_iH)P_{i|i-1}. \tag{5.59}$$

The filter is then incremented to month $i + 1$.

The observation equations and filtering setup are similar to previous models. The adjusted trend is shown in Figure 5.16. Note the artifacts originating from diminished spatial resolution. The time series for total continental ice sheet mass variation is given in 5.17. Cumulative regional mass balance time series for this model are shown in Figure 5.18. Cumulative basin-by-basin mass balance time series for this model are shown in Figure 5.19. GNSS residuals are shown in Figure 5.20.

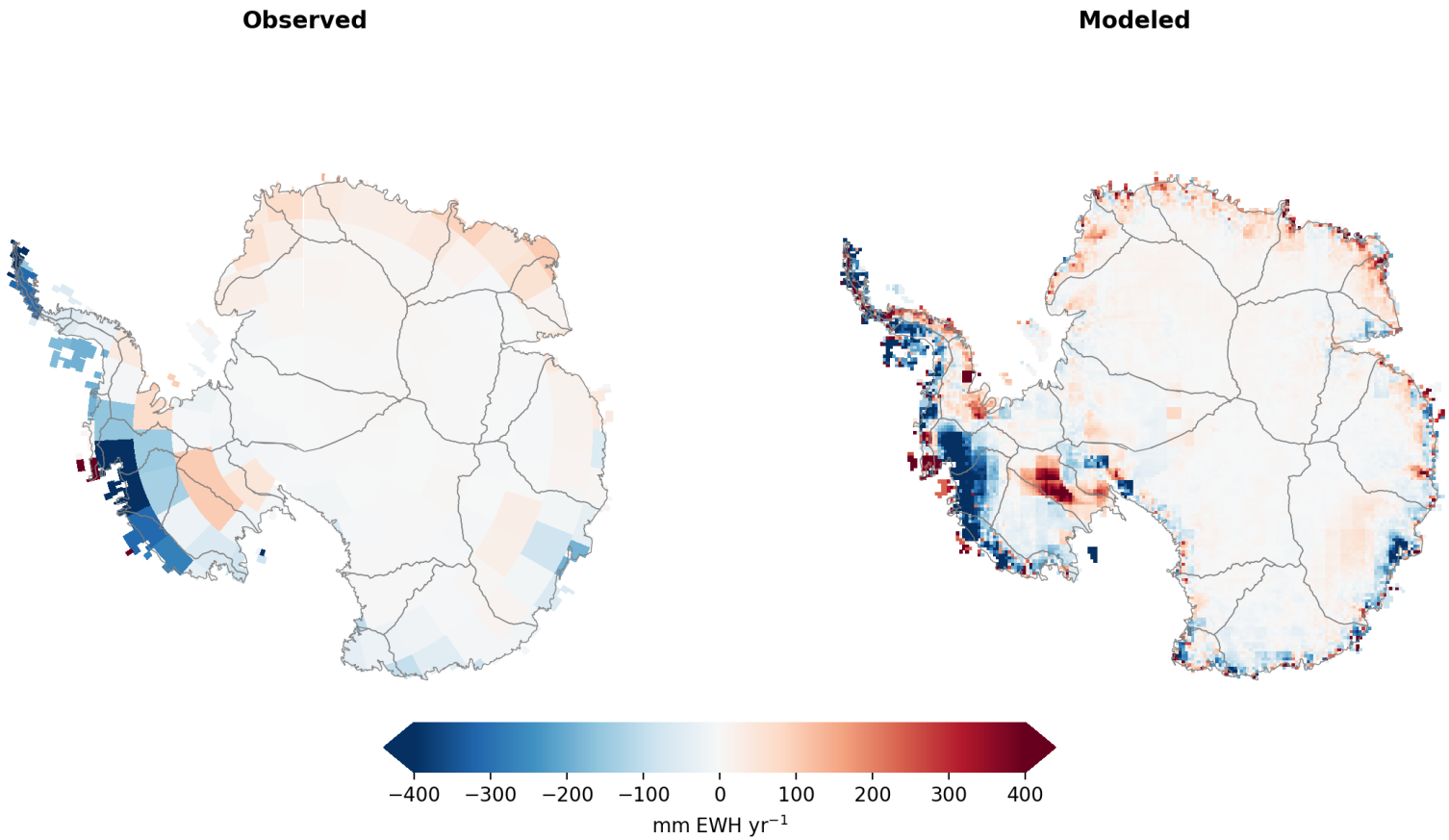

Figure 5.16: Input mascon trends over 2002–2017 interval and enhanced trends for the same time period obtained from the conventional Kalman filter. Note the coarser resolution of this solution.

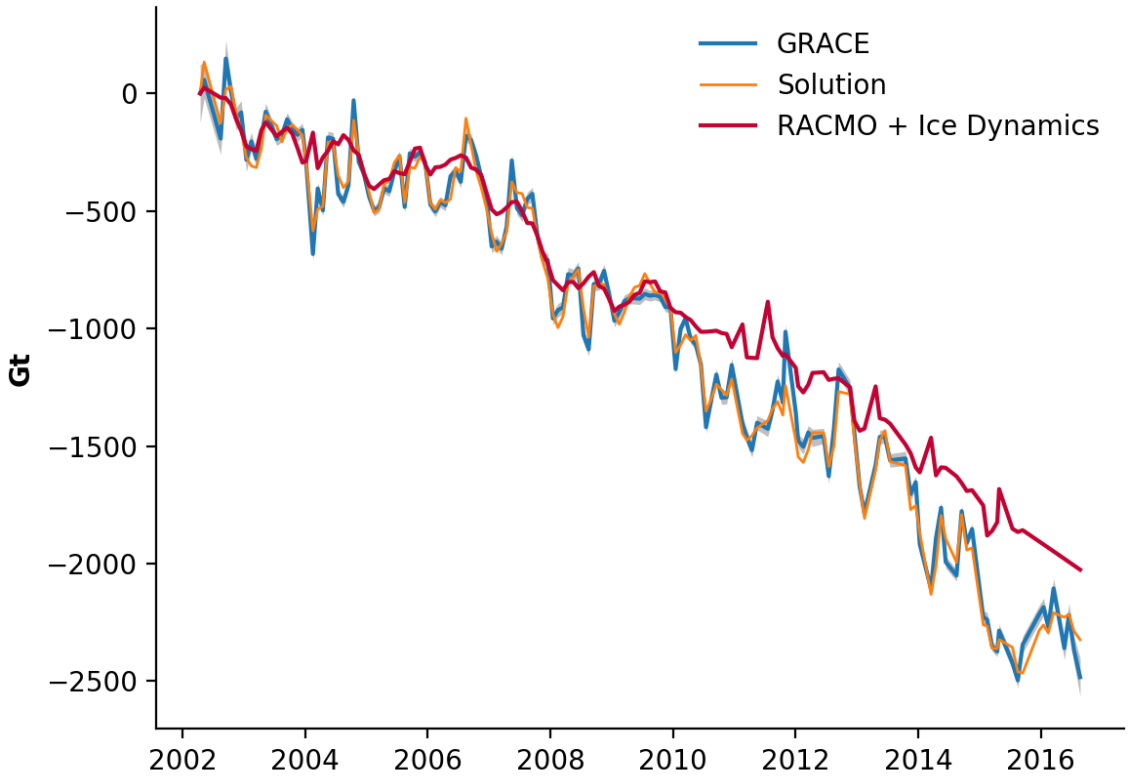

Figure 5.17: Mass change integrated over the entire Antarctic ice sheet from the conventional Kalman filter compared with its input GRACE data and corresponding 1-σ errors

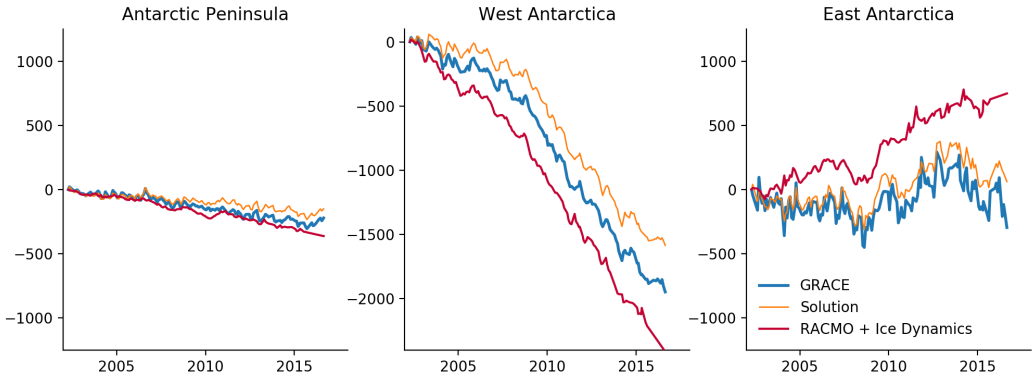

Figure 5.18: Mass change (Gt) from the conventional Kalman filter in Gt integrated over East Antarctica, West Antarctica, the Antarctic Peninsula compared with corresponding GRACE data

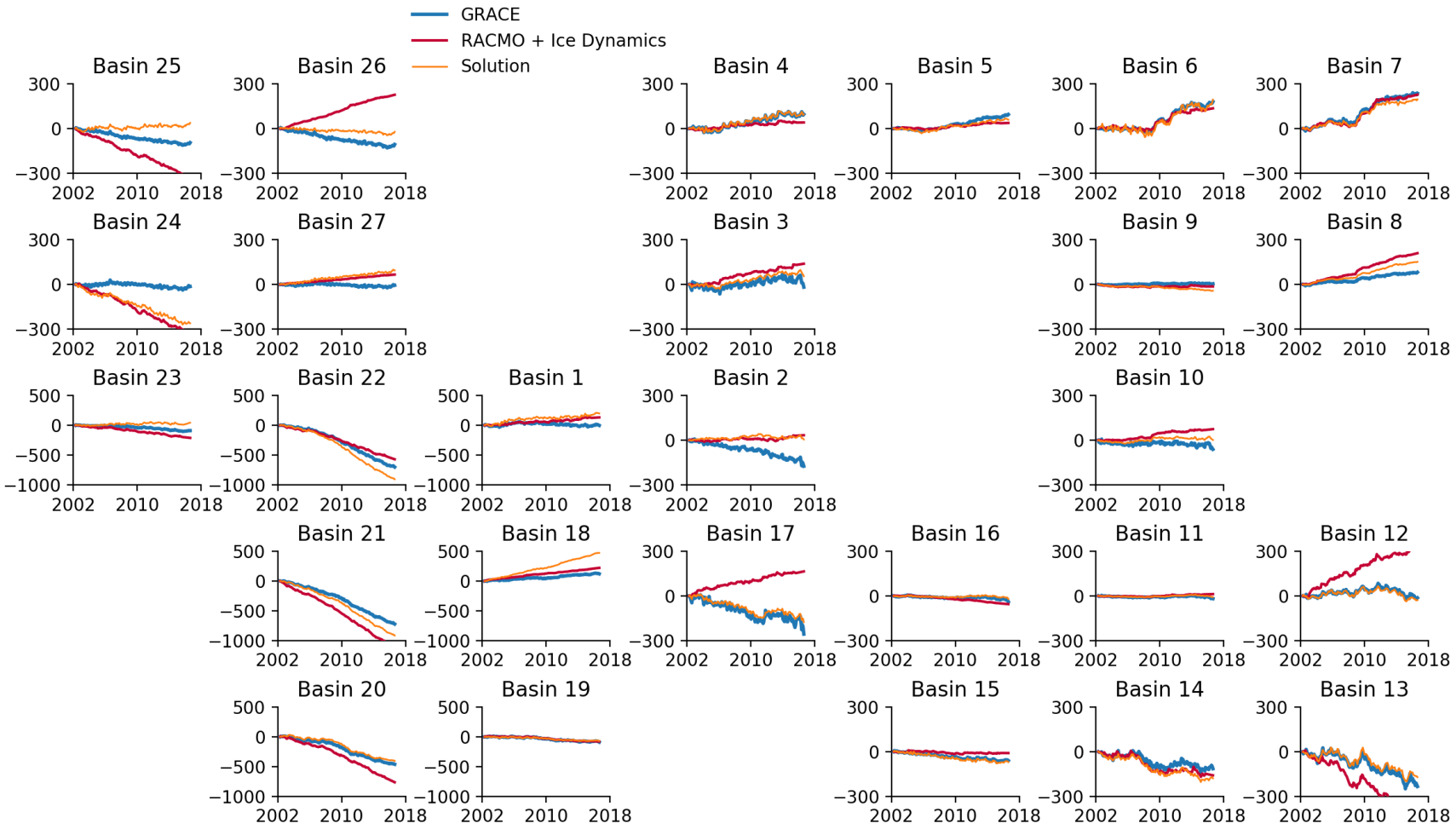

Figure 5.19: Basin-by-basin time series of mass change (Gt) obtained from the conventional Kalman filter and compared with GRACE

5.7 Discussion

The GRACE- and basin-discharge-constrained solutions all yield consistent mass loss estimates across the continent. The basin constraints notably have a slightly more conservative estimate of total acceleration in the 2002–2017 period. These solutions do not fit the JPL mascons well, with RMS residuals of over 200 mm EWH. Direct adjustment of mass fields with GRACE data fits the GRACE data with area-weighted RMS residuals of 24 mm EWH. The conventional Kalman filter has wRMS residuals of 14 mm EWH, comparable to the magnitude of atmospheric pressure errors in Antarctica. Mass loss estimates over the Antarctic Peninsula diverge widely across all solutions. All solution methods result in improvement in RMS residuals of GNSS trends relative to the elastic loading predicted by the JPL mascons. Detrended GNSS time series residuals generally show little overall change with any of these solutions, except in certain regions. Slight improvements may, for example, be seen in the horizontal components across the Transantarctic Mountains. No solution degrades the overall variance of the detrended GNSS residuals by more than 2%.

All solutions presented involve propagating uncertainties in mass change rates through time to inform the uncertainty and overall flexibility of the cumulative mass change field. Early iterations of these solutions techniques involved recursive modulation of the input mass rates themselves. In such a setup, cumulative mass errors at a particular instant are fed through a Kalman filter to damp or amplify the present rate of change in mass. This may be likened to a control algorithm, in which state derivatives at a present state are modulated by present state errors to minimize errors at a future state. Such a filter requires an explicit cross-covariance between surface mass balance. While this algorithm was successfully implemented with performance comparable to the extant methods in this work, the first-principles basis for the development of the cross-covariance was insufficient to justify inclusion in this work. This filter, instead, served as a prototype for the conventional Kalman filter presented in this work.

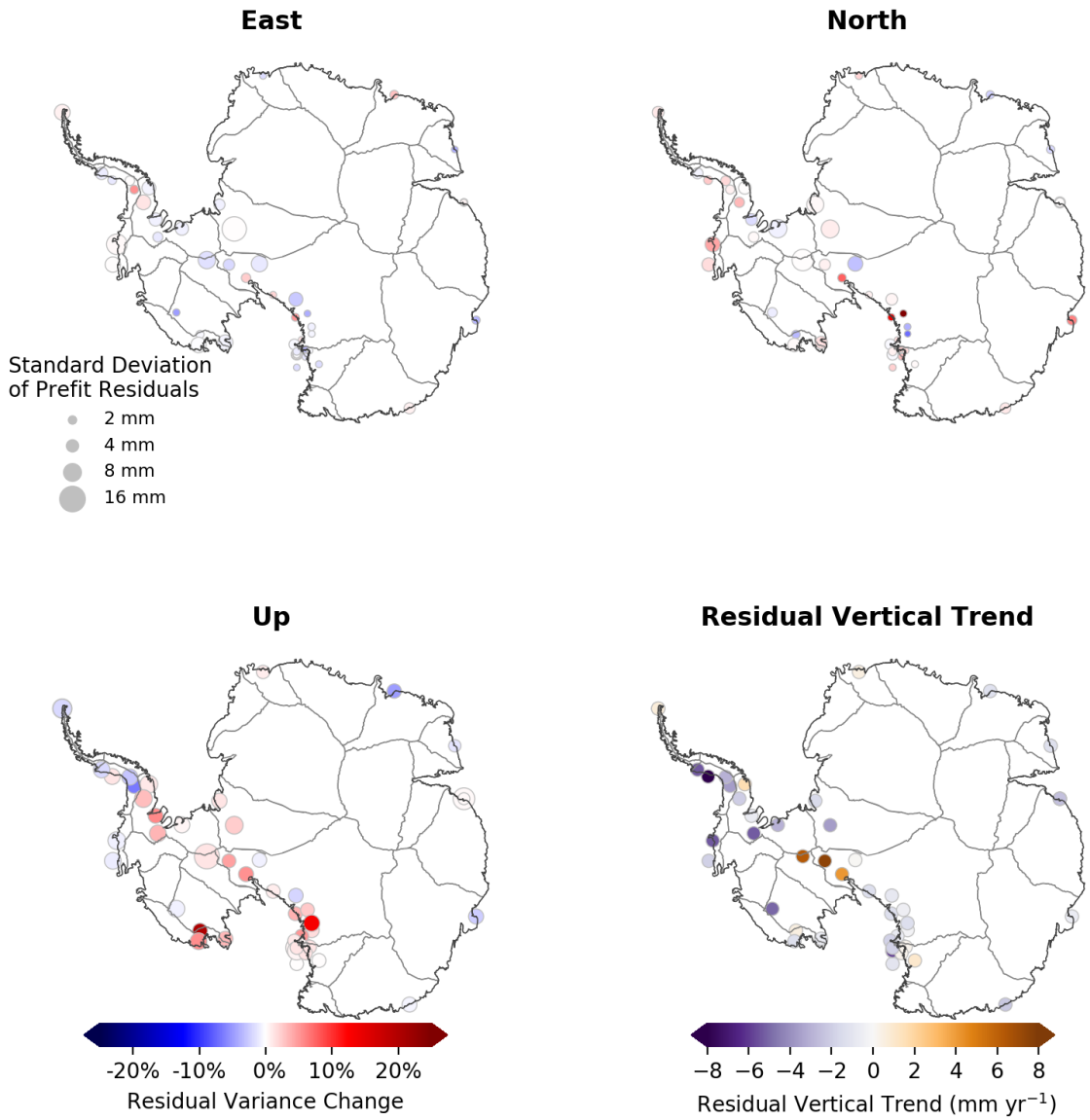

Figure 5.20: Change in variance of the detrended residual GNSS position time series relative to results obtained by computing elastic crustal deformation with the JPL RL05.1M mascon solutions after removing elastic crustal deformation predictions from the conventional Kalman filter. The lower-right subplot compares the trends predicted by the output model to the data after correction with the Caron et al. (2018) GIA model.

	Unit	JPL RL05.1M	RACMO +ICESat	Adjusted Ice Dynamics	Fixed-gain Kalman Filter	Conventional Kalman Filter
AIS Mass Rate	Gt yr^{-1}	-168.0 ± 2.8	+32.9 ± 1.5	-165.0 ± 1.5	-171.6 ± 2.7	-166.8 ± 2.5
AIS Acceleration	Gt y^{-2}	-13.5 ± 1.5	-3.8 ± 0.8	-10.0 ± 0.8	-13.5 ± 1.5	-13.1 ± 1.3
EAIS Mass Rate	Gt yr^{-1}	+36.5 ± 2.5	+192.1 ± 1.5	+78.0 ± 1.5	+33.2 ± 2.4	+27.3 ± 2.2
EAIS Acceleration	Gt y^{-2}	+2.7 ± 1.3	+3.0 ± 0.8	+3.0 ± 0.8	+2.3 ± 1.3	+3.0 ± 1.1
WAIS Mass Rate	Gt yr^{-1}	-139.8 ± 1.5	-141.7 ± 1.0	-185.5 ± 1.0	-134.8 ± 1.5	-127.9 ± 1.6
WAIS Acceleration	Gt yr^{-2}	-13.7 ± 0.8	-6.7 ± 0.5	-11.0 ± 0.5	-13.8 ± 0.8	-15.4 ± 0.8
AP Mass Rate	Gt yr^{-1}	-19.1 ± 0.4	-12.6 ± 0.3	-30.5 ± 0.3	-26.6 ± 0.5	-11.8 ± 0.4
AP Acceleration	Gt yr^{-2}	-0.4 ± 0.2	+0.2 ± 0.2	-0.7 ± 0.2	-0.6 ± 0.3	-0.9 ± 0.2

Table 5.1: Rates and accelerations for the major subdivisions of the Antarctic Ice Sheet predicted by each of the solutions presented in this Chapter. Residuals of GRACE and GNSS crustal motion time series of the various solutions developed in this chapter. Note that uncertainties are computed from the residuals of a polynomial fit and do not reflect the output filter covariances.

	Unit	JPL RL05.1M	RACMO +ICESat	Adjusted Ice Dynamics	Fixed-gain Kalman Filter	Conventional Kalman Filter
wRMS GRACE Residuals	mm EWH	0	174	205	24	14
wRMS GNSS Residual Trend	mm	2.13	1.87	1.92	2.07	2.02
GNSS Trend Δ Variance	%	+0.00	-22.07	-17.98	-3.29	-9.40
GNSS SDDR (Up)	mm	5.94	5.97	5.98	5.99	5.98
GNSS Δ Variance (Up)	%	+0.00	+0.82	+1.12	+1.60	+1.19
GNSS SDDR (East)	mm	3.27	3.26	3.25	3.27	3.26
GNSS Δ Variance (East)	%	+0.00	-0.41	-0.64	+0.08	-0.12
GNSS SDDR (North)	mm	2.88	2.87	2.87	2.88	2.89
GNSS Δ Variance (North)	%	+0.00	-0.54	-0.56	+0.30	+0.69

Table 5.2: Residuals of GRACE and GNSS crustal motion time series of the various solutions developed in this chapter

Chapter 6

Least-Squares Combination of GRACE and ICESat for Time-variable Mass Solutions

Thus far, this work has implemented a combination of altimetry and gravity trends, a combination of monthly gravity data with altimetry and constraints from background models. The previous chapter described the enhancement of monthly GRACE solutions with models and ICESat data. These enhancements are largely reliant on using high-resolution models and data to generate model covariances for the optimal redistribution of low-resolution measurements from GRACE. It would be preferable to require less model input and let the core GRACE and ICESat speak for themselves.

This chapter focuses on directly combining ICESat and GRACE data to produce time-variable mass solutions at the spatial and temporal resolution of ICESat. It begins with the production of ICESat elevation change grids for 17 ICESat cycles from overlapping footprints found in Chapter 4. These solutions are then compared with monthly GRACE solutions binned to the same altimetry cycles. Downsampling the altimetry data to the same resolution as GRACE enables an initial comparison of GRACE and ICESat time series. Both sets of time series are corrected for error sources and background signals, such as GIA, firn air content, atmospheric pressure errors, and ICESat inter-campaign biases before comparison.

These elevation and surface-mass flux time series may be regressed to infer the effective density of the surface material in Antarctica. They may also be combined at mascon resolution to create both surface mass flux solutions for the 17 ICESat cycles and a solution for a correction to

the GIA model. This low-resolution combination informs a subsequent combination at the full 27 km resolution of the gridded altimetry data .

The final product of this work is a set of corrections to the Caron et al. (2018) GIA model and 17 high-resolution maps of surface mass flux over the grounded portion of Antarctic Ice Sheet and Antarctica's major islands. These solutions are evaluated for effective spatial resolution, agreement with independent data, and agreement with previous work.

6.1 Data Reduction and Preprocessing

The combination of ICESat and GRACE requires the generation of solutions for surface elevation change for each ICESat cycle. The overlapping-footprint elevation differences from Chapter 4 were used as a starting point for the creation of these elevation change grids. Each shot pair was assigned to a spatial bin on a 27-km south-pole-centered stereographic grid and to one of 153 possible temporal difference bins corresponding to combinations of pairs of the 18 ICESat campaigns. Each shot pair contributed to an average elevation change within each spatiotemporal bin. The weight of each shot pair's contribution to the solution was determined by the degree of overlap of the larger shot footprint with the smaller footprint. This degree of overlap, computable from the radii and separation of both shots according to the formulation of Mandel and Agol (2002), defined the weight of each shot pair in each average. Over 350 million shot pairs contribute to these grids.

Each grid cell contains up to 153 elevation difference measurements for the 18 ICESat cycles. These elevation differences are then collapsed into a time series of 17 cycles with respect to a reference epoch using linear least squares. The input data are weighted by the sum of the overlap fractions of all available shots within an epoch pair. The reference datum was chosen to be laser 3E because of its centrality in the sequence of cycles and superlative availability of overlapping laser shots across all cycles. This process is repeated for all grids in which data are available to produce 17 elevation grids between 2003 and 2009. Corresponding formal uncertainties were computed from residuals of the predicted elevation differences with respect to the input data. The solutions for elevation change at each ICESat cycle are shown in Figure 6.1. Trends, shot densities, and the

spatial distribution of temporal resolution are illustrated in Figure 6.2.

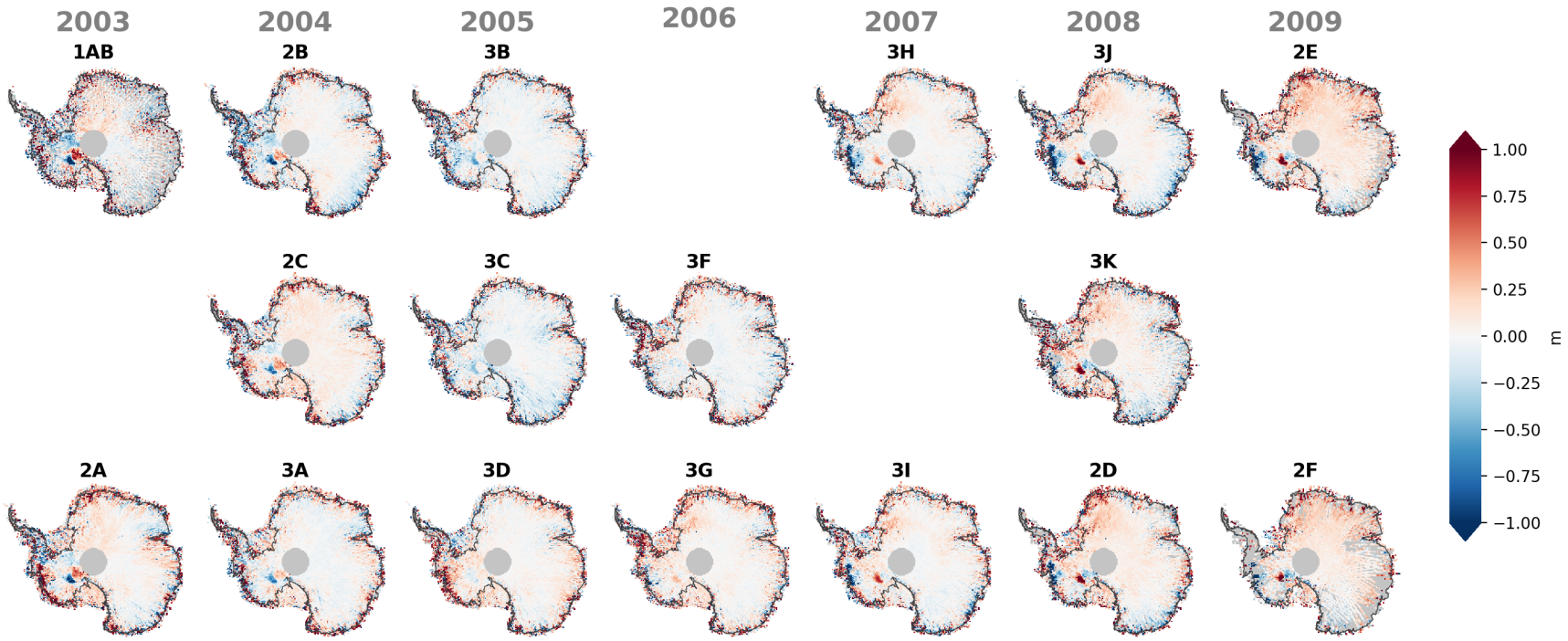

Figure 6.1: Time-variable altimetry solutions for 17 ICESat cycles between 2003 and 2009 relative to the Laser 3E (February/March 2006) campaign

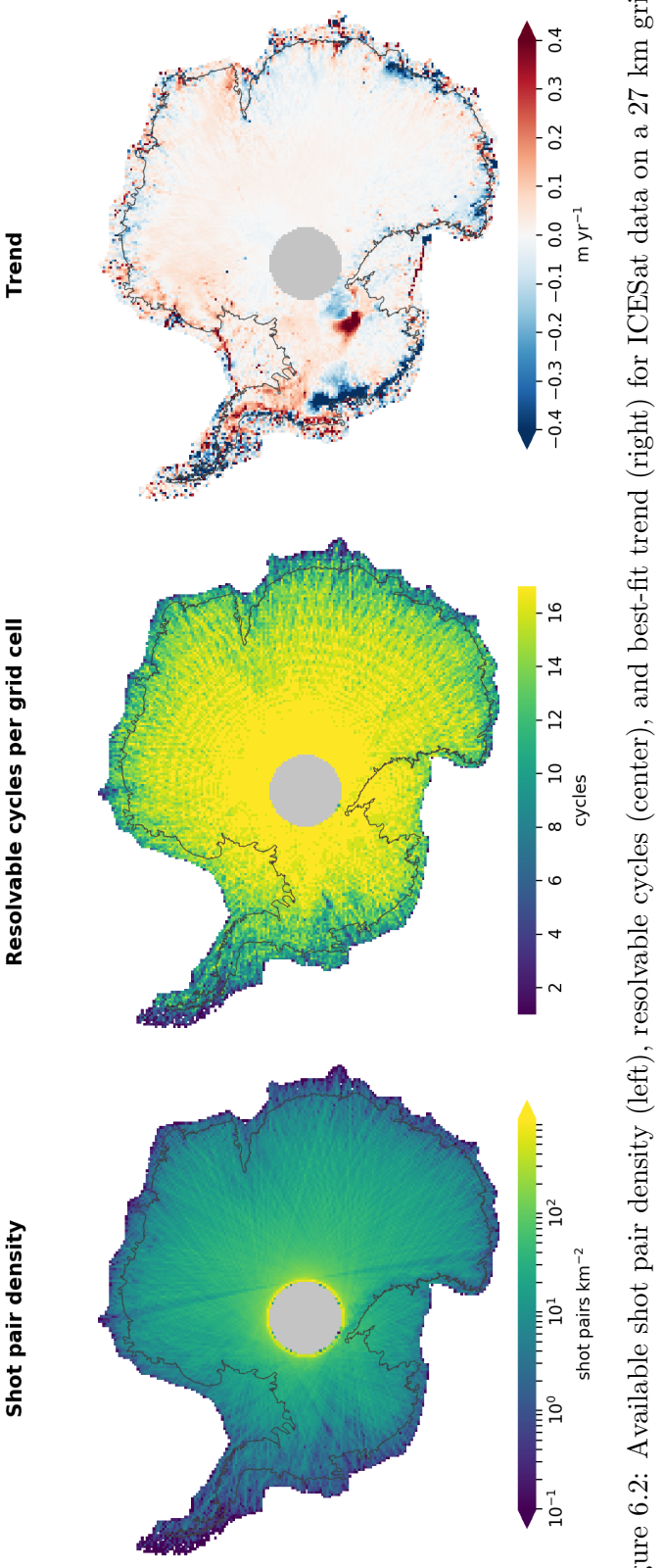

Figure 6.2: Available shot pair density (left), resolvable cycles (center), and best-fit trend (right) for ICESat data on a 27 km grid

The GRACE data used in this combination are the land components of the CRI-filtered JPL RL05.1M mascon solutions. As in Chapters 4 and 5, the input data is composed of 148 mascon time series, but the individual time series were resampled to match the corresponding ICESat data. Because multiple GRACE months may overlap with a single ICESat cycle, the GRACE months were binned into ICESat cycles using the number of overlapping days each GRACE month has within the corresponding ICESat cycle as a weight. Each ICESat cycle typically overlaps with two GRACE months. The major exceptions are Laser 2A (54 days, three GRACE months) and Laser 3K (14 days, no overlapping GRACE months). Because Laser 3K has no overlapping GRACE months, this cycle is filled using nearest-neighbor interpolation in time. The cycle-averaged GRACE data from Laser 3E were subtracted from all subsequent grids to match the reference epoch of the ICESat data.

The ICESat and GRACE data were corrected for geophysical and observational biases prior to combination and comparison. Both the ICESat and GRACE data were corrected for GIA using the Caron et al. (2018) GIA model uplift and mascon-averaged equivalent water height predictions, respectively. The integrated mass trend correction for GRACE was was 77 Gt yr^{-1} and the integrated volume correction for ICESat was 15 km^3 yr^{-1}. Surface pressure corrections from Hardy et al. (2017) were also subtracted from the GRACE data. Atmospheric modeling errors are at their most egregious between 2002 and 2007, which overlaps two-thirds of of the combination interval. Within the interval, these contain a trend of -16 Gt yr^{-1}, which was subtracted from the GRACE data. After these corrections have been applied, the trend in the input GRACE data between 2003 and 2009 is -102 Gt yr^{-1}.

The ICESat data were corrected for firn signals using the firn air content model of Ligtenberg et al. (2011). Unlike in Chapter 5, the firn air content only reflects the integrated void space within an ice column, rather than the sum of accumulated surface mass balance and firn air content. Subtracting firn air content alone should correct elevation signals such that they may be interpreted as linearly identical to mass changes of ice with a uniform density of 917 kg m^{-3}. The integrated magnitude of this correction is 28 km^3 yr^{-1}. The standard deviation of the detrended firn air

content was added in quadrature to the uncertainty of the original ICESat data to approximate firn error. Inter-campaign biases in ICESat data were measured by identifying a contiguous region above 2500 m elevation with annual precipitation of less than 30 mm EWH. ICESat-measured elevations in the low-precipitation zone (LPZ) were averaged for each cycle. The resultant the time series of LPZ biases was then subtracted from ICESat data for each cycle. The LPZ time series has a trend of 1.0 cm yr^{-1} of elevation, or 121 km^3 yr^{-1} integrated over the entire continent.

All pre-combination corrections are illustrated in Figure 6.3.

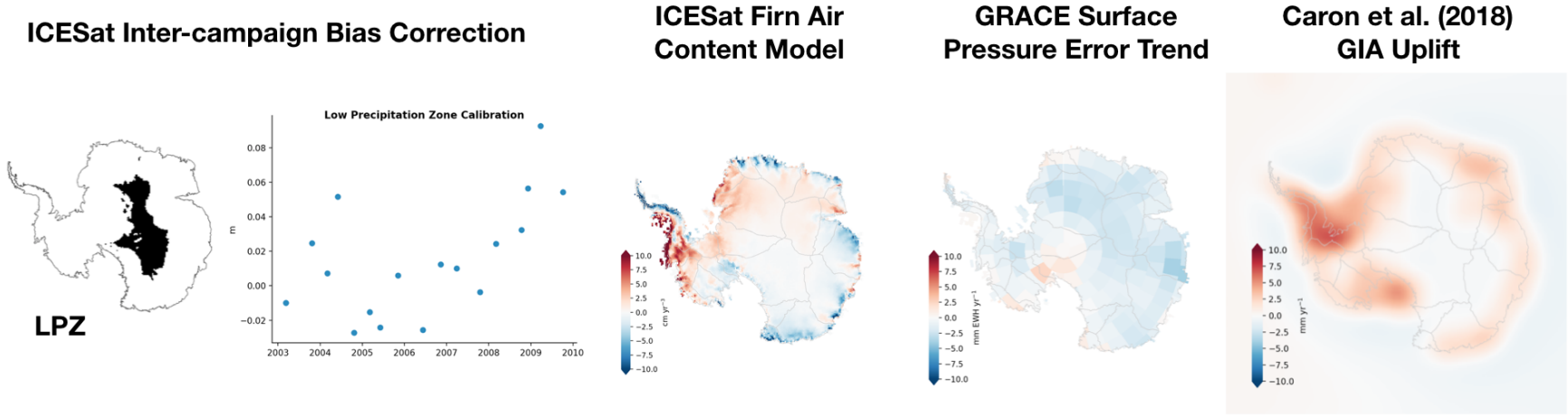

Figure 6.3: Representative corrections for (left to right): low-precipitation zone inter-campaign bias calibration and 2003–2009 trends for the firn air content calibration, GRACE surface pressure error corrections, and GIA uplift rates

6.2 Least-squares Combination

6.2.1 Examination of Time Series and Effective Densities

Prior to combination, we can inspect selected colocated time series of elevation and mass. For simplicity, the comparison is done by first mascon-averaging the ICESat data. Missing ICESat data were imputed by extrapolating the ICESat trend map found in Chapter 4 forward in time. A scale-agnostic comparison of these data is shown in Figure 6.4. Over regions of high mass change signal, (e.g., Pine Island, Thwaites, Kamb, and Totten) these time series are well-correlated. However, the low signal-to-noise ratio (SNR) of inland East Antarctic locations results in poor correlation of the GRACE and ICESat data. This low SNR is both a result of observational limitations in GRACE and unmodeled firn air content, which dilute the correlation between the time series. Over the Antarctic Peninsula, both ICESat and GRACE show strong trends, but broad disagreement in variation about these trends. The narrow north-south orientation of the Antarctic Peninsula creates an observability challenge for both ICESat and GRACE.

Further examination of Figure 6.4 shows that the the factor defining the relative scale of the GRACE time series does not correspond to the density of fully-compacted ice (917 kg m^{-3}) over most of the continent. It is generally expected that once firn air content has been subtracted from elevation data, the residual elevation signal is linearly related to gravity signals by the density of fully-compacted ice. To map effective density in space, an orthogonal regression of the GRACE and ICESat time series was performed for each mascon i and time index j:

$$h_{ij} = a_i m_{ij}. \tag{6.1}$$

The solution coefficient a_i represents a combination of average surface snow density within the mascon and a local elastic loading correction. The elastic loading effect is approximated by assuming that the ice sheet floats in a medium with the the average density of Earth's crust, 2.7 g cm^{-3}:

$$a_i = \frac{1}{\rho_i} - \frac{1}{\rho_{\text{crust}}} \tag{6.2}$$

Orthogonal regression, which minimizes the error-weighted sum of the squares in both the mass and elevation change time series was chosen over traditional linear least-squares regression to mitigate the effects of correlation dilution from low-SNR signals in East Antarctica. While GIA plays a role in the relationship between these time series, it was not included in this fit.

The results of the orthogonal regression, the effective densities, are shown in Figure 6.5 along with their uncertainties. These densities are most consistent with the expectation of 917 kg m^{-3} over West Antarctica, the Antarctic Peninsula, and Coats Land. Over East Antarctica. Negative densities are found in prominent pockets near Ellsworth Land and parts of the High Antarctic Plateau. The poor correlation of the time series in these regions is reflected in their high uncertainty. Over many of the remaining parts of the continent, the density is consistent with zero or the equilibrium firn densities modeled by Kaspers et al. (2004).

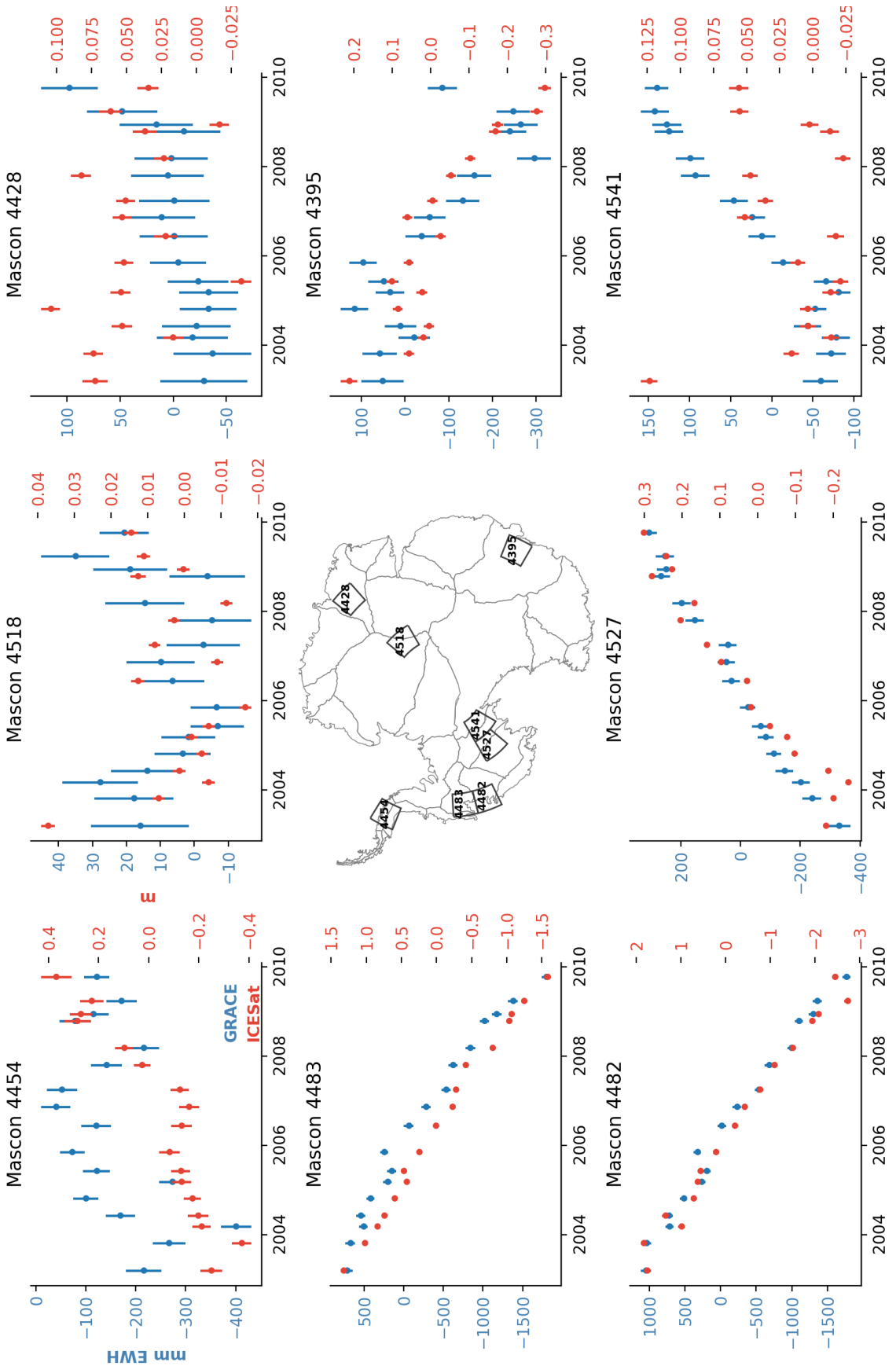

Figure 6.4: Comparison of selected GRACE mascon time series and corresponding mascon-averaged elevation time series

6.2.2 Time-Domain Combination at Mascon Resolution

The mascon-averaged altimetry time series may be combined with GRACE data at mascon resolution to yield cumulative mass balance for each cycle and a time-independent correction to the background GIA model. Each mascon time series pair forms a system of $2n$ sparse equations with $n+1$ unknowns, where n is the length of the time series (17 cycles). More explicitly,

$$\begin{bmatrix} y_{\text{GRACE},i,1} \\ y_{\text{GRACE},i,2} \\ \vdots \\ y_{\text{GRACE},i,n} \\ y_{\text{ICESat},i,1} \\ y_{\text{ICESat},i,2} \\ \vdots \\ y_{\text{ICESat},i,n} \end{bmatrix} = \begin{bmatrix} \Delta t_1 & 1 & & & \\ \Delta t_2 & & 1 & & \\ \vdots & & & \ddots & \\ \Delta t_n & & & & 1 \\ \frac{1}{\rho_{\text{GIA}}}\Delta t_1 & a_i & & & \\ \frac{1}{\rho_{\text{GIA}}}\Delta t_2 & & a_i & & \\ \vdots & & & \ddots & \\ \frac{1}{\rho_{\text{GIA}}}\Delta t_n & & & & a_i \end{bmatrix} \begin{bmatrix} m_{i,\text{GIA}} \\ m_{i,1} \\ m_{i,2} \\ \vdots \\ m_{i,n} \end{bmatrix} \tag{6.3}$$

The GIA model is parameterized in terms of equivalent water height and contributes to GRACE observations unitarily. The relationship between observed altimetry and GIA equivalent water height change is captured by an assumed mantle density of 4000 kg m^{-3}, following Gunter et al. (2014) and Riva et al. (2009). While Wahr et al. (1995) suggest that the asymptotic limit of effective mantle density is two-thirds the average density of Earth, or 3700 kg m^{-3}, Purcell et al. (2011) suggest a that this limit may be closer to 4200 kg m^{-3} over land. Effective mantle density over the Antarctic Peninsula may be lower because of its unique mantle structure. This work ultimately uses 4,000 kg m^{-3} everywhere to be consistent with Gunter et al. (2014) and Riva et al. (2009).

The data combination was performed by accumulating normal matrices and vectors for the system of equations. The diagonal elements of the mascon-projected covariance matrix from the GIA model Caron et al. (2018) were used as a constraint for the solution. The rationale for eliminating the off-diagonal terms is explained in Chapter 5.

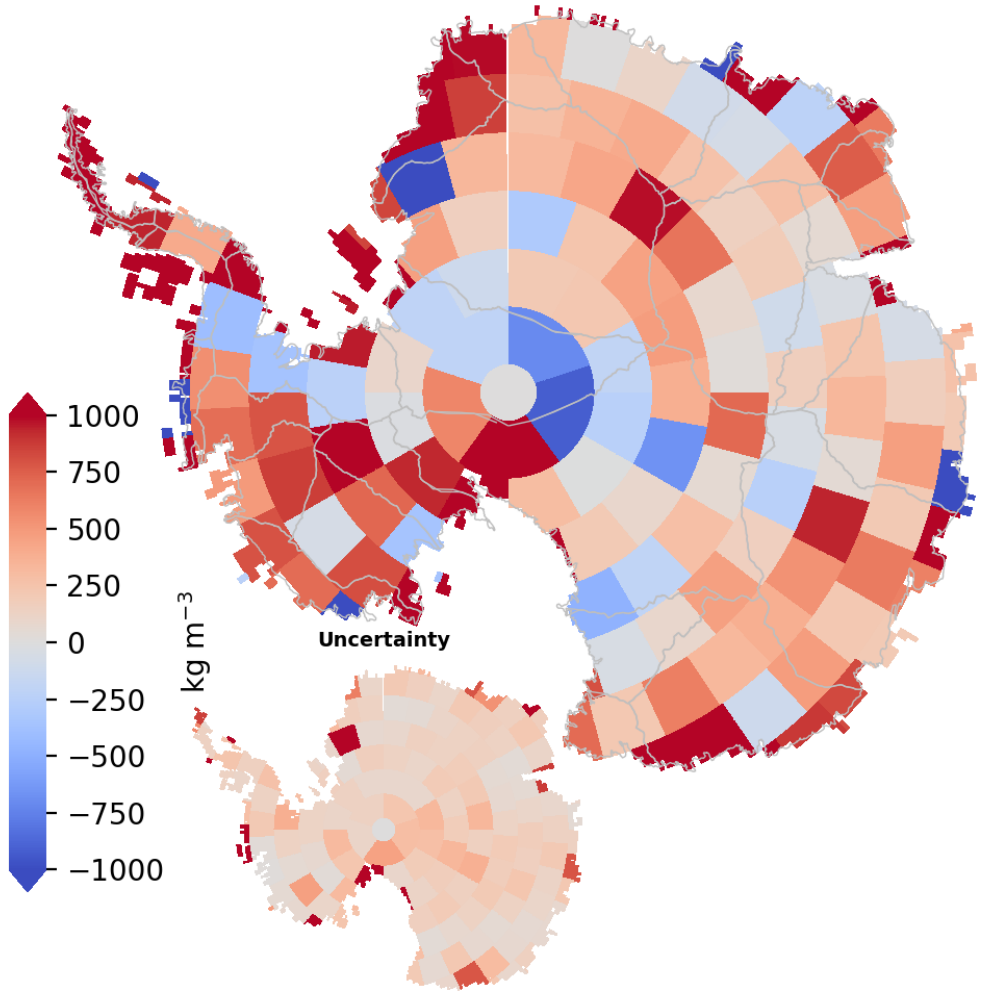

Figure 6.5: Best-fit, orthogonal-regression-based density solution from time series of ICESat and GRACE.

While the traditional approach for weighting the data involves the use of the inverse error variances of the input data as weights, we find that the high relative precision of the ICESat observations and their contributions to the mascon average will result in excessive weight being given to the ICESat data. Because the ICESat data contains spurious firn air content signals that will not be observable by GRACE, it is less important that the solution fits both time series within their own errors, but instead that the solution time series is maximally correlated with both input time series. The solution should therefore find the first principal component of both time series, optimally separating the latent mass change signals in both GRACE and ICESat and discarding spurious firn signals in ICESat.

This goal is met by weighting each input time series by its own inverse variance. This ensures that that a common spatial scale, both the GRACE and ICESat time series have the same approximate weight in the solution. However, if the ICESat data have additional firn signal, it should increase the overall variance of the ICESat signal, diminishing the weight of the ICESat data in the solution relative to the GRACE data.

$$w_{M,ii} = \frac{1}{\mathrm{var}(\mathrm{y_M})} \frac{\bar{\sigma}_M^2}{\sigma_{M,i}^2} \tag{6.4}$$

$$w_{A,ii} = \frac{1}{\mathrm{var}(\mathrm{y_A})} \frac{\bar{\sigma}_A^2}{\sigma_{A,i}^2} \tag{6.5}$$

The values $\sigma_{M,i}^2$ and $\sigma_{A,i}^2$ are the variances from the errors provided for each data point in the time series at each mascon. These values are normalized by their respective means, $\bar{\sigma}_M^2$ and $\bar{\sigma}_M^2$ but their relative variations are preserved to minimize the impact of known outliers on the solution.

Least-squares combinations of ICESat and GRACE were performed with various surface densities. The four models tested were: the "ice" model with surface density of 917 kg m^{-3} everywhere; the "equilibrium firn" density model of Kaspers et al. (2004), a hybrid density model in which everywhere above an elevation of 2000 m was assigned the equilibrium density model and every location below this elevation was assigned fully compacted ice; and the empirical orthogonal regression model discussed earlier. Results are shown in Table 6.1. The performance of each model

	Ice	Equilibrium Firn	Hybrid	Best-Fit
50% Density Range (kg m^{-3})	917	360–400	360–917	230–900
Ice Mass Trend (Gt yr^{-1})	-174 ± 156	-122 ± 59	-183 ± 92	-140 ± 56
GIA Mass Trend (Gt yr^{-1})	112 ± 131	112 ± 49	110 ± 69	100 ± 38
Reduced χ^2	229	226	219	25

Table 6.1: Results of mascon-resolution least-squares combinations with various density models

was assessed by computing the reduced χ^2 of each model, or the error- and degree-of-freedom-normalized sum of squared residuals. Instead of using the variance-based solution weights in the computation of least squares, the original inverse error variances were used. Thus, the reduced χ^2 exceeds 200 for three of the models.

Naturally, the empirical model is the best-fitting by an order of magnitude because this model was obtained by fitting both ICESat and GRACE. However, the values found in this fit, many of which are strongly negative or close to zero, are not usable without a natural physical basis to assign these densities. The best-performing model remaining is the hybrid model, which both captures intense coastal ice dynamics signals and fits weaker inland signals well. The quality of these models may also be assessed by their signal-to-noise ratio (SNR). The fully-compacted ice solution has too much inland noise, resulting in an unusable SNR, while the hybrid model has a higher SNR. The results from the hybrid fit are compared with the original input datasets in Figures 6.6 and 6.7.

The choice of densities in the solution is important to its integrity. The hybrid density model was chosen as the best compromise between the orthogonal regression density solution and the fully-compacted ice density model. Variance-based weighting was deemed necessary to properly balance the uncertainties in each dataset and find solutions that are maximally correlated with both ICESat and GRACE.

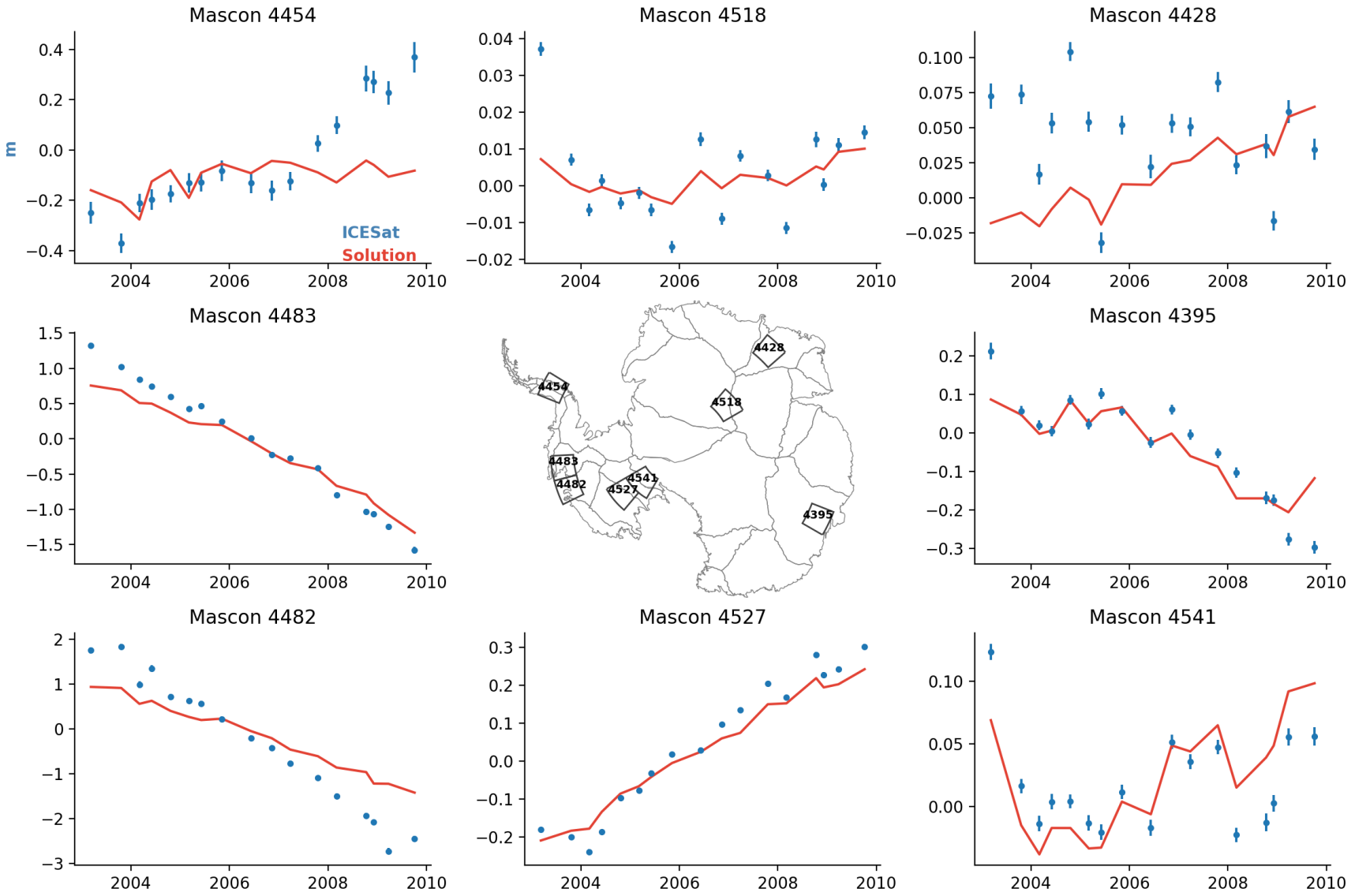

Figure 6.6: Comparison of best-fit predicted predicted altimetry time series using the hybrid surface density model with input mascon-averaged ICESat data. GIA predictions have been restored.

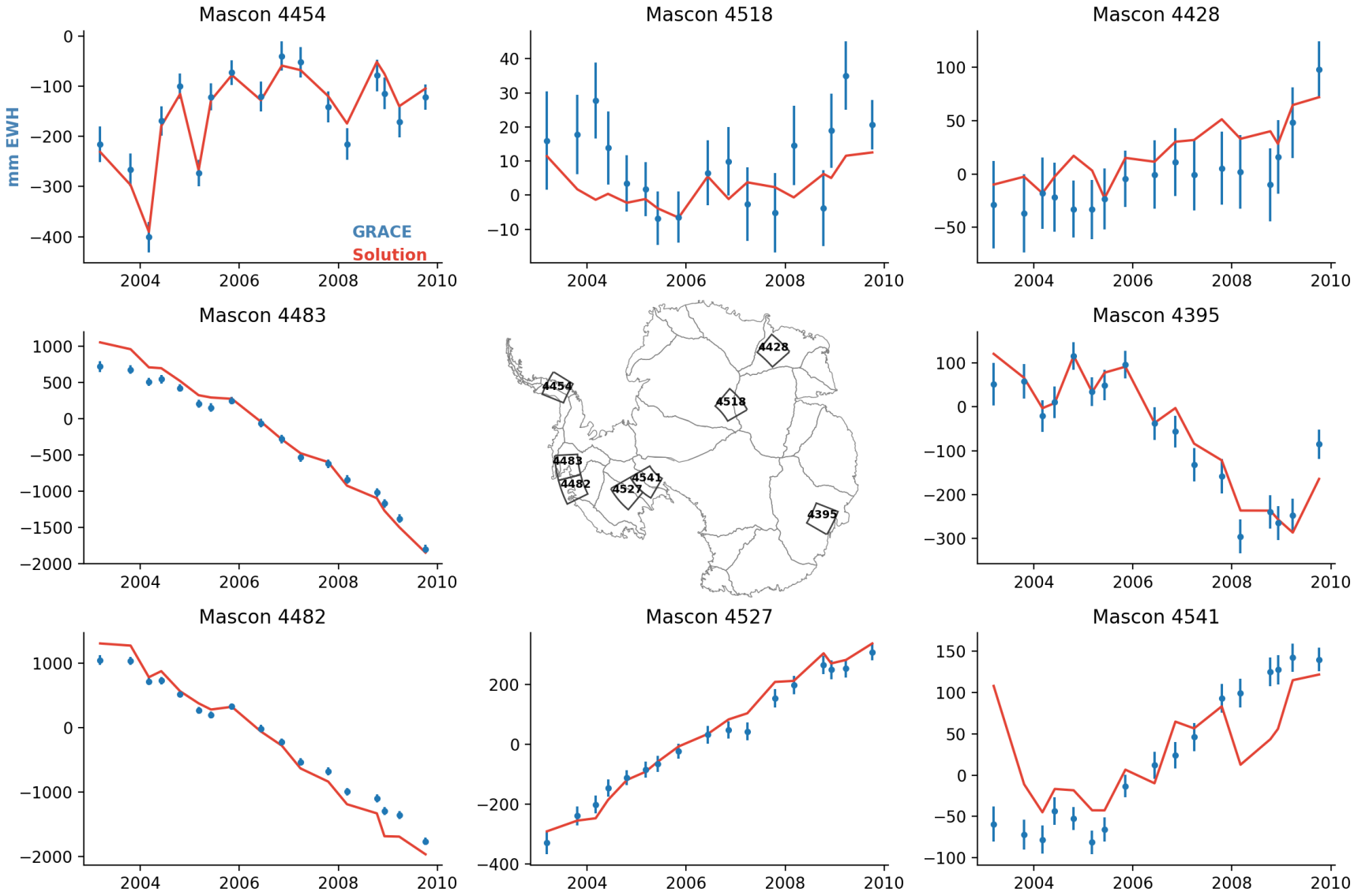

Figure 6.7: Comparison of best-fit predicted predicted surface mass flux time series obtained from combining GRACE and ICESat with a hybrid surface density model with mascon-scale GRACE data. GIA predictions have been restored.

6.3 Full-Resolution Combination

The goal of this work is to combine GRACE and ICESat data at the resolution of the input ICESat data (27 km). Like the previous solution, the solution consists of 17 grounded mass change vectors for the ICESat cycles, each with length 17,880, and one GIA deviation vector with length 148. Comprising the input data are 17 vectors of length 17880 for the altimetry and 17 vectors of length 148 for the mascon data. Missing altimetry data are handled by setting the corresponding weights to zero.

The observation matrix is sparse, and consists of four unique operators M, A, G_M and G_A. The M operator is the mascon-averaging operator, a 148x17880 sparse matrix that performs area-weighted averaging within the bounds of a mascon. The A operator, a 17880x17880 dense matrix, captures the effect mass variation has on altimetry. It combines both spatially variable ice density and Green's functions for elastic loading. The G_M matrix relates GIA mass variation to the land components of CRI-filtered JPL mascon equivalent water height rates. Because the GIA model is parameterized to match the mascon data, this matrix takes the form of a 148-by-148 identity matrix. Finally, the G_A operator captures the effect GIA has on observed altimetry rates. This matrix may be viewed as a mascon back-projection operator divided by a scalar mantle density of 4000 kg m^{-3}. The G_A and G_M operators are customarily multiplied by a scalar time deviation at each cycle to project GIA trends into the measurement space.

The full observation equation takes the form

$$\begin{bmatrix} \mathbf{y}_{\text{GRACE},1} \\ \mathbf{y}_{\text{ICESat},1} \\ \mathbf{y}_{\text{GRACE},2} \\ \mathbf{y}_{\text{ICESat},2} \\ \vdots \\ \mathbf{y}_{\text{GRACE},n} \\ \mathbf{y}_{\text{ICESat},n} \end{bmatrix} = \begin{bmatrix} \Delta t_1 G_M & M & & & \\ \Delta t_1 G_A & A & & & \\ \Delta t_2 G_M & & M & & \\ \Delta t_2 G_A & & A & & \\ \vdots & & & \ddots & \\ \Delta t_n G_M & & & & M \\ \Delta t_n G_A & & & & A \end{bmatrix} \begin{bmatrix} \mathbf{x}_{\text{GIA}} \\ \mathbf{m}_1 \\ \mathbf{m}_2 \\ \vdots \\ \mathbf{m}_n \end{bmatrix} \tag{6.6}$$

The sparse observation matrix has 306,476 rows and 304,108 columns. The system of equations has 2,368 degrees of freedom. The sheer size of the observation matrix means that direct solution of this least-squares problem cannot be achieved with an ordinary hardware setup. The sparsity of the observation equations, however, does result in a partially block-diagonal information matrix when assembling the final normal equations. This configuration fits a common problem in geodesy, where a time-independent background model is fit alongside time-dependent parameters.

The blockwise least squares solution algorithm is detailed in Kaula (1966). In it, the sparse normal equations formed by in the least squares solution are broken up into smaller time-dependent and time-independent components. Information matrices and vectors are accumulated for time-independent parameters alongside the information vectors, information matrices, and cross-information vectors and matrices of time-dependent mass variation parameters.

The GIA information vector $\mathbf{s}_{\text{GIA}}$ and matrix N_{GIA} are accumulated across all data cycles.

$$N_{\text{GIA}} = \sum_{i=1}^{n} \Delta t_i^2 [G_M^T W_{M,i} G_M + G_A^T W_{A,i} A G_A] + \bar{P}_{\text{GIA}}^{-1} \tag{6.7}$$

$$\mathbf{s}_{\text{GIA}} = \sum_{i=1}^{n} \Delta t_i [G_M^T W_{M,i} \mathbf{y}_M + G_A^T W_A \mathbf{y}_A] \tag{6.8}$$

At each iteration, the intrinsic information matrices and vectors (N_i and $\mathbf{s}_i$) for the high-resolution mass solution are collected alongside the time-dependent cross-information matrices $N_{i,\text{cross}}$ illustrating relating GIA and mass variation.

$$N_i = M^T W_{M,i} M + A^T W_{A,i} A + \bar{P}^{-1} \tag{6.9}$$

$$N_{i,\text{cross}} = \Delta t_i [M^T W_{M,i} G_M + A^T W_{A,i} G_A] \tag{6.10}$$

N_i and $N_{i,\text{cross}}$ are combined at each iteration and accumulated to form an intermediate time-independent information matrix and information vector used to decorrelate GIA and surface mass variation before the final solution of $\hat{\mathbf{x}}_{GIA}$.

$$N' = \sum_{i=1}^{n} N_{i,\text{cross}}^T N_i^{-1} N_{i,\text{cross}} \tag{6.11}$$

$$\mathbf{s}' = \sum_{i=1}^{n} N_{i,\text{cross}}^T N_i^{-1} \mathbf{s}_i \tag{6.12}$$

After accumulation, the time-independent best-fit GIA solution vector $\hat{\mathbf{x}}_{GIA}$ is inverted along with its error covariance $\hat{P}_{\text{GIA}}$.

$$\hat{\mathbf{x}}_{GIA} = [N_{\text{GIA}} - N']^{-1} [\mathbf{s}_{\text{GIA}} - \mathbf{s}'] \tag{6.13}$$

$$\hat{P}_{\text{GIA}} = [N_{\text{GIA}} - N']^{-1} \tag{6.14}$$

Once the GIA solution exists, it it possible to generate solutions for time-dependent mass variation solutions $\hat{\mathbf{m}}_i$ and the corresponding error covariance $\hat{P}_i$.

$$\hat{\mathbf{m}}_i = N_i^{-1} [\mathbf{s}_i - N_{i,\text{cross}} \hat{\mathbf{x}}_{\text{GIA}}] \tag{6.15}$$

$$\hat{P}_i = \left[N_i - N_{i,\text{cross}} N_{\text{GIA}} N_{i,\text{cross}}^T \right]^{-1} \tag{6.16}$$

The information matrices for GIA and cycle mass balances included smoothing constraints to aid in filling data gaps and erase the boundaries between mascons. The GIA constraint came from the diagonal elements of the mascon-averaged covariance matrix in the Caron et al. (2018) GIA model. The smoothing constraint was represented by a Gaspari-Cohn (Gaspari and Cohn, 1999)

function with a half-radius of 75 km and a diagonal covariance amplitude of 10^8 mm^2 EWH. The Gaspari-Cohn operator was chosen for its inherent suitability for sparse correlations. The inversion of the isotropic covariance matrix was performed via fast Fourier transform. Within the area south of 86° S, where ICESat cannot observe, a smaller constraint amplitude of 10^4 mm^2 EWH to ensure the smoothness of the resulting solution.

The construction of the altimetry component of the information matrix, $A^T W_{A,i} A$ at each iteration was a computational bottleneck because of the dimensions of the A matrix and the variability of the weight matrix between cycles. The computing time and memory requirements were reduced substantially through series expansions of this problem, based on the observation that the diagonal elements of the observation matrix (surface ice plus elastic loading) were several orders of magnitude larger than the off-diagonal terms (elastic deformation only). Therefore, breaking the A matrix into diagonal and off-diagonal components enabled a binomial decomposition of the product $A^T W_A A, iA$. If $A = A_{\text{diag}} + A_{\text{off}}$, where A_{diag} contains the diagonal elements of A and A_{off} contains the off-diagonal elements, then $A^T W_A A = A^T_{\text{diag}}[W_A A_{\text{diag}}] + A^T_{\text{diag}}[W_A A_{\text{off}}] + [W_A A_{\text{off}}]^T A_{\text{diag}} + A^T_{\text{off}}[W_A A_{\text{off}}]$. The first term $A^T_{\text{diag}}[W_A A_{\text{diag}}]$ may be computed in linear $O(n)$ time, while the next two terms $A^T_{\text{diag}}[W_A A_{\text{off}}] + [W_A A_{\text{off}}]^T A_{\text{diag}}$ are computable in $O(n^2)$ time. The final term, $A^T_{\text{off}}[W_A A_{\text{off}}]$ where the small off-diagonal elements are multiplied together create a negligible contribution to the content of the information matrix, but require $O(n^3)$ time to compute. The elimination of this term substantially reduces computation time and memory demand with minimal impact on the solution.

The best-fit solution trend is found in Figure 6.8. Note that the inputs to the trend fit are weighted by the inverse formal error variances from the combination.

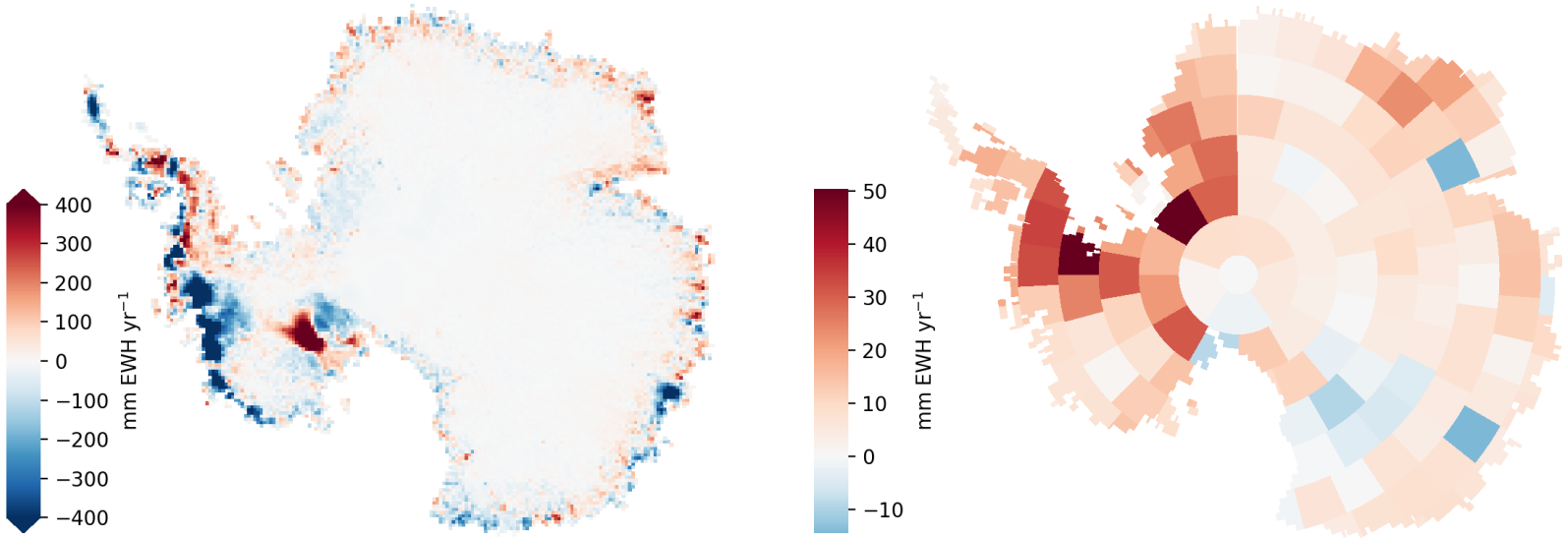

Figure 6.8: High-resolution ice mass trends for 2003–2009 (left) and GIA solution (right) obtained from least-squares combination of GRACE and ICESat

Uncertainty bounds were estimated using a bootstrap method (Press et al., 2007) . To speed up processing time, the observation equations were broken up mascon-by-mascon such that high-resolution solutions were computed within the bounds of a mascon, but were uncorrelated with solution coefficients in other mascons. The tradeoff of this speedup was that elastic loading and spatial smoothing could not be implemented across mascon bounds. For each mascon, the unaltered time series of GRACE data was injected into the normal equations. At each cycle within the mascon, altimetry data were spatially resampled with replacement. This means that certain values of $\mathbf{y}_{A,i}$ and $W_{A,i}$ and corresponding rows of the matrix A appeared multiple times within a resampled iteration. As before, the information vectors and matrices and the corresponding cross-information vectors and matrices for the mascon subvector were accumulated and inverted to solve for GIA and high-resolution mass-variation within that mascon. The mass variation subvector is added to a master vector of mass variation for the entire continent. This process is repeated 300 times–the maximum feasible number of iterations given time constraints–to generate a posterior distribution of possible mass variation and GIA solutions given the input data and realistic variations therein.

The ensemble of solutions may be used to compute a distribution of continental mass trends and total GIA correction. The posterior distribution of integrated mass change of the bootstrap are shown in Figure 6.9.

These solution distributions notably exhibit long, mirrored tails that reflects a strong anti-correlation between mass trend and total GIA signal. Continent-wide, the total GIA solution is nearly perfectly anti-correlated with the mass trend solution. This is also true for East Antarctica. Correlations between GIA and estimated ice mass trend over West Antarctica and the Antarctic Peninsula are weaker, at -0.50 and -0.37, respectively.

The distribution obtained from the bootstrap is used to construct a 1σ confidence around the best-fit estimate. Because these distributions are highly skewed, their asymmetry is expressed according to the deviation of the 15.9th and 84.1st percentiles from the solution. The continent-integrated mass change trend between 2003 and 2009 of -116^{+10}_{-51} Gt yr^{-1} is within 1σ of the 2002–2007 IMBIE (Shepherd et al., 2018) estimate of -73 $\pm$ 53 Gt yr^{-1}. Over West Antarctica,

recovered mass loss of -78 $^{+4}_{-11}$ Gt yr^{-1} remains consistent with the IMBIE estimate of -65 $\pm$ 27 Gt yr^{-1}. Further regional comparison of these solutions is shown in Table 6.2.

The quality of the solution may be examined by assessing its best and worst cases. Laser 2A, corresponding to late 2003, has laser shots available over 90% of the continent (Figure 6.10). However, altimetry coverage is unavoidably poor over the Antarctic Peninsula. This results in medium-wavelength ringing and other instabilities in this region. Elsewhere, particularly above 2000 m elevation, the solution recovers smooth variation in ice mass primarily attributable to surface mass balance. Near the coast, the solution exhibits the essential ice dynamics features. The mass loss signals from the Pine Island and Thwaites glaciers are recovered in detail, as are the more spatially concentrated signals on the Bakutis and Hobbs Coasts. The model further captures the ice dynamics gains in the Kamb Ice Stream and the mass loss signal near Totten.

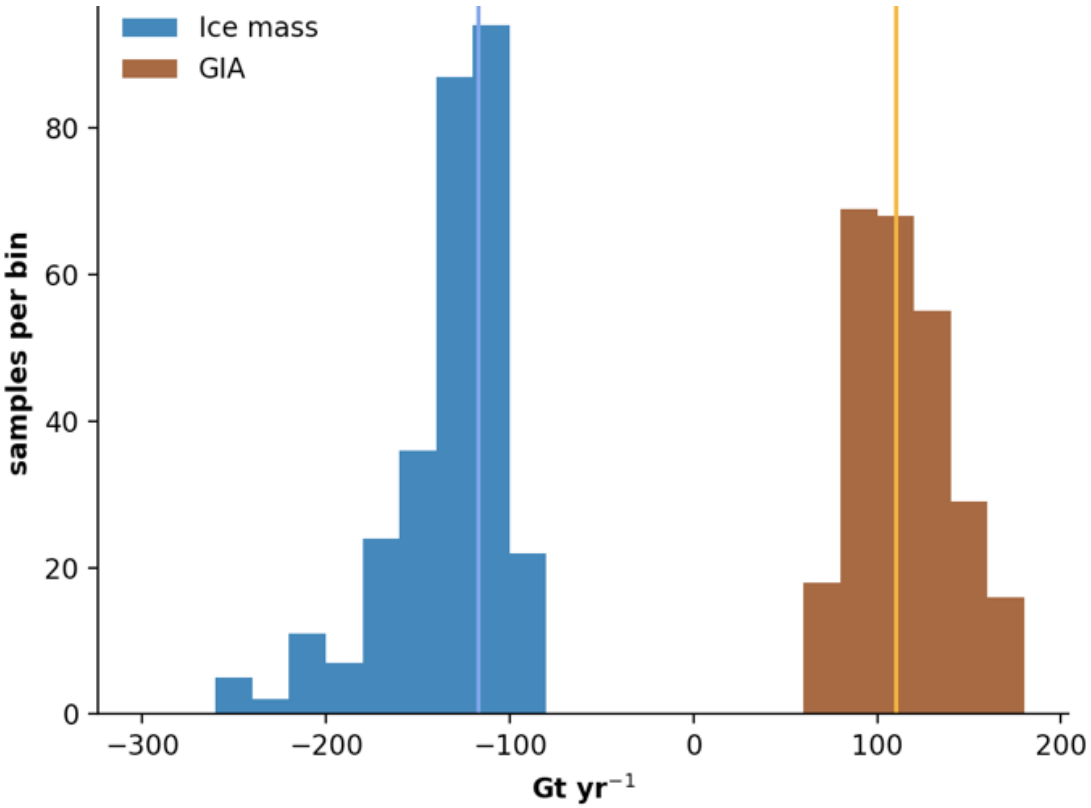

Figure 6.9: Histograms of posterior distributions for Antarctic Ice Sheet ice mass trend and GIA obtained from bootstrapping. Best-fit solutions are shown with vertical lines.

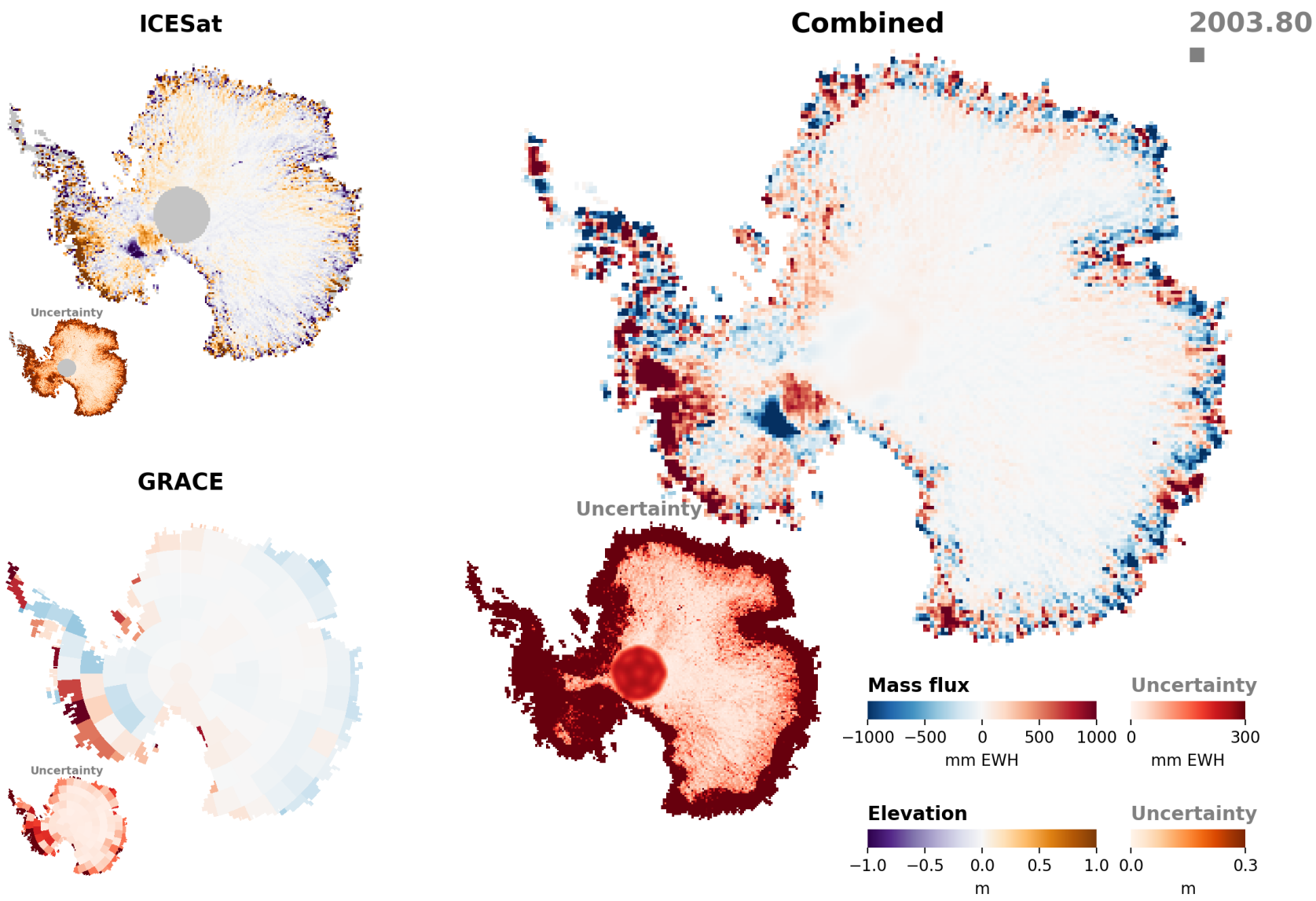

Figure 6.10: Time-variable mass variation solution for Laser 2A (late 2003), the which gives the best altimetry coverage over Antarctica in the 2003–2009 observation span

The recovered signal suffers from impulsive noise along other low-latitude coasts because of the gaps in the ICESat data. This noise is caused in part by ICEsat providing more spatial information in the north-south along-track direction than in the east-west crosstrack direction at low latitudes. This can lead to ringing and other artifacts when combined with smooth GRACE data. This type of noise may be mitigated with a median filter in post-processing the output solutions or by using a different set of constraints for coastal sites. For instance, an anisotropic smoothing constraint with more reach in the east-west direction than the north-south direction may compensate for the difference between along-track and cross-track resolution in ICESat data. Altimetry quality also degrades near the coast because of increased slopes and topographic roughness. These slope-induced errors can introduce appreciable noise, even between closely overlapping altimetry footprints. As may be expected from, ICESat exhibits noisier performance over the rugged topography of the Trans-Antarctic Mountains.

The worst case is embodied by Laser 2F, the last available observation cycle (Figure 6.11). Only 52% of the ground was covered by altimetry at 27 km resolution with signals being concentrated inland. Despite the high density of shots inland, the solution also suffers from isolated ringing artifacts from outlier altimetry inputs and zones of missing data. This solution fails to resolve Antarctic Peninsula signals better than GRACE. Mass loss near Totten is notably indistinct amid the coastal noise.

However, this cycle also demonstrates one of the chief benefits of data combination: filling gaps in altimetry coverage. In spite of missing data over the Kamb ice stream, the solution successfully reconstructs the shape of the ice mass gain signals at high resolution with only hints from low-resolution GRACE data and surrounding high-resolution altimetry. The solution also properly allocates long-wavelength signal to the outlet glaciers in West Antarctica, but does not resolve their shapes well.

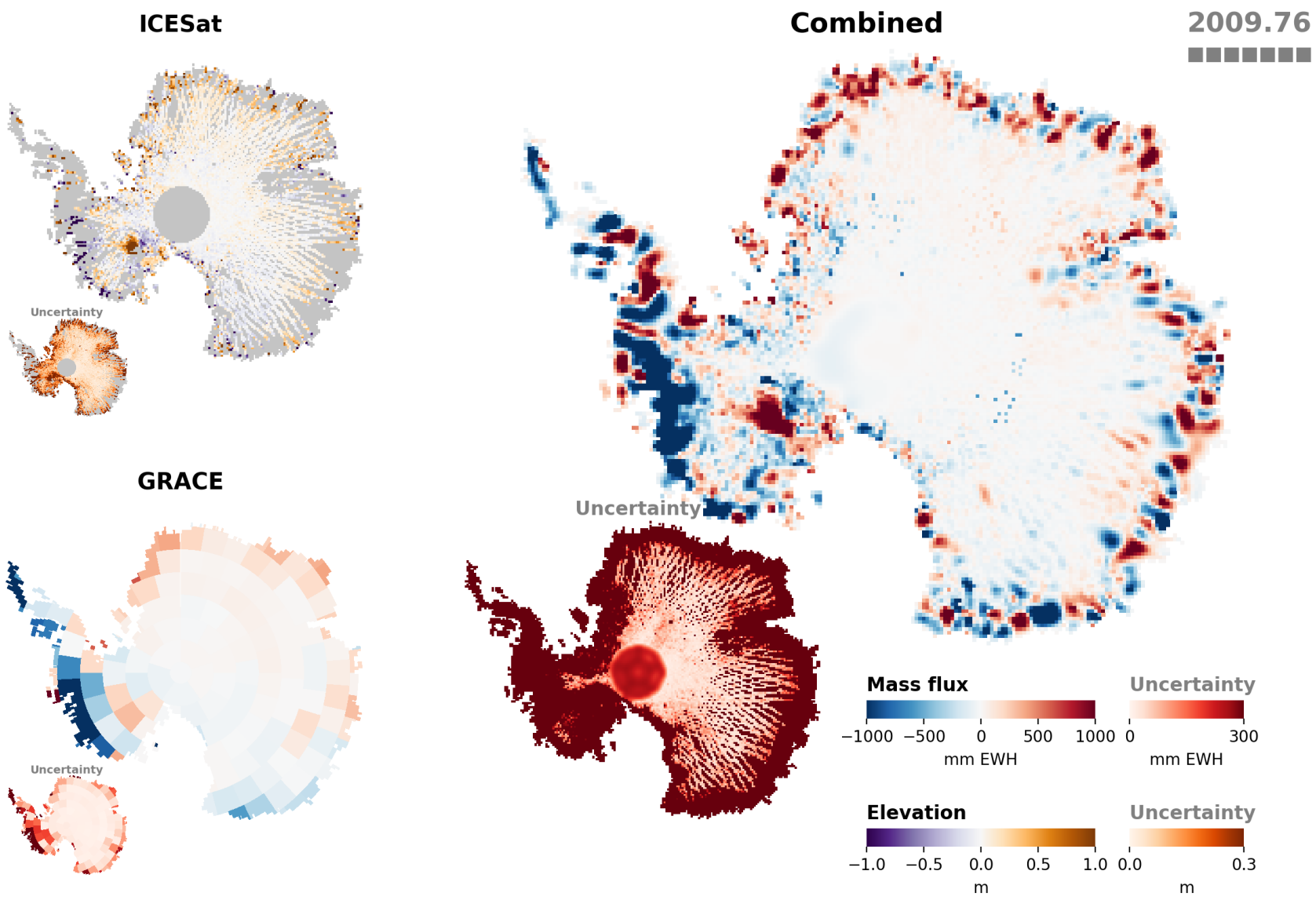

Figure 6.11: Time-variable mass variation solution for Laser 2F (late 2003), the which gives the worst altimetry coverage over Antarctica in the 2003–2009 observation span

The solutions may be integrated over East Antarctica, West Antarctica, the Antarctic Peninsula, and the entire continent to form time series and trends.

The best-fit GIA solution is compared with three representative models (Whitehouse et al. (2012), Peltier et al. (2015), and the reference model by Caron et al. (2018)) in Figure 6.13. The total mass rate correction for the Antarctic ice sheet is compared with other GIA models in Figure 6.14, which shows that the solution is within the range of variation of other models.

The majority of the deviation of the total GIA solution from the reference model comes from East Antarctica. Using the posterior distribution to construct asymmetric confidence intervals, the total GIA signal over East Antarctica is 70 $^{+58}_{-24}$ Gt yr^{-1}, 26 Gt yr^{-1} higher than the 44 $\pm$ 50 Gt yr^{-1} indicated by the Caron et al. (2018) reference model. Independent verification of this apparent bedrock uplift due to GIA could be difficult due to the lack of available GPS sites. Pending the development of novel geodetic observation methods, bedrock motion under the High Antarctic Plateau is only practically observable through the combination of altimetry and gravity demonstrated here.

The deviation of the GIA solution from the Caron et al. (2018) reference model is most intense over Ellsworth Land, where predicted uplift rates approach 1 cm yr^{-1}. The integrated mass change over all of West Antarctica, however only deviates from the reference model by 7 Gt yr^{-1} for a total mass rate of 32 $^{+2}_{-4}$ Gt yr^{-1}. The GIA model does not deviate from the predictions of Caron et al. (2018) significantly over the Antarctic Peninsula.

The GIA solution may be compared with GPS rates published by Martín-Español et al. (2016a). After using the JPL RL05.1M CRI-filtered mascons to remove elastic loading between 2009 and 2016, the residual observed mass trends are compared with predictions from the solution GIA model. A cluster of nine stations on the Antarctic Peninsula were removed from the analysis because of inadequate knowledge of mantle structure in that region. On the Amundsen Coast, data from the stations BERP and BACK were omitted because of concern with data quality and local environmental conditions. This comparison is shown in Figure 6.15.

At a glance, this comparison indicates that that the GIA model overestimated uplift in

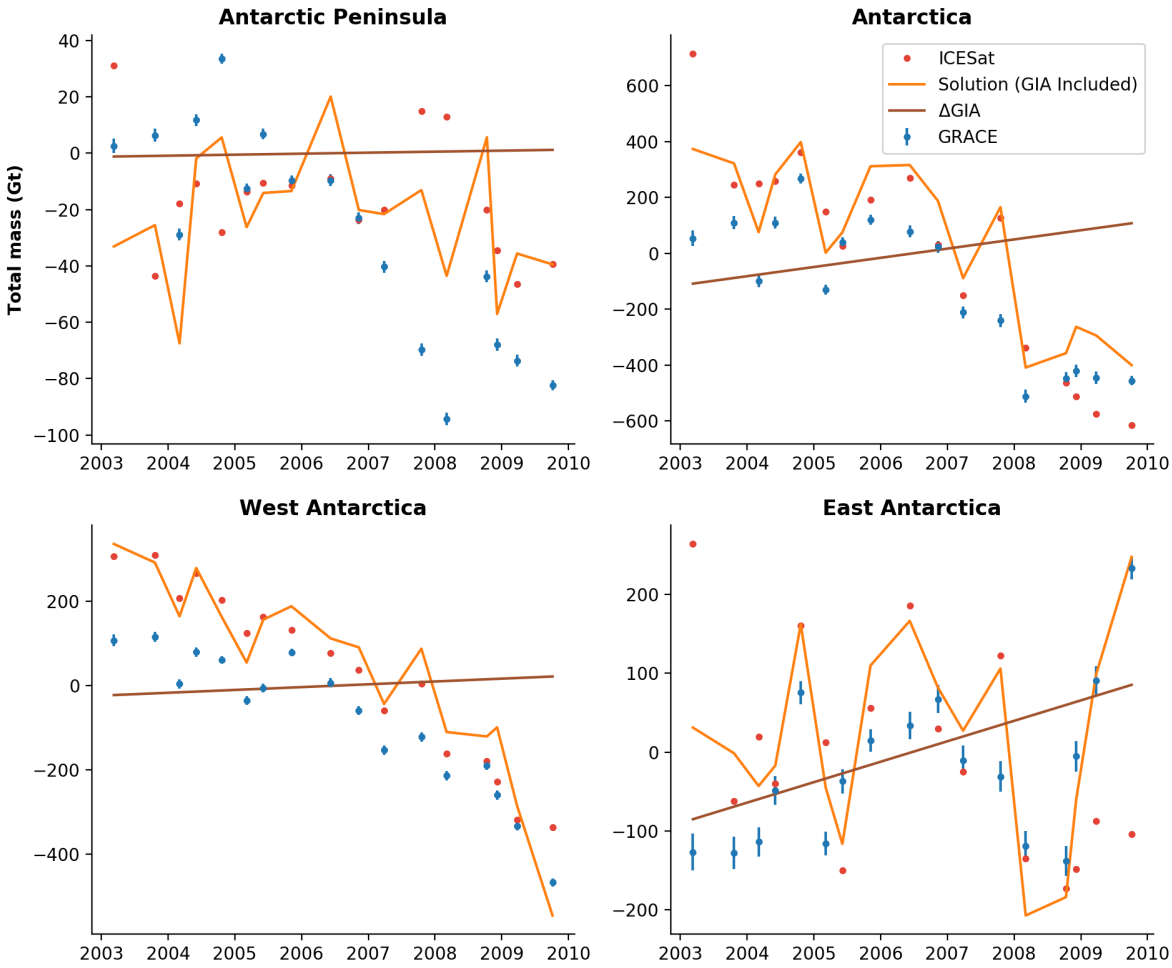

Figure 6.12: Time-variable combined mass variation solution for the major subdivisions of the Antarctic ice sheet compared with GRACE and ICESat input data

Mass Rate (Gt yr^{-1})		AIS	WAIS	EAIS	AP
GIA	This work	110^{+60}_{-24}	32^{+2}_{-4}	70^{+58}_{-24}	4^{+4}_{-4}
	Caron et al. (2018)	77 ± 71	25 ± 20	43 ± 50	2.7 ± 3.4
Ice Mass Trend	This work (2003–2009)	-116^{+10}_{-51}	-78^{+4}_{-11}	-21^{+24}_{-35}	-2^{+8}_{-6}
	IMBIE (2002–2007)	-73 ± 53	-65 ± 27	+12 ± 43	-20 ± 15

Table 6.2: Comparison of regional mass variation solutions with results from Caron et al. (2018) and Shepherd et al. (2018)

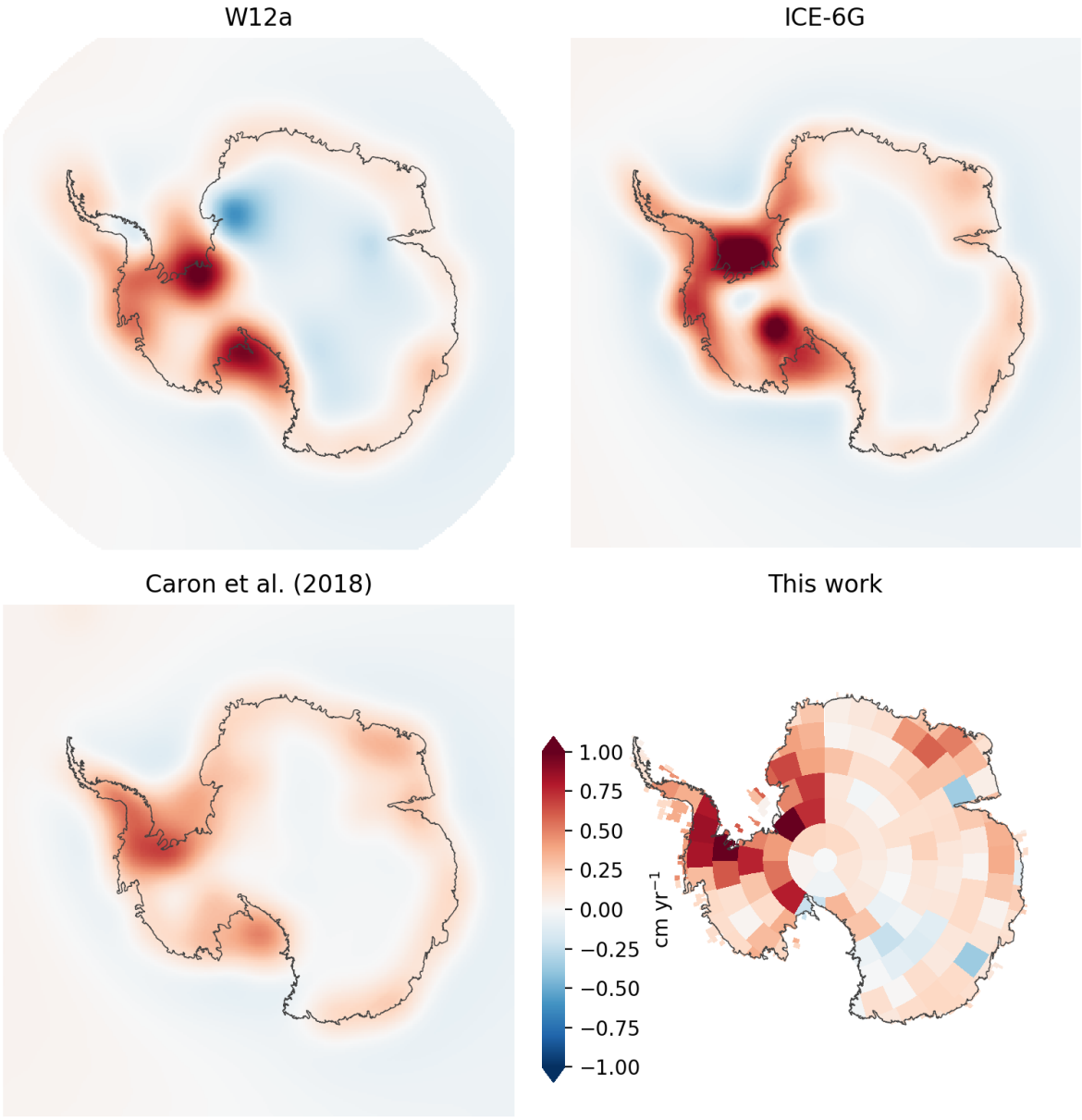

Figure 6.13: Best-fit GIA solution uplift rates from combining ICESat and GRACE (lower right) compared with three representative GIA models

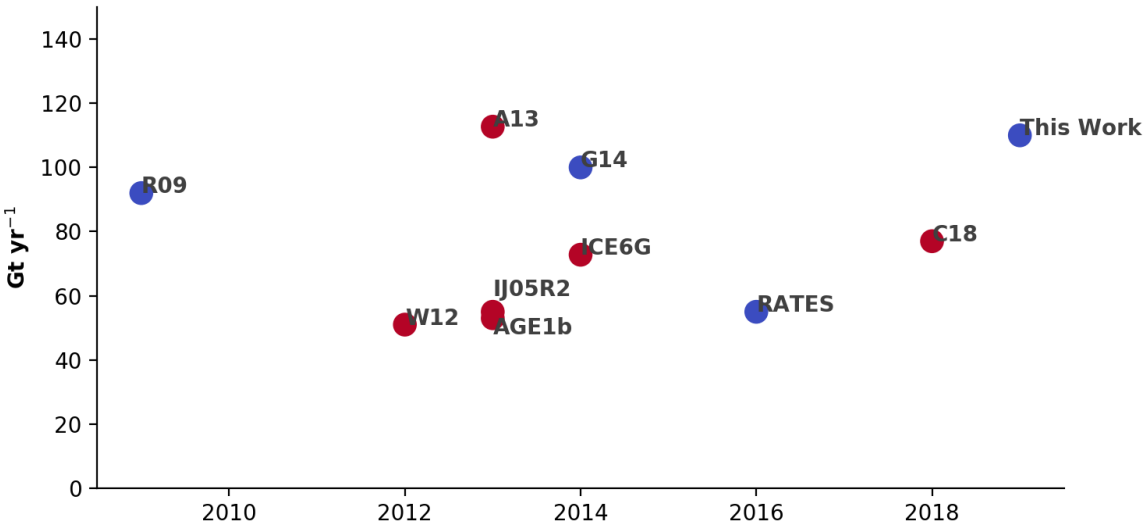

Figure 6.14: Comparison of GIA mass rates integrated over the Antarctic ice sheet after Martín-Español et al. (2016a)

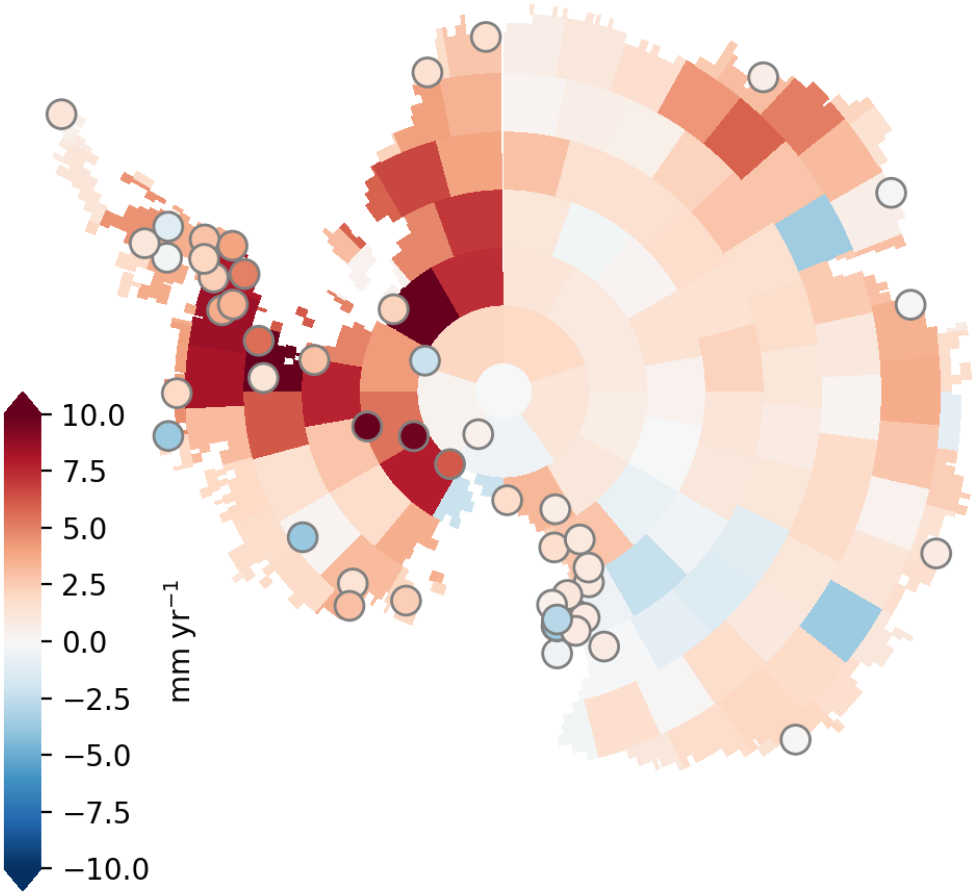

Figure 6.15: Comparison of the best-fit GIA model with GPS uplift rates

Std. Dev. Detrended Residuals (mm)	JPL Mascons	Combined Solution
Up	4.2	4.3
East	4.4	4.4
North	5.2	5.2

Table 6.3: Standard deviations of detrended residuals for UNR GPS positions positions predicted by GRACE and the combined solution within the 2003–2009 interval

Ellsworth Land. The model is otherwise consistent with uplift rate measurements across East Antarctica and the Trans-Antarctic Mountains. The weighted RMS error is computed using the inverse error variances as weights with distance-dependent tapering of the weights to diminish the effect of clusters of GPS stations. The weighted RMS of the residuals is 3.1 mm yr^{-1}. Other GIA models, including IJ05R2 (Ivins et al., 2013), AGE1b (Sasgen et al., 2013), and Gunter et al. (2014) have weighted RMS residuals of less than 2.0 mm yr^{-1}.

GPS time series may be used to validate the ice mass solution time series in principle. Examining the standard deviation of detrended residuals (SDDR) in three dimensions should enable quantification of solution quality independent of GIA and other trend signals. While Martín-Español et al. (2016a) only published GPS *trends*, the UNR daily GPS time series used in previous chapters may be used to compare time variations in bedrock deformation with model predictions. Unfortunately, this method is limited by the lack of GPS stations available in Antarctica prior to 2009. Outside of the cluster of stations in the vicinity of Ross Island, only seven sites are available for comparison with solutions over the 2003–2009 interval. Consequently, comparing the SDDR of the mascon-based solutions with GIA and elastic loading predictions from Caron et al. (2018) and the JPL RL05.1M mascons is inconclusive. Near-identical SDDR values are found for both mass variation solutions (Table 6.3).

The time series of solutions may be inspected basin-by-basin and compared with GRACE mass measurements integrated within their bounds (Figure 6.16). Basins 1, 13, 14, 17, 18, 20, 21, and 22 account for more than 80% of the variance of the total mass of the continent in this time span. Basin 1 exhibits a substantial GIA correction. There is a constant bias in the solution time series relative to GRACE solution. Mass loss on the Amundsen coast in basins 20, 21, and

22 is shown with a strong negative trend in both the GRACE and combined solution time series. However, notably, the trends in basins 21 and 22 are magnified relative to the low-resolution GRACE solution. This reflects high-resolution ICESat data aiding the restoration of mass loss signals that leak across basin boundaries in the GRACE data. This effect is most notable in the narrow boundaries of basin 18, which contains the Kamb Ice Stream. The trend measured by GRACE within the basin is magnified by a factor of two as additional spatial information from ICESat corrects for leakage. Within the larger basins 13 and 14, where leakage is less important, there is broad agreement with GRACE and important mass loss signals and events are captured.

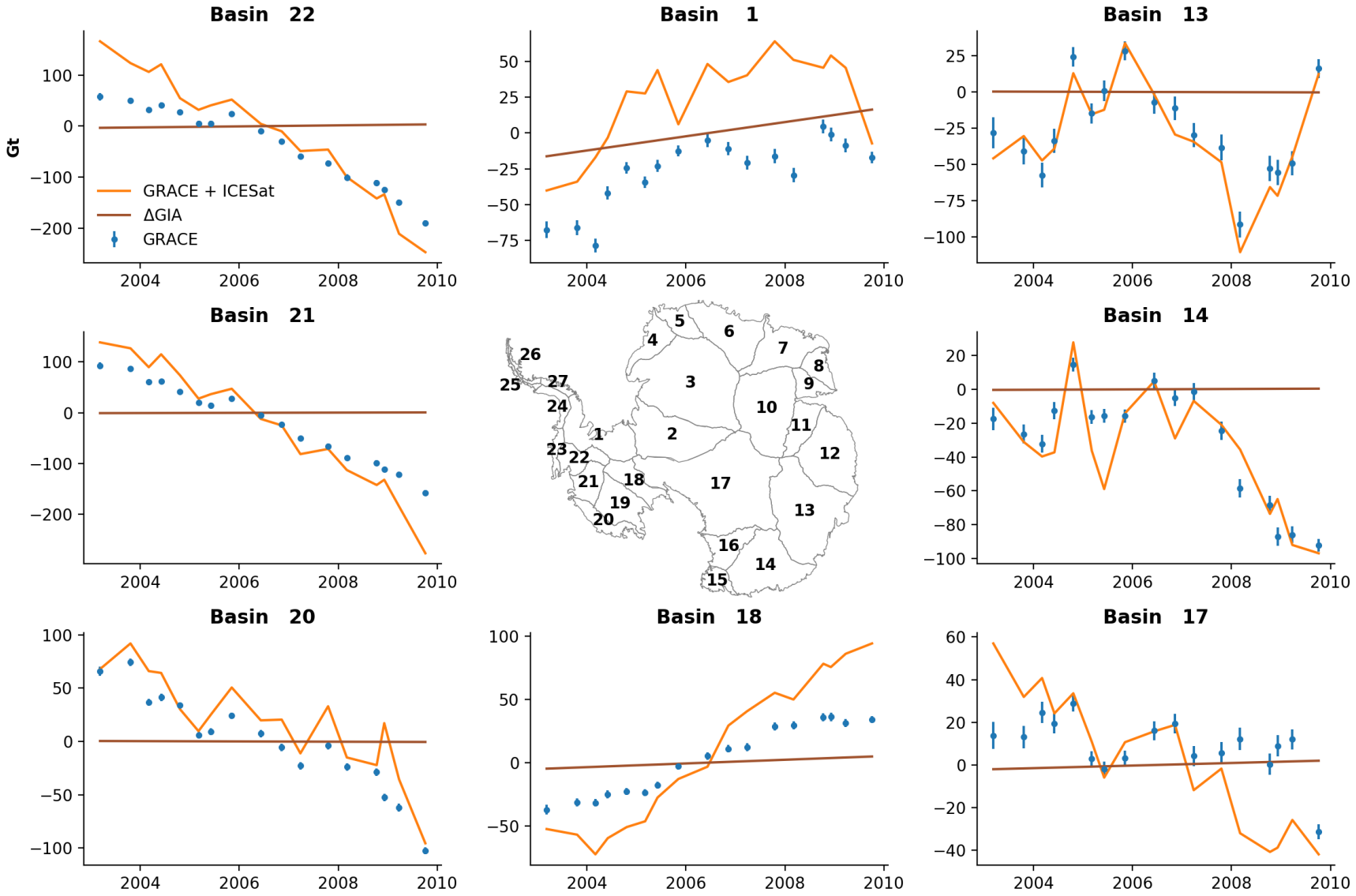

Figure 6.16: Time-variable combined mass variation solution for the eight most variable basins the Antarctic ice sheet compared with GRACE input data

6.3.1 Resolution

The chief motivation for combining ICESat and GRACE is enhanced spatial resolution. Verifying that the combination of these two datasets yields greater spatial resolution requires multiple methods of quantification.

In imaging, spatial resolution is defined system's ability to distinguish lines of a particular spacing. Resolution is represented by a modulation transfer function, which describes the imagine system's impulse response as a function of spatial frequency. The modulation transfer function is obtained by computing the spectral coherence of an image relative to the structure of the original source.

A simpler, more intuitive approach to quantifying resolution involves visualizing the modulation transfer function in terms of how the observation system modulates Fourier kernels of a particular frequency. This is similar to checkerboard tests performed in seismic tomography and GPS elastic loading inversion.

The first step in resolution quantification is construction of the "resolution matrix" which is the product of the observation system pseudoinverse and the observation operator. The resolution matrix is a square matrix that relates a set of parameters to the solution generated from the solution of a system of observation equations. It describes impulse response of the observation system. The diagonal elements of the resolution matrix lie between 0 and 1. The closer a diagonal element is to 1, the more well-resolved a parameter may be understood to be. The spatial resolution is reflected in the dispersion of the off-diagonal elements in each row with distance, indicating the degree of confusion in the solution.

For each cycle, the resolution matrix is computed from the information matrix obtained from altimetry and gravity. The effects of GIA are neglected and the final calculation of the resolution matrix at each cycle takes the form:

$$R = [A^T W_{A,i} A + M^T W_{M,i} M + \bar{P}^{-1}]^{-1} [A^T W_{A,i} A + M^T W_{M,i} M]. \tag{6.17}$$

	Altimetry Coverage	<27 km resolution	<100 km resolution	>100 km resolution
Best case (Laser 2A)	90%	86%	94%	6 %
Worst case (Laser 2F)	53%	52%	85%	15 %

Table 6.4: Antarctic ice sheet altimetry coverage and resolving widths for resolution thresholds of better than the native grid resolution of 27 km, better than 100 km, and worse than 100 km

The calculation of the resolution matrix includes the smoothing covariance $\bar{P}$.

Michelini and McEvilly (1991) devised a compact metric to summarize spatial resolution for a given point in the solution vector. The rows of R may be used to compute the resolving width s_j for the corresponding mass solution vector at index j.

$$s_j = |R_j|^{-1} \sum_{k=1}^{N} \left(\frac{R_{kj}}{|R_j|} \right)^2 d_{jk}, \tag{6.18}$$

where d_{jk} corresponds to the distance matrix for the locations of each point in the vector $\mathbf{m}$. This metric uses the resolution matrix rows as weights to compute the average information dispersion distance from a solution location.

We compute the resolution matrix and resolving width for the best (Laser 2A, 2003, 90% altimetry coverage) and worst (Laser 2F, 2009, 53% altimetry coverage) ICESat epochs allowed by the model. These results are shown in Table 6.4 In the best-case epoch, a resolution of 27 km is achieved over 86% of the continent. A further 8% of the continent is resolvable to better than 100 km. In total, 97% of the continent is resolvable to better-than-GRACE resolution of 330 km. The chief deficiencies in resolution occur near the coast and are especially pronounced on the northern reaches of the Antarctic peninsula. While the 4.8% of the continent below the 86 °S parallel is unobservable to altimetry, the combination of altimetry, GRACE, and elastic loading inversion enables the solution to resolve signals as far south as 87° S with an east-west resolution of ∼100 km.

The resolving width may be verified with a checkerboard test. For this test, we generate symmetric and continuous cosine checkerboard functions with half-wavelengths given in octaves

of grid resolution: 27 km, 54 km, 108 km, 216 km, and 432 km. The checkerboard vectors are multiplied by the resolution matrix to obtain a set of test solutions, the local coherence of which may be visually inspected to verify spatial resolution at each checkerboard scale. Both the resolving widths and checkerboard tests for the selected epochs are shown in Figure 6.17.

In the best-case epoch, the 27 km checkerboard is fully resolved in the solution region above 2000 m elevation and parts of the Rockefeller Plateau. The altimetry hole south of 86 °S remains unresolved. The 54 km checkerboard is well resolved over the majority of the continent, including Ellesmere Island, but is not resolved within 200 km of the coast or over the Kamb ice stream. The 108 km checkerboard is recovered everywhere, except within 50 km of a coast or in the 86 °S hole. Evidence of partial recovery of the checkerboard south of 86 °S. Little improvement in coherence is found on the Antarctic peninsula at coarser scales.

The worst-case epoch demonstrates adequate recovery of the 27 km checkerboard where altimetry is present. Most of the continent can be represented continuously at 108 km resolution, except within ∼200 km of the coast. The coast and Antarctic peninsula are poorly resolved even at half-wavelengths of 432 km.

The checkerboard test provides an optimistic upper limit on the spatial resolution of the combination. The ability to distinguish features will ultimately depend on the spatial distribution of the signal-to-noise ratio of the input data.

The spatial distribution of the SNR was examined by first computing the geometric mean of the ratio of the absolute value of solution signal to the standard deviation of the bootstrap ensemble members. This is shown in Figure 6.18. For more than 90% of the observable continent, the typical SNR is ∼1. The major exceptions are over Amundsen, Kamb, and Totten glaciers. Assuming that SNR improves with the square root of the number of grid cells included in an averaging window, then the smallest scale required to resolve a typical inland Antarctic mass change signal with 3-sigma certainty may be ∼100 km.

These tests enable the following generalization: For an ideal ICESat cycle with reliable firn corrections and little noise, over 85% of the continent may be resolved to 27 km or better. Coastal

locations or major ice streams may be resolved to ∼100 km. Locations on the Antarctic peninsula are resolvable to ∼100 km, but observing gaps may result in minimal resolution improvement over CRI-filtered mascons. Inspection of the SNR suggests that the effective spatial resolution of the solution is ∼100 km.

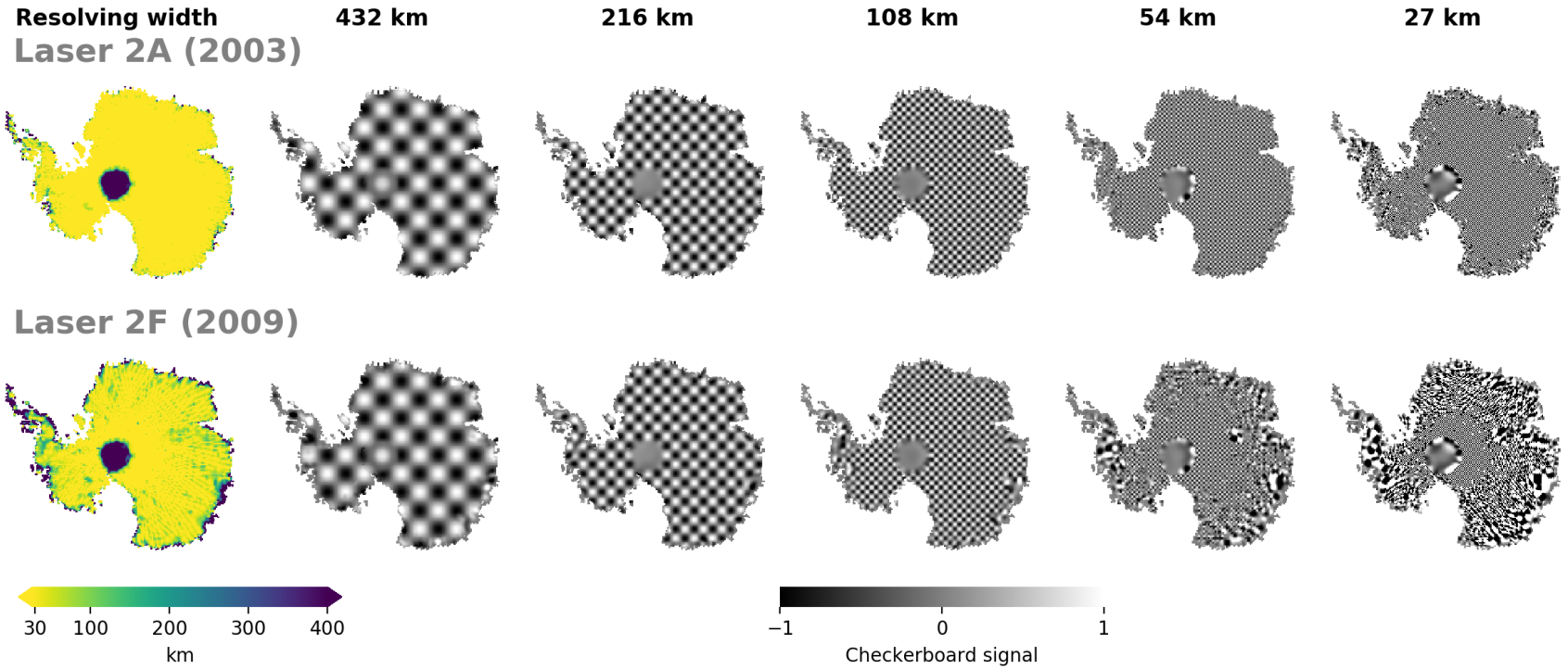

Figure 6.17: Resolving widths and checkerboard tests illustrating the effective spatial resolution and scale-dependent distortion of regular checkerboard patterns at various spatial resolutions

6.4 Discussion

This chapter details the generation of time-variable solutions for surface elevation change in Antarctica and the combination of these solutions with corresponding GRACE data to create high-resolution mass variation solutions.

The gridded, high-resolution time-variable altimetry product at the heart of this work is a novel contribution to the field. Most literature up to this point has focused on producing altimetry trends to assess mass trends within an interval. The altimetry product created to enable this combination is a unique and novel "frame-by-frame" examination of surface elevation variation in the Antarctic Ice Sheet. The spatial resolution of this product is currently 27 km, but maps of shot pair density and cycle availability (Figure 6.2) imply that solutions with grid resolutions as low as 2 km may be generated to examine elevation variations within regions. One such application of altimetry series is the investigation of subglacial lakes across the Antarctic Ice Sheet as performed by Smith et al. (2009) using ICESat data.

The availability of time-variable altimetry grids was an essential ingredient in producing cycle-by-cycle, high-resolution solutions for mass variation in Antarctica. The solutions generated in this chapter may also be used as training dataset to construct estimators to optimally relate low-resolution GRACE surface mass flux data to high-resolution. Such an estimator may be used to preserve temporal continuity for high-resolution spatial solutions in the event that ICESat-2 is temporarily unable to collect data during its coincident observing span with GRACE-FO.

A number of lessons resulted from this combination. First, even after correcting for firn air content, some firn air content signal is expected to remain in the data and the errors may be correlated with the signal. Considering the low signal-to-noise ratio of GRACE and ICESat over quiet parts of the ice sheet, a hybrid density model with fully compacted ice at low elevations and equilibrium firn density at high elevations may be necessary to properly combine these datasets. Variance-based weighting further mitigated the role of residual firn air content signal in the ICESat data in the combination. Weighting the data according to variance ensures that the mass time

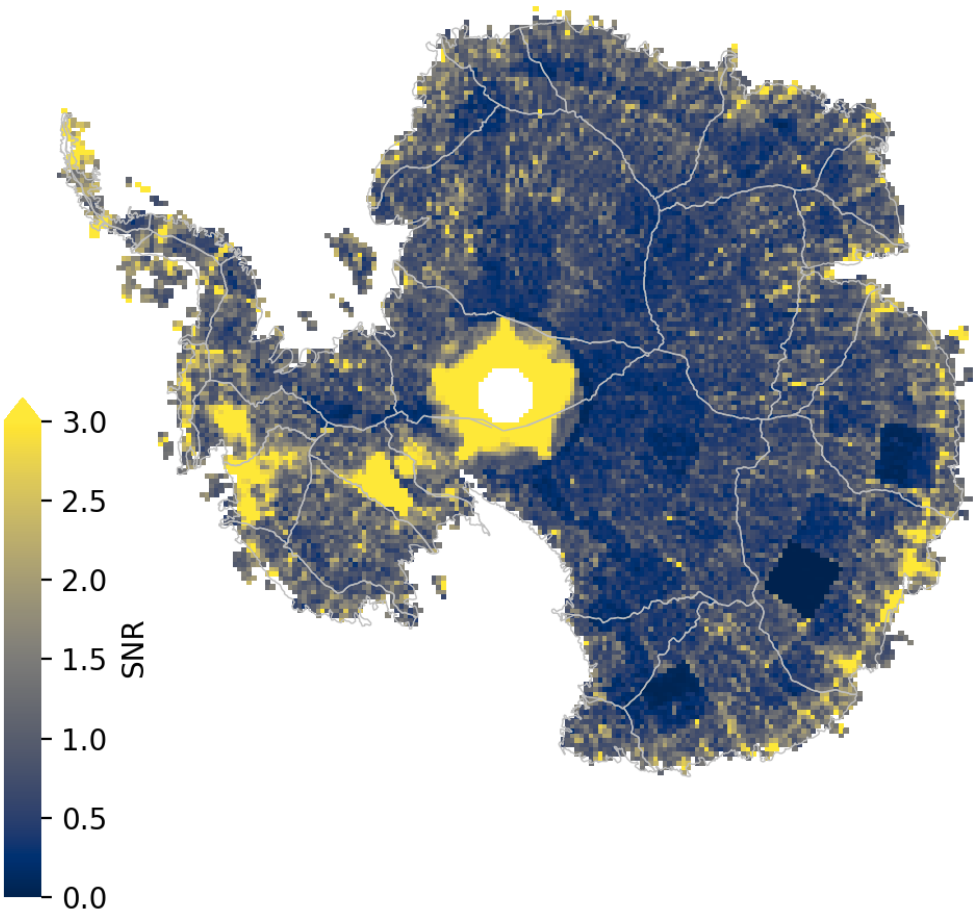

Figure 6.18: Signal-to-noise ratio of high-resolution mass variation solutions

series in the solution is maximally correlated with both the GRACE and ICESat input time series at a point by downweighting the ICESat data accordingly if it contains extraneous signals that aren't correlated with the corresponding with GRACE time series.

While few GPS observing sites are available for measurement of crustal deformation during the period of 2003–2009, trends obtained from GPS stations installed in later years may be used to constrain the time-independent GIA model outside of the data observing range. The inclusion of GPS trends from outside the observation period would be applicable to combination of data from GRACE-FO and ICESat-2 if these satellites outlive any of the current GPS observing sites.

ICESat's groundtrack may be poorly suited for observing elevation change over the Antarctic Peninsula. This results in poor resolution of mass change over this region in the combination of ICESat and GRACE. Other possible data sources, data editing rules, and and spatial constraints should be investigated to improve mass variation solutions near the coast. The addition of lower-inclination altimetry data, such as from CryoSat may stabilize this solution.

Sasgen et al. (2019) notably combine CryoSat altimetry data with GRACE data over the 2011–2017 interval to find a mass loss rate of 178 $\pm$ 23 Gt yr^{-1}. While these aren't directly comparable with our solutions over the 2003–2009 interval, the difference is partly attributable to the acceleration in mass loss of $\sim$15 Gt yr^{-2} over the 2002–2017 interval found by Shepherd et al. (2018). Their combination technique differs from this work in that it was performed in the spectral, rather than spatial domain. This enabled scale-dependent relative weighting of altimetry and GRACE, with altimetry being given more weight at spatial scales below 400 km. This work, by contrast, is a straightforward space-domain combination of low-resolution area averages with high-resolution point measurements.

Gao et al. (2019) recently performed another combination of GRACE with ICESat altimetry over 2003–2009, finding a mass loss signal of 84 $\pm$ 31 Gt yr^{-1} and a GIA correction of 55 $\pm$ 23 Gt yr^{-1}. While their mass loss estimate is consistent with this work within 1 σ, their GIA estimate is significantly smaller. Their GIA estimate is distinguished from this work in that it uses the more robust spherical-cap parameterization presented in Chapter 4 of this work. They also use variable

effective mantle densities, particularly over the Antarctic Peninsula.

Chapter 7

Conclusions

This project focused on combining GRACE, ICESat, and GNSS data to better resolve the sources of mass change in Antarctica. The primary objective is to implement a combination of geodetic observations of Antarctica to resolve variations in mass on monthly timescales. The combination should fulfill three criteria:

(1) Assimilate GNSS, altimetry, and gravimetry data into a model of mass variability in Antarctica

(2) Disaggregate sources of mass and elevation change including GIA, ice dynamics, surface mass balance, and firn compaction

(3) Increase spatial resolution of Antarctic mass transport relative to GRACE solutions at monthly timescales

The inputs, outputs, and timescales of each method are tabulated in Figure 7.1.

Because of the exploratory nature of this investigation, no single method presented in this work fulfills all of these goals. This is partly to enable independent validation of solutions and to reduce the complexity of the overall problem. Furthermore, no method disaggregates all Antarctic mass transport processes at once. Instead, GIA is separated from aggregated ice sheet processes in some methods. In solution methods seeking to disaggregate ice dynamics and surface mass balance or adjust the sum of their contributions, GIA is treated as an independent background model.

Finally, a number of these investigations were preformed at mascon-resolution or by operating on elevation and surface mass trends, not necessarily offering improvements on the spatial or temporal resolution of GRACE. The direct least-squares combination of ICESat and GRACE in Chapter 5 improves the spatial resolution of GRACE at the temporal resolution of ICESat.

Nonetheless, this investigation has resulted in the creation of an in-depth toolkit for understanding Antarctic mass variation with multiple geodetic datasets.

Atmospheric errors, a major error source in GRACE data were studied in depth on monthly timescales. In situ data, robust reanalyses, and optimal combinations of these models and data were used to validate the atmospheric component of the dealiasing model and produce corrections to GRACE solutions. These errors were found that to hide additional acceleration in mass loss on the order of 4 Gt yr^{-2}. This work also finds that the next generation of dealiasing models, AOD1B RL06, largely corrects these discrepancies by using the ERA-Interim surface pressure field as an input after 2006. However, the new dealiasing model still contains less robust operational atmospheric models prior to 2006 and thus still features their associated drifts. This work further demonstrates the presence of atmospheric error signals in GRACE data over the High Antarctic Plateau. Using these a method for recovery of atmospheric signals in quiet parts of Antarctica was developed, demonstrating the potential of GRACE as a meteorological observing tool.

These atmospheric errors and their corrections were used in preprocessing of data combination in Chapter 6. Over the 2003–2009 ICESat interval, where atmospheric errors are most extreme, these errors add a correction of 16 Gt yr^{-1} to the input GRACE data. This work highlights the importance of including atmospheric surface pressure corrections in analyses of GRACE data.

This investigation required the development of data products for ICESat elevation changes from overlapping footprints and elevation change grids by cycle. The resolution and effective revisit frequencies of locations in Antarctica over the 2003–2009 span were quantified. These time-variable grids for each cycle were used to produce estimates of effective surface density via least-squares comparison of mascon-averaged ICESat elevation grids.

This work developed a method for separation of ice sheet mass trend signals and GIA using GRACE data, GNSS data, and GIA ensembles. It also replicated the Gunter et al. (2014) method for separation of ice sheet mass trend signals and GIA using GIA ensembles and GNSS data. A method for separating ice dynamics and surface mass balance trend signals in mascons without necessarily increasing spatial resolution was explored.

Another part of this project focused on obtaining monthly solutions at high spatial resolution through the combination of GRACE, ICESat, surface mass balance models, and basin discharge measurements. The investigation of monthly combination first resulted in a method for estimating ice dynamics fields using ICESat fields and adjusting these fields with basin discharge estimates. This *a priori* ice dynamics model was combined with the RACMO surface mass balance model and low-resolution GRACE data to obtain high-resolution mass change solutions. The elastic loading predictions from these solution methods were demonstrated to be consistent with in independent GNSS position time series.

Finally, the work culminated in the direct, least-squares combination of GRACE and ICESat at the temporal and spatial resolution of ICESat. It required the creation of a unique, time-variable elevation data product created by locating overlapping footprints across different ICESat cycles and inverting these elevation differences to create time series of elevation change. These time series were combined with low-resolution mascon solutions from GRACE to simultaneously produce 17 high-resolution slices of Antarctic mass balance in time and a low-resolution, time-independent solution for GIA. This work revealed the challenges of combining fundamentally different measurement types at these temporal and spatial scales. It resulted in an estimate for total mass change in the 2003–2009 interval of -116^{+10}_{-51} Gt yr^{-1} and a GIA estimate of 110^{+60}_{-24} Gt yr^{-1}. These estimates are broadly consistent with contemporary work within 1–2σ.

7.1 Future work

It is desirable to unify the analysis techniques described in this work into a single filter that accomplishes all of the stated project goals. This work produced time-variable maps of ICESat

		Inputs					Modeled Processes					
	Filter Description	**GRACE**	**ICESat**	**GNSS**	**RACMO**	**Basin Discharge**	**Atmospheric Errors**	**Surface Mass Balance**	**Ice Dynamics**	**Firn Compaction**	**GIA**	**Timescale**
Chapter 3	**Atmospheric Errors**	•			•		•					Monthly
Chapter 4	**GNSS + GRACE**	•		•					•		•	Trend
	ICESat + GRACE	•	•						•		•	Trend
	ICESat/GRACE Regression	•	•							•		Constant
	Source Separation	•			•			•	•			Trend
Chapter 5	**Ice Dynamics Adjustment**		•		•	•			•			Monthly
	Fixed-gain Kalman Filter	•	•		•				•			Monthly
	Conventional Kalman Filter	•	•		•	•			•			Monthly
Chapter 6	**Least-Squares Combination**	•	•						•		•	Cycle

Figure 7.1: Summary of input data, modeled output processes, and data timescales for all solution methods explored in this work

elevation grids at the timescale of the iciest cycle (2-3 times per year over a typical 33-day span), but these were not ingested into the monthly solutions. The cycle-based solutions may be used to estimate ice dynamics priors and covariances instead of using average trends. Firn air content could be modeled using spatial constraints from existing models rather than being treated as a background model. GNSS solutions could also be included with future solutions rather than set aside for validation.

The methods developed for this work can benefit regions where changes in ice mass occur on smaller scales than GRACE can resolve. The Gulf of Alaska contributed 75 $\pm$ 11 Gt yr^{-1} to current sea level rise between 1994 and 2013 (Larsen et al., 2015). Because Alaskan ice mass loss can locally create geoid changes in excess of 1 cm per decade, high-resolution modeling of these signals may prove essential to maintaining an accurate geoid-based height system (Jacob et al., 2011). Iceland's major ice caps are individually much smaller than a single mascon, but local crustal deformation caused by these processes are observable by InSAR and surrounding GNSS sites, which capture both elastic loading from the ice caps and the unique GIA signals associated with recent deglaciation (Auriac et al., 2013).

As the three major datasets used in this work represent the major types of geodetic observations in Antarctica, the mathematical and computational infrastructure used to solve this problem could, in principle, accommodate other time-variable geodetic datasets. More importantly, the accuracy of this solution should be evaluated using data outside of the core triad of GRACE, ICESat, and GNSS data.

Radar altimetry data present the most immediate additional information due to their broad coverage in both space and time. CryoSat-2, launched in 2010, extends the record of Antarctic surface elevation change to the present day. Helm et al. (2014), for example, use CryoSat-2 data to measure the loss of -128 $\pm$ 83 km^3 yr^{-1} of Antarctic ice sheet volume between 2011 and 2014. Envisat radar altimetry is available between 2002 and 2012, with considerable temporal overlap between ICESat data. Envisat orbits at a somewhat lower inclination than ICESat, and is therefore only able to provide data from as far south as 81.6° S compared with ICESat's 86.0° S. Nonetheless,

the data provided by the Envisat mission have been used to establish elevation change rates over Antarctica (Flament and Rémy, 2012).

Airborne laser altimetry from Operation IceBridge (Koenig et al., 2010) is designed to supplement ICESat altimetry. While IceBridge flight lines often capture much smaller spatial scales than the proposed solution scales, these flights are often designed to follow prior ICESat groundtracks and frequently target regions where elevation change is expected.

7.2 Final Remarks

As stated at the beginning of this work, measuring mass transport on Earth's surface is a top priority for Earth science in coming years. At the time of this writing, GRACE-FO and ICESat-2 are in orbit collecting and will soon return science data products to extend the record of mass change in Antarctica. The techniques demonstrated in this work pave the way toward robust simultaneous combinations of these data and will enable refinement of the community's understanding Antarctica's present contributions to sea level rise and the role Antarctica will play in future sea level. The higher resolution afforded by the techniques developed here will sharpen understanding of mass transport processes in Antarctica. The unique altimetry and surface mass change products developed in Chapter 6 will allow researchers to examine cumulative mass balance in Antarctica on a cycle-by-cycle basis rather than through averaged trends. They will be of benefit to modelers of both the Antarctic ice sheet and solid-Earth processes like GIA. Furthermore, the techniques demonstrated here are applicable to ice mass changes in other parts of the world.

The combination techniques presented here and their output products open new avenues for Antarctic science.

Bibliography

A, G., Wahr, J., and Zhong, S. (2013). Computations of the viscoelastic response of a 3-d compressible earth to surface loading: an application to glacial isostatic adjustment in antarctica and canada. Geophysical Journal International, 192(2):557–572.

Argus, D. F., Fu, Y., and Landerer, F. W. (2014). Seasonal variation in total water storage in california inferred from GPS observations of vertical land motion. Geophysical Research Letters, 41(6):1971–1980.

Auriac, A., Spaans, K. H., Sigmundsson, F., Hooper, A., Schmidt, P., and Lund, B. (2013). Iceland rising: Solid earth response to ice retreat inferred from satellite radar interferometry and visocelastic modeling. Journal of Geophysical Research: Solid Earth, 118(4):1331–1344.

Barletta, V. R., Bevis, M., Smith, B. E., Wilson, T., Brown, A., Bordoni, A., Willis, M., Khan, S. A., Rovira-Navarro, M., Dalziel, I., Smalley, R., Kendrick, E., Konfal, S., Caccamise, D. J., Aster, R. C., Nyblade, A., and Wiens, D. A. (2018). Observed rapid bedrock uplift in amundsen sea embayment promotes ice-sheet stability. Science, 360(6395):1335–1339.

Blewitt, G., Hammond, W., and Kreemer, C. (2018). Harnessing the GPS data explosion for interdisciplinary science. Eos, 99.

Caron, L., Ivins, E. R., Larour, E., Adhikari, S., Nilsson, J., and Blewitt, G. (2018). GIA model statistics for GRACE hydrology, cryosphere, and ocean science. Geophysical Research Letters, 45(5):2203–2212.

Church, J., Clark, P., Cazenave, A., Gregory, J., Jevrejeva, S., Levermann, A., Merrifield, M., Milne, G., Nerem, R., Nunn, P., Payne, A., Pfeffer, W., Stammer, D., and Unnikrishnan, A. (2013). Sea Level Change. Cambridge University Press, Cambridge, United Kingdom and New York, NY, USA.

Dee, D. P., Uppala, S. M., Simmons, A. J., Berrisford, P., Poli, P., Kobayashi, S., Andrae, U., Balmaseda, M. A., Balsamo, G., Bauer, P., Bechtold, P., Beljaars, A. C. M., van de Berg, L., Bidlot, J., Bormann, N., Delsol, C., Dragani, R., Fuentes, M., Geer, A. J., Haimberger, L., Healy, S. B., Hersbach, H., Hólm, E. V., Isaksen, L., Kållberg, P., Köhler, M., Matricardi, M., McNally, A. P., Monge-Sanz, B. M., Morcrette, J.-J., Park, B.-K., Peubey, C., de Rosnay, P., Tavolato, C., Thépaut, J.-N., and Vitart, F. (2011). The ERA-interim reanalysis: configuration and performance of the data assimilation system. Quarterly Journal of the Royal Meteorological Society, 137(656):553–597.

Dobslaw, H., Bergmann-Wolf, I., Dill, R., Poropat, L., Thomas, M., Dahle, C., Esselborn, S., Knig, R., and Flechtner, F. (2017). A new high-resolution model of non-tidal atmosphere and ocean mass variability for de-aliasing of satellite gravity observations: Aod1b rl06. Geophysical Journal International, submitted.

Farrell, W. E. (1972). Deformation of the earth by surface loads. Rev. Geophys., 10(3):761.

Felikson, D., Urban, T. J., Gunter, B. C., Pie, N., Pritchard, H. D., Harpold, R., and Schutz, B. E. (2017). Comparison of elevation change detection methods from ICESat altimetry over the greenland ice sheet. IEEE Transactions on Geoscience and Remote Sensing, 55(10):5494–5505.

Flament, T. and Rémy, F. (2012). Dynamic thinning of antarctic glaciers from along-track repeat radar altimetry. Journal of Glaciology, 58(211):830–840.

Flechtner, F. (2007). Aod1b product description document for product releases 01 to 04 (rev. 3.1, april 13, 2007). GRACE project document, pages 327–750.

Fretwell, P., Pritchard, H. D., Vaughan, D. G., Bamber, J. L., Barrand, N. E., Bell, R., Bianchi, C., Bingham, R. G., Blankenship, D. D., Casassa, G., Catania, G., Callens, D., Conway, H., Cook, A. J., Corr, H. F. J., Damaske, D., Damm, V., Ferraccioli, F., Forsberg, R., Fujita, S., Gim, Y., Gogineni, P., Griggs, J. A., Hindmarsh, R. C. A., Holmlund, P., Holt, J. W., Jacobel, R. W., Jenkins, A., Jokat, W., Jordan, T., King, E. C., Kohler, J., Krabill, W., Riger-Kusk, M., Langley, K. A., Leitchenkov, G., Leuschen, C., Luyendyk, B. P., Matsuoka, K., Mouginot, J., Nitsche, F. O., Nogi, Y., Nost, O. A., Popov, S. V., Rignot, E., Rippin, D. M., Rivera, A., Roberts, J., Ross, N., Siegert, M. J., Smith, A. M., Steinhage, D., Studinger, M., Sun, B., Tinto, B. K., Welch, B. C., Wilson, D., Young, D. A., Xiangbin, C., and Zirizzotti, A. (2013). Bedmap2: improved ice bed, surface and thickness datasets for antarctica. The Cryosphere, 7(1):375–393.

Gao, C., Lu, Y., Zhang, Z., and Shi, H. (2019). A joint inversion estimate of antarctic ice sheet mass balance using multi-geodetic data sets. Remote Sensing, 11(6):653.

Gardner, A. S., Moholdt, G., Scambos, T., Fahnstock, M., Ligtenberg, S., van den Broeke, M., and Nilsson, J. (2018). Increased west antarctic and unchanged east antarctic ice discharge over the last 7 years. The Cryosphere, 12(2):521–547.

Gaspari, G. and Cohn, S. E. (1999). Construction of correlation functions in two and three dimensions. Quarterly Journal of the Royal Meteorological Society, 125(554):723–757.

Gunter, B. C., Didova, O., Riva, R. E. M., Ligtenberg, S. R. M., Lenaerts, J. T. M., King, M. A., van den Broeke, M. R., and Urban, T. (2014). Empirical estimation of present-day antarctic glacial isostatic adjustment and ice mass change. The Cryosphere, 8(2):743–760.

Hardy, R. A., Nerem, R. S., and Wiese, D. N. (2017). The impact of atmospheric modeling errors on GRACE estimates of mass loss in greenland and antarctica. Journal of Geophysical Research: Solid Earth, 122(12):10,440–10,458.

Harig, C. and Simons, F. J. (2012). Mapping greenland's mass loss in space and time. Proceedings of the National Academy of Sciences, 109(49):19934–19937.

Helm, V., Humbert, A., and Miller, H. (2014). Elevation and elevation change of greenland and antarctica derived from CryoSat-2. The Cryosphere, 8(4):1539–1559.

Ivins, E. R., James, T. S., Wahr, J., Schrama, E. J. O., Landerer, F. W., and Simon, K. M. (2013). Antarctic contribution to sea level rise observed by GRACE with improved GIA correction. J. Geophys. Res. Solid Earth, 118(6):3126–3141.

Jacob, T., Wahr, J., Gross, R., Swenson, S., and A, G. (2011). Estimating geoid height change in north america: past, present and future. Journal of Geodesy, 86(5):337–358.

Kanamitsu, M., Ebisuzaki, W., Woollen, J., Yang, S.-K., Hnilo, J. J., Fiorino, M., and Potter, G. L. (2002). NCEP–DOE AMIP-II reanalysis (r-2). Bull. Amer. Meteor. Soc., 83(11):1631–1643.

Kaspers, K. A., van de Wal, R. S. W., van den Broeke, M. R., Schwander, J., van Lipzig, N. P. M., and Brenninkmeijer, C. A. M. (2004). Model calculations of the age of firn air across the antarctic continent. Atmospheric Chemistry and Physics, 4(5):1365–1380.

Kaula, W. M. (1966). Theory of satellite geodesy. Applications of satellites to geodesy. Dover.

Kim, B.-H., Eom, J., Seo, K.-W., and Wilson, C. R. (2016). Spurious barometric pressure acceleration in antarctica and propagation into GRACE antarctic mass change estimates. Geophys. J. Int., 206(2):1306–1314.

Kobayashi, S., OTA, Y., Harada, Y., Ebita, A., Moriya, M., Onoda, H., Onogi, K., Kamahori, H., Kobayashi, C., Endo, H., Miyaoka, K., and Takahashi, K. (2015). The JRA-55 reanalysis: General specifications and basic characteristics. Journal of the Meteorological Society of Japan, 93(1):5–48.

Koenig, L., Martin, S., Studinger, M., and Sonntag, J. (2010). Polar airborne observations fill gap in satellite data. Eos, Transactions American Geophysical Union, 91(38):333–334.

Larsen, C. F., Burgess, E., Arendt, A. A., O'Neel, S., Johnson, A. J., and Kienholz, C. (2015). Surface melt dominates alaska glacier mass balance. Geophysical Research Letters, 42(14):5902–5908.

Lazzara, M. A., Weidner, G. A., Keller, L. M., Thom, J. E., and Cassano, J. J. (2012). Antarctic automatic weather station program: 30 years of polar observation. Bull. Amer. Meteor. Soc., 93(10):1519–1537.

Lenaerts, J. T. M., van Meijgaard, E., van den Broeke, M. R., Ligtenberg, S. R. M., Horwath, M., and Isaksson, E. (2013). Recent snowfall anomalies in dronning maud land, east antarctica, in a historical and future climate perspective. Geophysical Research Letters, 40(11):2684–2688.

Ligtenberg, S. R. M., Helsen, M. M., and van den Broeke, M. R. (2011). An improved semi-empirical model for the densification of antarctic firn. The Cryosphere, 5(4):809–819.

Mandel, J. (2009). A Brief Tutorial on the Ensemble Kalman Filter. ArXiv e-prints.

Mandel, K. and Agol, E. (2002). Analytic light curves for planetary transit searches. The Astrophysical Journal, 580(2):L171–L175.

Martín-Español, A., King, M. A., Zammit-Mangion, A., Andrews, S. B., Moore, P., and Bamber, J. L. (2016a). An assessment of forward and inverse GIA solutions for antarctica. Journal of Geophysical Research: Solid Earth, 121(9):6947–6965.

Martín-Español, A., Zammit-Mangion, A., Clarke, P. J., Flament, T., Helm, V., King, M. A., Luthcke, S. B., Petrie, E., Rémy, F., Schn, N., Wouters, B., and Bamber, J. L. (2016b). Spatial and temporal antarctic ice sheet mass trends, glacio-isostatic adjustment, and surface processes from a joint inversion of satellite altimeter, gravity, and GPS data. Journal of Geophysical Research: Earth Surface, 121(2):182–200.

Michelini, A. and McEvilly, T. (1991). Seismological studies at parkfield. i. simultaneous inversion for velocity structure and hypocenters using cubic b-splines parameterization. Bulletin of the Seismological Society of America, 81(2):524–552.

Minasny, B., McBratney, A. B., and Walvoort, D. J. (2007). The variance quadtree algorithm: Use for spatial sampling design. Computers & Geosciences, 33(3):383–392.

Moritz, H. (1978). Least-squares collocation. Rev. Geophys., 16(3):421.

National Academies of Sciences, Engineering, and Medicine (2018). Thriving on Our Changing Planet: A Decadal Strategy for Earth Observation from Space. National Academies Press.

Peltier, W. R., Argus, D. F., and Drummond, R. (2015). Space geodesy constrains ice age terminal deglaciation: The global ICE-6g_c (VM5a) model. J. Geophys. Res. Solid Earth, 120(1):450–487.

Petrov, L. (2004). Study of the atmospheric pressure loading signal in very long baseline interferometry observations. Journal of Geophysical Research, 109(B3).

Press, W. H., Teukolsky, S. A., Vetterling, W. T., and Flannery, B. P. (2007). Numerical Recipes 3rd Edition: The Art of Scientific Computing. Cambridge University Press.

Purcell, A., Dehecq, A., Tregoning, P., Potter, E.-K., McClusky, S. C., and Lambeck, K. (2011). Relationship between glacial isostatic adjustment and gravity perturbations observed by GRACE. Geophys. Res. Lett., 38(18):n/a–n/a.

Purcell, A., Tregoning, P., and Dehecq, A. (2016). An assessment of theICE6g_c(VM5a)glacial isostatic adjustment model. J. Geophys. Res. Solid Earth, 121(5):3939–3950.

Rienecker, M. M., Suarez, M. J., Gelaro, R., Todling, R., Bacmeister, J., Liu, E., Bosilovich, M. G., Schubert, S. D., Takacs, L., Kim, G.-K., Bloom, S., Chen, J., Collins, D., Conaty, A., da Silva, A., Gu, W., Joiner, J., Koster, R. D., Lucchesi, R., Molod, A., Owens, T., Pawson, S., Pegion, P., Redder, C. R., Reichle, R., Robertson, F. R., Ruddick, A. G., Sienkiewicz, M., and Woollen, J. (2011). MERRA: NASA's modern-era retrospective analysis for research and applications. Journal of Climate, 24(14):3624–3648.

Rignot, E., Mouginot, J., and Scheuchl, B. (2011). Ice flow of the antarctic ice sheet. Science, 333(6048):1427–1430.

Riva, R. E. M., Gunter, B. C., Urban, T. J., Vermeersen, B. L. A., Lindenbergh, R. C., Helsen, M. M., Bamber, J. L., van de Wal, R. S. W., van den Broeke, M. R., and Schutz, B. E. (2009). Glacial Isostatic Adjustment over Antarctica from combined ICESat and GRACE satellite data. Earth and Planetary Science Letters, 288:516–523.

Sabadini, R. and Vermeersen, B. (2004). Global Dynamics of the Earth. Springer Netherlands.

Sasgen, I., Konrad, H., Helm, V., and Grosfeld, K. (2019). High-resolution mass trends of the antarctic ice sheet through a spectral combination of satellite gravimetry and radar altimetry observations. Remote Sensing, 11(2):144.

Sasgen, I., Konrad, H., Ivins, E. R., den Broeke, M. R. V., Bamber, J. L., Martinec, Z., and Klemann, V. (2013). Antarctic ice-mass balance 2003 to 2012: regional reanalysis of GRACE satellite gravimetry measurements with improved estimate of glacial-isostatic adjustment based on GPS uplift rates. The Cryosphere, 7(5):1499–1512.

Sasgen, I., Martín-Español, A., Horvath, A., Klemann, V., Petrie, E. J., Wouters, B., Horwath, M., Pail, R., Bamber, J. L., Clarke, P. J., Konrad, H., and Drinkwater, M. R. (2017). Joint inversion estimate of regional glacial isostatic adjustment in antarctica considering a lateral varying earth structure (ESA STSE project REGINA). Geophysical Journal International, 211(3):1534–1553.

Schoen, N., Zammit-Mangion, A., Rougier, J. C., Flament, T., Rémy, F., Luthcke, S., and Bamber, J. L. (2015). Simultaneous solution for mass trends on the west antarctic ice sheet. The Cryosphere, 9(2):805–819.

Seo, K.-W., Wilson, C. R., Scambos, T., Kim, B.-M., Waliser, D. E., Tian, B., Kim, B.-H., and Eom, J. (2015). Surface mass balance contributions to acceleration of antarctic ice mass loss during 2003-2013. J. Geophys. Res. Solid Earth, 120(5):3617–3627.

Shepherd, A., Ivins, E., Rignot, E., Smith, B., van den Broeke, M., Velicogna, I., Whitehouse, P., Briggs, K., Joughin, I., Krinner, G., Nowicki, S., Payne, T., Scambos, T., Schlegel, N., A, G., Agosta, C., Ahlstrm, A., Babonis, G., Barletta, V., Blazquez, A., Bonin, J., Csatho, B., Cullather, R., Felikson, D., Fettweis, X., Forsberg, R., Gallee, H., Gardner, A., Gilbert, L., Groh, A., Gunter, B., Hanna, E., Harig, C., Helm, V., Horvath, A., Horwath, M., Khan, S., Kjeldsen, K. K., Konrad, H., Langen, P., Lecavalier, B., Loomis, B., Luthcke, S., McMillan, M., Melini, D., Mernild, S., Mohajerani, Y., Moore, P., Mouginot, J., Moyano, G., Muir, A., Nagler, T., Nield, G., Nilsson, J., Noel, B., Otosaka, I., Pattle, M. E., Peltier, W. R., Pie, N., Rietbroek, R., Rott, H., Sandberg-Srensen, L., Sasgen, I., Save, H., Scheuchl, B., Schrama, E., Schrder, L., Seo, K.-W., Simonsen, S., Slater, T., Spada, G., Sutterley, T., Talpe, M., Tarasov, L., van de Berg, W. J., van der Wal, W., van Wessem, M., Vishwakarma, B. D., and Wouters, D. W. . B. (2018). Mass balance of the antarctic ice sheet from 1992 to 2017. Nature, 558(7709):219–222.

Smith, B. E., Fricker, H. A., Joughin, I. R., and Tulaczyk, S. (2009). An inventory of active subglacial lakes in antarctica detected by ICESat (2003–2008). Journal of Glaciology, 55(192):573–595.

Swenson, S. and Wahr, J. (2002). Methods for inferring regional surface-mass anomalies from gravity recovery and climate experiment (GRACE) measurements of time-variable gravity. Journal of Geophysical Research: Solid Earth, 107(B9):ETG 3–1–ETG 3–13.

Turner, J., Colwell, S. R., Marshall, G. J., Lachlan-Cope, T. A., Carleton, A. M., Jones, P. D., Lagun, V., Reid, P. A., and Iagovkina, S. (2004). The SCAR READER project: Toward a high-quality database of mean antarctic meteorological observations. Journal of Climate, 17(14):2890–2898.

Velicogna, I., Sutterley, T. C., and van den Broeke, M. R. (2014). Regional acceleration in ice mass loss from greenland and antarctica using GRACE time-variable gravity data. Geophys. Res. Lett., 41(22):8130–8137.

Wahr, J., DaZhong, H., and Trupin, A. (1995). Predictions of vertical uplift caused by changing polar ice volumes on a viscoelastic earth. Geophysical Research Letters, 22(8):977–980.

Wahr, J., Khan, S. A., van Dam, T., Liu, L., van Angelen, J. H., van den Broeke, M. R., and Meertens, C. M. (2013). The use of GPS horizontals for loading studies, with applications to northern california and southeast greenland. Journal of Geophysical Research: Solid Earth, 118(4):1795–1806.

Wahr, J., Molenaar, M., and Bryan, F. (1998). Time variability of the earth's gravity field: Hydrological and oceanic effects and their possible detection using GRACE. J. Geophys. Res., 103(B12):30205–30229.

Wahr, J., Wingham, D., and Bentley, C. (2000). A method of combining ICESat and GRACE satellite data to constrain antarctic mass balance. J. Geophys. Res., 105(B7):16279–16294.

Watkins, M. M., Wiese, D. N., Yuan, D.-N., Boening, C., and Landerer, F. W. (2015). Improved methods for observing earth's time variable mass distribution with GRACE using spherical cap mascons. J. Geophys. Res. Solid Earth, 120(4):2648–2671.

Weigel, A. P., Liniger, M. A., and Appenzeller, C. (2008). Can multi-model combination really enhance the prediction skill of probabilistic ensemble forecasts? Quarterly Journal of the Royal Meteorological Society, 134(630):241–260.

Wessem, J. V., Reijmer, C., Morlighem, M., Mouginot, J., Rignot, E., Medley, B., Joughin, I., Wouters, B., Depoorter, M., Bamber, J., Lenaerts, J., Berg, W. D. V., Broeke, M. V. D., and Meijgaard, E. V. (2014). Improved representation of east antarctic surface mass balance in a regional atmospheric climate model. Journal of Glaciology, 60(222):761–770.

Whitehouse, P. L., Bentley, M. J., Milne, G. A., King, M. A., and Thomas, I. D. (2012). A new glacial isostatic adjustment model for antarctica: calibrated and tested using observations of relative sea-level change and present-day uplift rates. Geophysical Journal International, 190(3):1464–1482.

Wiese, D. (2015). Grace mascon ocean and hydrology equivalent water heights jpl rl05m.1.

Wiese, D. N., Landerer, F. W., and Watkins, M. M. (2016). Quantifying and reducing leakage errors in the JPL RL05m GRACE mascon solution. Water Resources Research, 52(9):7490–7502.

Zammit-Mangion, A., Rougier, J., Bamber, J., and Schn, N. (2013). Resolving the antarctic contribution to sea-level rise: a hierarchical modelling framework. Environmetrics, 25(4):245–264.

Zammit-Mangion, A., Rougier, J., Schn, N., Lindgren, F., and Bamber, J. (2015). Multivariate spatio-temporal modelling for assessing antarctica's present-day contribution to sea-level rise. Environmetrics, 26(3):159–177.

Zwally, H. J., Giovinetto, M. B., Beckley, M. A., and Saba, J. L. (2012). Antarctic and greenland drainage systems, gsfc cryospheric sciences laboratory. The Cryosphere.

Zwally, H. J., Li, J., Robbins, J. W., Saba, J. L., Yi, D., and Brenner, A. C. (2015). Mass gains of the antarctic ice sheet exceed losses. Journal of Glaciology, 61(230):1019–1036.